Variational Multiscale Enrichment Method for Modeling of Structures Subjected to Extreme Environments

By

Shuhai (Kyle) Zhang

Dissertation

Submitted to the Faculty of the

Graduate School of Vanderbilt University

in partial fulfillment of the requirements

for the degree of

DOCTOR OF PHILOSOPHY

in

Civil Engineering

August 11, 2017

Nashville, Tennessee

Approved:

Caglar Oskay, Ph.D

Prodyot K. Basu, Ph.D

Ravindra Duddu, Ph.D

Haoxiang Luo, Ph.D

Ravi Penmetsa, Ph.D

To my Mom, Dad and Hui

ACKNOWLEDGMENTS

I would like to express my deepest appreciation to my research advisor, Dr. Caglar Oskay, for his valuable guidance and advice. Thank you for inspiring and entrusting me to perform this challenging research. He has encouraged me to keep achieving higher goals which equipped me with great problem solving skills. Without his advice and support, it would have been impossible to wind my way through the difficulties of this research.

Thank you to Dr. Ravi Penmesta of the Air Force Research Laboratory for your collaboration and support on this research project. His guidance and encouragement have helped me to progress faster during my Ph.D. study.

I would like to thank the remaining members of my Ph.D. committee: Dr. Prodyot Basu, Dr. Ravindra Duddu and Dr. Haoxiang Luo. From the moment I began to work at Vanderbilt University, their support in my research and academic study has been a valuable asset for me. Thank you Dr. Basu for mentoring me in many aspects of my life. It really made my Ph.D. journey delightful and smooth. Thank you Dr. Duddu for encouraging me in my courses and research. Thank you Dr. Luo for guiding me in my studies.

I am very grateful for the opportunity to be a member of Multiscale Computational Mechanics Laboratory (MCML) at Vanderbilt University. It is such a great research group with knowledgeable, helpful and hard working members. Thank you to all the group members of MCML that I have worked with during my time at Vanderbilt. My accomplishments would be diminished without the remarkable ideas, skills and experience shared by everyone in the group.

Thank you to Mom and Dad, Xiaojun and Lixiang, for supporting me wholeheartedly in every aspect of my life. Your endless love have encouraged me to keep improving myself. Very specially thank you to my beautiful and lovely wife, Hui, for your strength and love. I can not thank you enough for supporting and encouraging me in everything that I have chosen to pursue. My life would not be this joyful without your accompany by my side. I am very grateful to have you and cherish you for the rest of my life.

Finally, I gratefully acknowledge the financial support provided by Vanderbilt University, IBM Ph.D. Fellowship Awards Program, and the Air Force Office of Scientific Research Multi-Scale Structural Mechanics and Prognosis Program (Grant No: FA9550-13-1-0104. Program Manager: Dr. David Stargel).

TABLE OF CONTENTS

LIST OF TABLES

LIST OF FIGURES

Chapter 1

INTRODUCTION

1.1 Motivation

Environment exposure induced deterioration of material and related structural failures have been a difficult problem to address from both physical and computational perspectives. The problem is quite pervasive ranging from stress corrosion to hydrogen embrittlement and oxidation of metals to sulfate and chloride attack in concrete and hydration induced leaching in polymers. In surface degradation problems, an aggressive environmental agent attacks the surface of the structure inducing property changes such as embrittlement, cracking and reduction of monotonic and cyclic strength and life as a consequence. The property changes could be due to phase transformation activated by the diffusing agent or lattice strains due to elevated concentrations and pile-ups around the lattice imperfections. In the presence of high temperature, the degradation processes is accelerated and the thermal deformation would cause more critical responses in the structures.

In certain problems, the structural property degradation is severe even for a very small thickness of affected region. For instance, titanium alloys, which are candidate structural materials for hypersonic aircraft, are subjected to formation of a brittle case of oxygen rich layer on its surface under the severe thermo-mechanical environment. While the brittle case is of the order of a few tens of microns thick, the presence of acoustic loads threaten micron cracks within the brittle case to rapidly propagate and cause structural failure. From the computational perspective, this calls for a very refined analysis with resolved material heterogeneities around exposed surfaces. In order to retain computational tractability, the refinement cannot be extended to the entire structure.

Global-local numerical approaches are well-suited to address such problems. These methods attempt to capture the fine scale behavior at small subdomains of the problem, whereas a coarse discretization and modeling is used to approximate the behavior in the remainder of the problem domain. The reason for the particular interests in the small subdomains is determined by the na-

ture of the problem, such as strain localization [1] or environmental degradation [2]. Starting from the early works of Mote [3], a number of global-local methods have been proposed including the global-local finite element method [4, 5, 6, 7], the S-version finite element method [8], the domain decomposition method [9], the generalized/extended finite element method [10, 11, 12, 13], multi-scale coupling based on Lagrange multiplier method [14], among others. These approaches permit the incorporation of additional geometric features such as crack tips [8, 10, 15], as well as material heterogeneities [9] at local subdomains with accurately captured load fields and response mechanisms. However, for many problems, the computational complexity associated with resolving the local features even for small subdomains could be prohibitive, notwithstanding a few examples based on very high performance computing [16].

A number of recent multiscale computational methods are also well suited to address problems that exhibit global-local character. Particularly the multiscale methods which permit the evaluation of scale inseparable problems such as multiscale finite element method [17, 18], multiscale aggregating discontinuities [19, 20], numerical subgrid upscaling [21, 22], variational multiscale enrichment [2, 23, 24] among others have been shown to successfully address global-local problems. The common idea behind these approaches is the additive split of the principal response fields into macro (or coarse) and micro (or fine) components with equal order of magnitude (in contrast to scale separable models, where the fine component is considered a perturbation to the coarse component [25, 26, 27, 28]). The coarse component of the response is evaluated using a coarse grid whereas the fine scale response is evaluated using a fine grid resolving the features of the small scales. Similar to earlier global-local methods, the computational cost of these approaches are large enough to prohibit evaluation of realistic problems.

The high computational expense issue is typically overcome using massively parallel simulations (e.g., [29]), reduced order approximations to the microstructure problems, or a combination of both. In the context of homogenization methods, a number of order reduction approaches, such as generalized method of cells [30], transformation field analysis [31, 32, 33], fast Fourier transforms (FFT) [34], proper orthogonal decomposition [35, 36] and eigendeformation-based model order

reduction [37, 38, 39], among others were successful in reducing the complexity of microstructure computation for linear and nonlinear problems. In the context of global-local methods, FFT was employed to model the thermo-elastic behavior of alumina/Al composites [40, 41].

Variational multiscale method (VMM) originally proposed by Hughes et al. [42] evaluates the fine scale response of the global-local problem analytically or semi-analytically through variational projection [1, 43]. The projection based approach eliminates the need to resolve the fine scale behavior, hence providing a tremendous computational efficiency. Garikipati and Hughes [44, 45] employed the analytical fine scale Green's operator for strain localization problems. Garikipati [46] further incorporated fine scale strain gradient theories into the variational multiscale continuum formulation. Hughes and Sangalli [47] optimized the projection operator for advection-diffusion problems. Masud and Xia [48] developed a stabilized VMM based on variational projection for small strain inelasticity. Masud and Truster [49] extended the stabilized VMM for nearly incompressible elasticity. Yeon and Youn [50] performed variational multiscale analysis on the elasto-plastic deformation problem using a meshfree method. Hund and Ramm [43] employed a continuum damage mechanics model in the context of the numerical subgrid upscaling scheme to address the strain localization problem. Arbogast [21, 22] and Juanes and Dub [51] performed the projection through numerical Green's functions to solve porous media flow problems. However, the projection approach has not been employed to address complex response mechanisms induced by material heterogeneities at the fine scale. A reduced order multiscale method is desirable to address global-local problems with resolved material heterogeneities.

In addition to pure mechanical problems, performance of structures operating in extreme thermo-mechanical environments is also marked by the formation of hot-spots. Hot-spots refer to localized regions within the domain of the structure that are exposed to higher rates of heating, higher stresses or a combination of both. Hot-spots are considered important as they serve as failure initiation sites (such as, shock-boundary layer interaction-induced localized heating in hypersonic aircraft components [52, 53, 54]), and could ultimately define structural survivability. From the modeling perspective, deformation and failure mechanisms within hot-spots may be accurately

captured using thermo-mechanical multiscale computational approaches, where the microstructural heterogeneities are resolved at least within a critical subdomain of the structure. The majority of the previous efforts on thermo-mechanical multiscale modeling employed computational homogenization principles (e.g., Golanski et al. [55], Ghosh et al. [56, 57], Yu and Fish [58], Zhang et al. [59], Ozdemir et al. [60], Muliana et al. [61, 62]), which are valid at the scale separation limit. An efficient multiscale method is missing for the analysis of thermo-mechanical problems with material heterogeneities that exhibit scale inseparable features.

Considering structures subjected to surface degradation induced by coupled transport-thermo-mechanical loading conditions, the detailed material heterogeneity resolution within the surface region is required due to the significant material property changes. Over the localized surface regions of the problem domains, significant structural response variations are observed along the critical directions, such as the direction of aggressive agent diffusion. The material heterogeneity in these directions has essential contributions to the accuracy of the modeling results and has to be resolved in the context of scale inseparable problems. In contrast, the material heterogeneity in the other directions is not of great importance, due to the directionally smooth variation of the structural behaviors. With the scale separation assumption, the material heterogeneity in these directions can be homogenized to improved the computational efficiency of the simulations without significant accuracy loss. A hybrid integration scheme is required to enable the directionally different material heterogeneity treatment within the localized surface region.

1.2 Dissertation Goal and Objectives

The primary goal of the current dissertation is to devise a computationally efficient multiscale framework to accurately model the response of structures subjected to high temperatures, mechanical loads and environmental exposure. The framework would have the capability of resolving material heterogeneities at the subdomains of particular interests, while modeling the structural behaviors with coarse material representations in the remainder of the problem domain. High computational efficiency of the computational framework is expected for the analysis of struc-

tural scale problems. The response coupling effects of the transport-thermo-mechanical problems need to be considered properly, in order to accurately model structures subjected to extreme environments. To achieve the dissertation goal, the following objectives and the associated tasks are accomplished.

Objective 1 Build the foundation of the proposed framework with an approach that can address scale inseparable inelastic problems with resolved material heterogeneity at subdomains.

Task 1.1: Develop the variational multiscale enrichment (VME) method for elasto-viscoplastic problems (2-D Perzyna and Johnson-Cook model).

Task 1.2: Investigate the microscale boundary effect with the presence of plasticity, using mixed boundary conditions.

Objective 2 Improve the computational efficiency of the VME method without significant accuracy loss.

Task 2.1: Develop the reduced order variational multiscale enrichment (ROVME) method for elasto-viscoplastic problems, by extending the eigenstrain-based reduced order modeling to scale inseparable problems.

Task 2.2: Verify the accuracy and computational efficiency of the proposed ROVME method.

Objective 3 Predict multiscale structural response for structures subjected to coupled thermo-mechanical loading conditions

Task 3.1: Generalize the ROVME method to incorporate the temperature effects, including thermal expansion and temperature dependent material properties.

Task 3.2: Investigate the performance of the proposed computational framework for thermo-mechanical problems

Objective 4 Modeling structures subjected to extreme environments

Task 4.1: Develop a hybrid integration for reduced order variational multiscale enrichment (HROVME) method.

Task 4.2: Verify the applicability of the proposed approach in evaluating structural scale surface degradation problems.

1.3 Dissertation Organization

The first research objective is achieved in Chapter 2 which provides the formulation and implementation of the variational multiscale enrichment (VME) method for elasto-viscoplastic problems. Chapter 3 details the reduced order variational multiscale enrichment method (ROVME) which significantly improves the computational efficiency of the VME method. Chapter 4 describes the ROVME method for coupled thermo-mechanical problems that exhibit global-local character. Chapter 5 presents the hybrid integration for reduced order variational multiscale enrichment (HROVME) method to address problems subjected to extreme environments. Conclusions of the current dissertation and future works are provided in Chapter 6.

Chapter 2

VARIATIONAL MULTISCALE ENRICHMENT METHOD WITH MIXED BOUNDARY CONDITIONS FOR ELASTO-VISCOPLASTIC PROBLEMS

2.1 Introduction

This chapter presents the formulation and implementation of the variational multiscale enrichment (VME) method to address inelastic material behavior in the context of deformation problems. The novel contributions of the chapter are: (1) The VME approach is formulated for elasto-viscoplastic material behavior: the previous work on VME included only elastic material behavior [2, 23]; and (2) the performance of the inelastic VME formulation was assessed as a function of the choice of boundary conditions proposed in Ref. [23] in the viscoplastic regime. In the proposed approach, the fine scale representation not only approximates the coarse grid residual, but also accounts for the material heterogeneity. The scale inseparable feature is represented by the relatively insignificant scale size difference and strong coupling effect between the scales. A one-parameter family of mixed boundary conditions that range from Dirichlet to Neumann is employed to study the effect of the choice of the boundary conditions at the fine scale on accuracy. The inelastic material behavior is modeled using Perzyna type viscoplasticity coupled with flow stress evolution idealized by the Johnson-Cook model. Numerical verifications are performed to assess the performance of the proposed approach against the direct finite element simulations. The results of verification studies demonstrate that VME with proper boundary conditions accurately model the inelastic response accounting for material heterogeneity.

The remainder of this chapter is organized as the follows: Section 2.2 provides the problem statement and governing equations of the boundary value problems. Section 2.3 details the variational multiscale enrichment methodology for solving inelastic mechanical problems with elasto-viscoplastic material model. Section 2.4 describes the computational implementation of the proposed methodology, including finite element discretization of the problems and solution strategy.

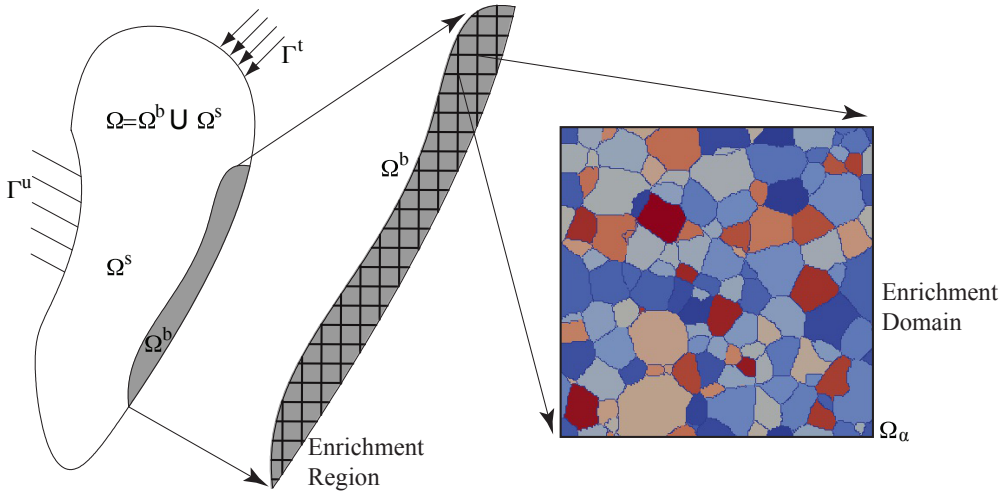

Figure 2.1: The schematic representation of the overall problem domain, enrichment region and an enrichment domain.

Numerical experiments are provided in Section 2.5, including the effect of boundary conditions on accuracy of the proposed computational framework.

2.2 Governing Equations

We start by defining the governing equations that idealize the inelastic deformation within the problem domain. Let $\Omega \subset \mathbb{R}^{n_{\text{sd}}}$ be the domain of the structure as illustrated in Fig. 2.1, where n_{sd} is the number of spatial dimensions. The equilibrium equation is expressed as:

$$\nabla \cdot \boldsymbol{\sigma}(\mathbf{x},t) = 0; \quad \mathbf{x} \in \Omega, \quad t \in [0,\, t_o] \tag{2.1}$$

in the absence of the body forces. $\mathbf{x}$ and t respectively denote the position and time coordinates; $\boldsymbol{\sigma}$ is the stress tensor; ∇ the gradient operator; $(\cdot)$ the inner product; and t_o is the end of the observation period. The boundary conditions are given as:

$$\text{Dirichlet B.C.:} \quad \mathbf{u}(\mathbf{x},t) = \tilde{\mathbf{u}}(\mathbf{x},t); \qquad \mathbf{x} \in \Gamma^u \tag{2.2}$$

$$\text{Neumann B.C.:} \quad \boldsymbol{\sigma}(\mathbf{x},t) \cdot \mathbf{n} = \tilde{\mathbf{t}}(\mathbf{x},t); \qquad \mathbf{x} \in \Gamma^t \tag{2.3}$$

where, $\tilde{\mathbf{u}}$ is the prescribed displacement along the boundary subdomain, Γ^u; $\tilde{\mathbf{t}}$ the prescribed traction along the boundary subdomain, Γ^t. The decomposition of the external boundary is such that $\Gamma = \Gamma^u \cup \Gamma^t$ and $\Gamma^u \cap \Gamma^t \equiv \emptyset$.

The description of the constitutive relationship over the parts of the domain that remain unresolved, as well as the parts that resolve the micro-heterogeneity is taken to be elasto-viscoplastic. The constitutive equation is expressed in the rate form as:

$$\dot{\boldsymbol{\sigma}}(\mathbf{x},t) = \mathbf{L}(\mathbf{x},t) : [\dot{\boldsymbol{\varepsilon}}(\mathbf{x},t) - \dot{\boldsymbol{\varepsilon}}^{vp}(\mathbf{x},t)] \tag{2.4}$$

in which, $\mathbf{L}$ is the tensor of elastic moduli; $\boldsymbol{\varepsilon}$ and $\boldsymbol{\varepsilon}^{vp}$ denote total strain and viscoplastic strain tensors, respectively. The superposed dot indicates material time derivative and $(:)$ the double inner product. The evolution of the viscoplastic strain is idealized based on the Perzyna's viscoplastic model [53]:

$$\dot{\boldsymbol{\varepsilon}}^{vp} = \gamma \left\langle \frac{f}{\sigma_y} \right\rangle^q \frac{\partial f}{\partial \boldsymbol{\sigma}} \tag{2.5}$$

where, σ_y denotes the flow stress; γ the fluidity parameter; q the viscoplastic hardening exponent; $\langle\cdot\rangle$ the Macaulay brackets (i.e., $\langle\cdot\rangle = ((\cdot) + |\cdot|)/2$); and f the loading function defined based on the classical J_2 plasticity:

$$f(\boldsymbol{\sigma}, \varepsilon^{vp}) = \sqrt{3}\bar{\sigma} - \sigma_y(\bar{\varepsilon}^{vp}) \tag{2.6}$$

in which, $\bar{\sigma}$ denotes the second invariant of the deviatoric stress tensor, $\mathbf{s} = \boldsymbol{\sigma} - \mathrm{tr}(\boldsymbol{\sigma})\boldsymbol{\delta}/3$; $\mathrm{tr}(\cdot)$ the trace operator; $\boldsymbol{\delta}$ the Kronecker delta; and $\bar{\varepsilon}^{vp}$ is the effective viscoplastic strain defined as:

$$\bar{\varepsilon}^{vp} = \sqrt{\frac{2}{3}\, \boldsymbol{\varepsilon}^{vp} : \boldsymbol{\varepsilon}^{vp}} \tag{2.7}$$

The flow stress is a function of the effective viscoplastic strain using a reduced version of the Johnson-Cook model:

$$\sigma_y = A + B(\bar{\varepsilon}^{vp})^n \tag{2.8}$$

where, A, B and n are material parameters. We note that the standard Johnson-Cook model includes the effect of strain rate and temperature into the flow equation. The strain rate effect is modeled directly using the Perzyna formulation and the temperature dependence is suppressed for simplicity. All materials in the problem domain are assumed to follow the same general constitutive form, with separate material properties sets defining the behavior of each constituent.

Equations (2.1)-(2.8) constitute the strong form equations of the elasto-viscoplastic problem. The proposed enrichment approach operates within a variational setting. The equilibrium equation along with the boundary conditions is expressed in the weak form as follows:

Find $\mathbf{u} \in \mathscr{V} \times [0,\ t_o]$ such that:

$$\int_{\Omega} \nabla \mathbf{w} : \boldsymbol{\sigma}(\mathbf{x},t)\ d\Omega - \int_{\Gamma^t} \mathbf{w} \cdot \tilde{\mathbf{t}}(\mathbf{x},t)\ d\Gamma = 0; \quad \forall \mathbf{w} \in [H_0^1(\Omega)]^{n_{\text{sd}}} \tag{2.9}$$

along with the constitutive equations (i.e., Eqs. (2.4)-(2.8)) that relate the displacement field to the stress field. The trial space for the displacement field is:

$$\mathscr{V} \equiv \left\{ \hat{\mathbf{u}} \in [H^1(\Omega)]^{n_{\text{sd}}} | \hat{\mathbf{u}} = \tilde{\mathbf{u}} \ \text{ on } \ \mathbf{x} \in \Gamma^u \right\} \tag{2.10}$$

in which, $\mathbf{w}$ is the test function; $H^1(\Omega)$ is the Sobolev space of functions with square integrable values and derivatives defined in the domain, Ω; $H_0^1(\Omega)$ is the subspace of functions in $H^1(\Omega)$ and that are homogeneous along the domain boundary, Γ.

2.3 Variational Multiscale Enrichment (VME)

The governing equations (Eqs. (2.1)-(2.8)) are evaluated using the variational multiscale enrichment method. In this approach, the problem domain, Ω, is decomposed into two non-overlapping subdomains, as demonstrated in Fig. 2.1:

$$\Omega \equiv \Omega^s \cup \Omega^b; \quad \Omega^s \cap \Omega^b \equiv \emptyset \tag{2.11}$$

where, Ω^b denotes the enrichment region, in which the response is accurately characterized by modeling and resolving at the scale of microstructural heterogeneities. In the substrate region Ω^s, coarse scale modeling is taken to be sufficient to accurately capture the mechanical response. It is implicitly assumed that the domain is large enough to computationally prohibit full resolution of the microscale heterogeneities throughout the structure. The enrichment region is further partitioned into enrichment (microstructural) domains. The partitioning is done such that the resulting enrichment domains are simple such that they can be represented by a single finite element at the coarse scale:

$$\Omega^b = \bigcup_{\alpha=1}^{n_{\text{en}}} \Omega_\alpha; \;\; \Omega_\alpha \cap \Omega_\beta \equiv \emptyset \;\; \text{when} \;\; \alpha \neq \beta \tag{2.12}$$

where, n_{en} denotes the total number of enrichment domains. Within each enrichment domain, the microscale heterogeneity is resolved and numerically evaluated.

The boundary of an enrichment domain, α, can be decomposed into the following components:

$$\Gamma_\alpha \equiv \partial\Omega_\alpha = \Gamma_\alpha^{\text{int}} \cup \Gamma_\alpha^s \cup \Gamma_\alpha^u \cup \Gamma_\alpha^t \tag{2.13}$$

in which, Γ_α^s is the part of the boundary that intersects with the substrate region boundary ($\Gamma_\alpha^s \equiv \Gamma_\alpha \cap \partial\Omega^s$); Γ_α^u is the part of the boundary that intersects with the Dirichlet boundary of the problem domain ($\Gamma_\alpha^u \equiv \Gamma_\alpha \cap \Gamma^u$); Γ_α^t is the part of the boundary that intersects with the Neumann boundary of the problem domain ($\Gamma_\alpha^t \equiv \Gamma_\alpha \cap \Gamma^t$); and, $\Gamma_\alpha^{\text{int}}$ is the inter-enrichment domain boundaries:

$$\Gamma_\alpha^{\text{int}} \equiv \bigcup_{\beta \in I_\alpha} \Gamma_\alpha^\beta \tag{2.14}$$

where the neighbor index set of enrichment domain Ω_α, can be expressed as: $I_\alpha \equiv \{\beta \leq n_{\text{en}} | \, \Gamma_{\alpha\beta} \neq \emptyset\}$; $\Gamma_{\alpha\beta}$ is the inter-enrichment domain boundary between α and β domain ($\Gamma_{\alpha\beta} \equiv \Gamma_\alpha \cap \Gamma_\beta$); Γ_α^β and Γ_β^α denotes the α and β side of the inter-enrichment domain boundary, respectively.

The displacement response field is decomposed into macroscale and microscale contributions

through additive two-scale decomposition:

$$\mathbf{u}(\mathbf{x},t) = \mathbf{u}^M(\mathbf{x},t) + \sum_{\alpha=1}^{n_{\text{en}}} \mathscr{H}(\Omega_\alpha)\mathbf{u}_\alpha^m(\mathbf{x},t) \tag{2.15}$$

where, superscripts M and m denote the macroscale and microscale response fields, respectively, and

$$\mathscr{H}(\Omega_\alpha) = \begin{cases} 1, & \text{if } \mathbf{x} \in \Omega_\alpha \\ 0, & \text{elsewhere} \end{cases} \tag{2.16}$$

Equation (2.16) ensures that the microscale displacement field, $\mathbf{u}_\alpha^m$, is nonzero only on the closure of enrichment domain, Ω_α. The decomposition of the displacement field is performed such that the corresponding function spaces recover the trial function space through direct sum ($\mathbf{u}^M \in \mathscr{V}^M(\Omega)$ and $\mathbf{u}_\alpha^m \in \mathscr{V}_\alpha(\Omega_\alpha)$):

$$\mathscr{V}(\Omega) = \mathscr{V}^M(\Omega) \oplus \bigoplus_{\alpha=1}^{n_{\text{en}}} \mathscr{V}_\alpha(\Omega_\alpha) \tag{2.17}$$

in which, $\mathscr{V}^M(\Omega) \subset [H^1(\Omega)]^{n_{sd}}$ is the trial space for the macroscale displacement field and $\mathscr{V}_\alpha(\Omega_\alpha) \subset [H^1(\Omega_\alpha)]^{n_{sd}}$ is the trial space for the microscale displacement field within enrichment domain, Ω_α. This decomposition implies linear independence of the macroscale and the microscale subspaces necessary for uniqueness and stability of the numerical solution [1, 44]. Similar to Eq. (2.17), the test function is additively decomposed into macroscale and microscale components

$$\mathbf{w} = \mathbf{w}^M + \sum_{\alpha=1}^{n_{\text{en}}} \mathscr{H}(\Omega_\alpha)\mathbf{w}_\alpha^m \tag{2.18}$$

where, $\mathbf{w}^M \in \mathscr{W}^M(\Omega) \subset [H_0^1(\Omega)]^{n_{\text{sd}}}$ is the macroscale test function; and $\mathbf{w}_\alpha^m \in \mathscr{W}_\alpha(\Omega_\alpha) \subset [H^1(\Omega_\alpha)]^{n_{\text{sd}}}$ is the microscale test function of the enrichment domain, Ω_α.

Substituting Eqs.(2.18) and (2.15) into Eq. (2.9), the weak form of the problem yields:

$$\begin{aligned} \int_{\Omega_s} \nabla\mathbf{w}^M : \boldsymbol{\sigma}(\mathbf{u}^M, \mathbf{0})\, d\Omega + \sum_{\alpha=1}^{n_{\text{en}}} \int_{\Omega_\alpha} (\nabla\mathbf{w}^M + \nabla\mathbf{w}_\alpha^m) : \boldsymbol{\sigma}(\mathbf{u}^M, \mathbf{u}_\alpha^m)\, d\Omega \\ - \int_{\Gamma^t} (\mathbf{w}^M + \mathbf{w}_\alpha^m) \cdot \tilde{\mathbf{t}}\, d\Gamma = 0 \end{aligned} \tag{2.19}$$

On the substrate domain, the stress field is determined solely from the macroscale displacement field, whereas within the enrichment region, both the macroscale and microscale displacement fields define stress. Since $\mathbf{w}^M$ and $\mathbf{w}^m_\alpha$ are arbitrary and independent, a macroscale and a series of microscale problems over each enrichment domain ($\alpha = 1, 2, ...n_{\text{en}}$) are obtained by collecting the terms with $\mathbf{w}^M$ and $\mathbf{w}^m_\alpha$. Considering the decomposition of the boundaries in Eq. (2.13) and setting the microscale test functions to zero yields the weak form of the macroscale problem:

$$\int_\Omega \nabla \mathbf{w}^M : \boldsymbol{\sigma}(\mathbf{u}^M, \mathbf{u}^m_\alpha) d\Omega - \int_{\Gamma^t} \mathbf{w}^M \cdot \tilde{\mathbf{t}}\, d\Gamma - \int_{\Gamma_{sb}} \mathbf{w}^M \cdot \mathbf{t}^r\, d\Gamma = 0 \tag{2.20}$$

where, $\mathbf{t}^r$ denotes the residual tractions along the substrate-enrichment region boundary, Γ_{sb}. The weak form of the microscale problem at an arbitrary enrichment domain, α, is obtained similarly by considering vanishing macroscale test functions:

$$\int_{\Omega_\alpha} \nabla \mathbf{w}^m_\alpha : \boldsymbol{\sigma}(\mathbf{u}^M, \mathbf{u}^m_\alpha) d\Omega - \int_{\Gamma^t_\alpha} \mathbf{w}^m_\alpha \cdot \tilde{\mathbf{t}}\, d\Gamma - \int_{\Gamma_\alpha \setminus \Gamma} \mathbf{w}^m_\alpha \cdot \mathbf{t}\, d\Gamma = 0 \tag{2.21}$$

in which, $\mathbf{t}$ denotes the internal tractions along the boundaries of the enrichment domain that does not overlap with the external boundaries. Substituting the displacement decomposition (Eq. (2.15)) into Eq. (2.4), the stress-strain relationship is expressed as a function of the macro- and micro-variables in the rate form as:

$$\dot{\boldsymbol{\sigma}} = \mathbf{L} : \left[\dot{\boldsymbol{\varepsilon}}^M(\mathbf{u}^M) + \sum_{\alpha=1}^{n_{\text{en}}} \mathscr{H}(\Omega_\alpha)\, \dot{\boldsymbol{\varepsilon}}^m_\alpha(\mathbf{u}^m_\alpha) - \dot{\boldsymbol{\varepsilon}}^{vp}(\boldsymbol{\sigma}, \mathbf{u}^M, \mathbf{u}^m) \right] \tag{2.22}$$

The macroscale and microscale response fields, along with their test functions, are discretized using the standard Buhnov-Galerkin approach. The finite element spaces are shown in the following:

$$\mathscr{V}^M(\Omega) \equiv \left\{ \mathbf{u}^M(\mathbf{x}, t) \,\middle|\, \mathbf{u}^M(\mathbf{x}, t) = \sum_{A=1}^{N_D} N_A(\mathbf{x})\, \hat{\mathbf{u}}^M_A(t);\ \hat{\mathbf{u}}^M_A(t) = \hat{\mathbf{u}}^M(\mathbf{x}_A, t) \text{ if } \mathbf{x}_A \in \Gamma^u \right\} \tag{2.23}$$

$$\mathscr{V}^m_\alpha(\Omega_\alpha) \equiv \left\{ \mathbf{u}^m_\alpha(\mathbf{x}, t) \,\middle|\, \mathbf{u}^m_\alpha(\mathbf{x}, t) = \sum_{a=1}^{n_{d\alpha}} n_{\alpha,a}(\mathbf{x})\, \hat{\mathbf{u}}^m_{\alpha,a}(t);\ \hat{\mathbf{u}}^m_{\alpha,a}(t) = \hat{\mathbf{u}}_\alpha(\mathbf{x}_\alpha, t) \text{ if } \mathbf{x}_\alpha \in \Gamma^u_\alpha \right\} \tag{2.24}$$

in which, N_D and n_{d_α} denote the number of nodes in the macroscale discretization Ω, and the microscale discretization of Ω_α, respectively; N_A and $n_{\alpha,a}$ are the shape functions for the macroscale and microscale fields, respectively; $\mathbf{x}_A$ and $\mathbf{x}_\alpha$ are the corresponding nodal coordinates. Overhat denotes the nodal coordinates of the corresponding response field. The present formulation considers the macroscale and microscale grids to be nested, which means each enriched macroscale finite element coincides with a corresponding enrichment domain in the enrichment region. It is also possible to consider enrichment domains to be independent of the macroscale mesh, i.e., each enrichment domain may occupy multiple macroscale elements. While the general formulation is unaffected by this generalization, the implementation could be quite different and not considered in this study.

2.3.1 Mixed boundary conditions at microscale

The accuracy of the response approximation using the VME method is significantly affected by the conditions imposed along the enrichment domain boundaries. In variational multiscale literature, the typical choice has been the homogeneous Dirichlet boundary condition [63, 64, 65, 66, 67]:

$$\mathbf{u}_\alpha^m(\mathbf{x},t) = 0;\ \mathbf{x} \in \Gamma_\alpha \tag{2.25}$$

The resulting microscale displacement is homogeneous along enrichment domain boundaries and nonzero in the interior, leading to the bubble shape and sometimes referred as residual free bubbles. This boundary condition typically leads to overly stiff response. In order to relax the overconstraint imposed by the homogeneous Dirichlet boundary condition, mixed boundary conditions that has been proposed for elasticity problems in Ref. [23] are generalized for inelastic problems and implemented herein. When the mixed boundary conditions are employed, the resulting microscale displacement is zero at enrichment domain corners and nonzero elsewhere, leading to a canopy shape and referred as the canopy functions. In this approach the boundary tractions along the

enrichment domain boundaries are expressed as:

$$\mathbf{t}^r(\mathbf{x},t) = \hat{\mathbf{t}}_\alpha(\mathbf{x},t) - \kappa\,[\mathbf{u}^m_\alpha(\mathbf{x},t) - \hat{\mathbf{u}}_\alpha(\mathbf{x},t)] \;\; \text{on} \;\; \mathbf{x} \in \Gamma_\alpha \equiv \partial\Omega_\alpha; \;\; \alpha = 1,2,...n_{\text{en}}. \tag{2.26}$$

where $\hat{\mathbf{t}}_\alpha(\mathbf{x},t)$ and $\hat{\mathbf{u}}_\alpha(\mathbf{x},t)$ are prescribed traction and displacement along the microscale boundary. Equation (2.26) constitutes a one-parameter family of boundary conditions that range from a pure Neumann condition when $\kappa = 0$ to a pure Dirichlet condition when $\kappa \to \infty$ (denoted as $\kappa = \kappa_\infty$). The boundary parameter, κ (such that $0 \leq \kappa < \infty$) therefore controls the boundary constraint stiffness and is adjusted to improve solution accuracy. On the inter-enrichment domain boundaries, $\Gamma_{\alpha\beta}$, the boundary data vanishes (i.e., $\hat{\mathbf{t}}_\alpha(\mathbf{x},t) = 0$ and $\hat{\mathbf{u}}_\alpha(\mathbf{x},t) = 0$) and Eq. (2.26) leads to mixed boundary conditions that range from traction-free to homogeneous Dirichlet conditions. The residual free bubbles are achieved by setting $\kappa = \infty$ on Γ_α.

The proposed mixed boundary condition also improves the approximation of the prescribed conditions along the external boundaries of the problem domain, Ω. Consider the prescribed traction $\tilde{\mathbf{t}}$ along the external boundary Γ^t_α is variable at the scale of the microstructure. The residual external traction not resolved by the coarse grid is expressed as:

$$\hat{\mathbf{t}}_\alpha(\mathbf{x},t) = \tilde{\mathbf{t}}_\alpha(\mathbf{x},t) \equiv \tilde{\mathbf{t}}(\mathbf{x},t) - \tilde{\mathbf{t}}^M(\mathbf{x},t) \;\; \text{on} \; \mathbf{x} \in \Gamma^t_\alpha \tag{2.27}$$

The residual traction is enforced by setting, $\kappa = 0$ at Γ^t_α. Similarly, the residual applied displacement along the boundary Γ^u_α is:

$$\hat{\mathbf{u}}_\alpha(\mathbf{x},t) = \tilde{\mathbf{u}}_\alpha(\mathbf{x},t) \equiv \tilde{\mathbf{u}}(\mathbf{x},t) - \tilde{\mathbf{u}}^M(\mathbf{x},t) \;\; \text{on} \; \mathbf{x} \in \Gamma^u_\alpha \tag{2.28}$$

in which, $\tilde{\mathbf{u}}^M(\mathbf{x},t)$ is the coarse grid approximation of the prescribed displacement. The residual prescribed displacement field is imposed by setting $\kappa = \kappa_\infty$ on Γ^u_α.

In order to satisfy the continuity of the displacement fields across the inter-enrichment domain boundaries, a master-slave coupling approach is employed [23]. Let the neighbor index set for the

enrichment domain α be split into master and slave index sets:

$$\begin{aligned} I_\alpha^m &\equiv \left\{\beta |\ \alpha < \beta \leq n_{\text{en}} |\ \Gamma_{\alpha\beta} \neq \emptyset\right\}; \\ I_\alpha^s &\equiv \left\{\beta |\ \beta < \alpha \leq n_{\text{en}} |\ \Gamma_{\alpha\beta} \neq \emptyset\right\}. \end{aligned} \tag{2.29}$$

For an arbitrary enrichment domain, α, the displacement continuity is enforced by considering:

$$\mathbf{t}^r(\mathbf{x},t) = -\kappa_\infty \left[\mathbf{u}_\alpha^m(\mathbf{x},t) - \mathbf{u}_\beta^m(\mathbf{x},t)\right];\ \ \beta \in I_\alpha^s \text{ and } \mathbf{x} \in \Gamma_\alpha^\beta \tag{2.30}$$

Employing the mixed boundary conditions as well as the displacement continuity conditions along the inter-enrichment boundaries, the microscale problems defined in Eq. (2.21) is expressed as:

$$\begin{aligned} \Psi_\alpha^m \equiv &\int_{\Omega_\alpha} \nabla \mathbf{w}_\alpha^m : \boldsymbol{\sigma}(\mathbf{u}^M, \mathbf{u}_\alpha^m)\, d\Omega - \int_{\Gamma_\alpha^t} \mathbf{w}_\alpha^m \cdot \tilde{\mathbf{t}}_\alpha\, d\Gamma - \int_{\Gamma_\alpha} \mathbf{w}_\alpha^m \cdot \mathbf{t}^M\, d\Gamma + \kappa_\infty \int_{\Gamma_\alpha^s} \mathbf{w}_\alpha^m \cdot \mathbf{u}_\alpha^m\, d\Gamma \\ &+ \kappa \sum_{\beta \in I_\alpha^m} \int_{\Gamma_\alpha^\beta} \mathbf{w}_\alpha^m \cdot \mathbf{u}_\alpha^m\, d\Gamma + \kappa_\infty \sum_{\beta \in I_\alpha^s} \int_{\Gamma_\alpha^\beta} \mathbf{w}_\alpha^m \cdot \left(\mathbf{u}_\alpha^m - \mathbf{u}_\beta^m\right)\, d\Gamma - \kappa_\infty \int_{\Gamma_\alpha^u} \mathbf{w}_\alpha^m \cdot \tilde{\mathbf{u}}\, d\Gamma = 0 \end{aligned} \tag{2.31}$$

The displacement continuity is satisfied by setting $\kappa = \kappa_\infty$ along the interface between the enrichment domain and the substrate domain. Considering the mixed boundary conditions, the macroscale problem in Eq. (2.20) becomes:

$$\Psi^M \equiv \int_\Omega \nabla \mathbf{w}^M : \boldsymbol{\sigma}(\mathbf{u}^M, \mathbf{u}_\alpha^m)\, d\Omega - \int_{\Gamma^t} \mathbf{w}^M \cdot \tilde{\mathbf{t}}^M\, d\Gamma + \kappa_\infty \sum_{\alpha=1}^{n_{\text{en}}} \int_{\Gamma_\alpha^s} \mathbf{w}^M \cdot \mathbf{u}_\alpha^m\, d\Gamma = 0 \tag{2.32}$$

In the numerical verification studies below, a sufficiently large but finite value is employed for κ_∞ for stability and accuracy.

Equations (2.31) and (2.32), along with the constitutive equations, constitute the coupled multiscale system. The microscale problem defined over the enrichment domain (Eq. (2.31)) is coupled to the macroscale response field through the constitutive relationship (i.e., through the first term on the left hand side of Eq. (2.31)) as well as the macroscale tractions. The macroscale problem

is similarly coupled to the microscale response field through the constitutive relationship and the boundary interactions.

The variational multiscale enrichment system (Eqs. (2.31) and (2.32)) are linearized and solved using a staggered scheme in the context of finite element discretization, along with the constitutive equation (Eq. (2.22)) and the viscoplastic strain evolution (Eq. (2.5)). The detailed formulation and implementation for the numerical evaluation of the VME system (including consistent linearization, finite element discretization and implementation strategy) are detailed in Ref. [24]. They are skipped herein for the simplicity of presentation.

2.4 Computational Implementation

The weak form macroscale equation defined over the problem domain, Ω and the microscale equations defined over each enrichment domain, Ω_α are nonlinear through the constitutive relationship and coupled. The computational implementation of the evolution of this nonlinear coupled system is performed by consistent linearization and finite element discretization, which leads to a coupled algorithmic system. The evaluation of the coupled algorithmic system is performed by employing a sequential coupling algorithm described in Section 2.4.3.

2.4.1 Consistent linearization

The macro- and microscale equations along with the constitutive equations are discretized in time to obtain a linearized system of equations evaluated incrementally. The linearization consists of time discretization of the weak forms, stress-strain, kinematic equations and condensation of the constitutive equations to arrive at a system, in which the unknowns are the macro- and microscale displacement fields only. Substituting Eq. (2.15) into Eq.(2.4), the stress-strain equation is expressed as a function of the macro- and microscale displacement fields as:

$$\dot{\boldsymbol{\sigma}} = \mathbf{L} : \left[\dot{\boldsymbol{\varepsilon}}^M(\mathbf{u}^M) + \sum_{\alpha=1}^{n_{\text{en}}} \mathscr{H}(\Omega_\alpha)\, \dot{\boldsymbol{\varepsilon}}^m_\alpha(\mathbf{u}^m_\alpha) - \dot{\boldsymbol{\varepsilon}}^{vp}(\boldsymbol{\sigma}, \mathbf{u}^M, \mathbf{u}^m) \right] \tag{2.33}$$

in which, $\theta \in [0,1]$ is an algorithmic parameter. $\mathbf{u}^m := \{\mathbf{u}_\alpha^m\}_{\alpha=1}^{n_{\text{en}}}$ is the set of all microscale displacement fields. We proceed with the time discretization of the governing equations. Consider a discrete set of instances with the observation period: $\{0, {}_1t, {}_2t, ..., {}_nt, {}_{n+1}t, ..., t_o\}$. The viscoplastic slip evolution is discretized based on a one-parameter family (referred to as θ-rule):

$$\dot{\varepsilon}^{vp}(\mathbf{x},t) = (1-\theta)\dot{\varepsilon}^{vp}(\mathbf{x},{}_nt) + \theta\dot{\varepsilon}^{vp}(\mathbf{x},{}_{n+1}t); \quad t \in [{}_nt,\ {}_{n+1}t] \tag{2.34}$$

which leads to the following expression for viscoplastic update:

$$\mathbf{P} \equiv {}_{n+1}\varepsilon^{vp} - {}_n\varepsilon^{vp} - \Delta t\ (1-\theta)\ {}_n\dot{\varepsilon}^{vp} - \Delta t\ \theta\ {}_{n+1}\dot{\varepsilon}^{vp} = 0 \tag{2.35}$$

in which left subscript n and $n+1$ indicate the value of a field variable at ${}_nt$ and ${}_{n+1}t$, respectively (e.g. ${}_n\varepsilon^{vp} = \varepsilon^{vp}({}_nt)$). The time discretization of Eq. (2.33) yields:

$$\begin{aligned}\mathbf{R}(\boldsymbol{\sigma}, \mathbf{u}^M, \mathbf{u}^m) \equiv {}_{n+1}\boldsymbol{\sigma} - {}_n\boldsymbol{\sigma} - \mathbf{L} : \Delta\varepsilon^M - \sum_{\alpha=1}^{n_{\text{en}}} \mathscr{H}(\Omega_\alpha)\mathbf{L} : \Delta\varepsilon_\alpha^m + \\ (1-\theta)\Delta t\ \mathbf{L} : {}_n\dot{\varepsilon}^{vp} + \theta\Delta t\ \mathbf{L} : {}_{n+1}\dot{\varepsilon}^{vp} = 0\end{aligned} \tag{2.36}$$

where $\Delta\varepsilon^M = {}_{n+1}(\nabla\mathbf{u}^M) - {}_n(\nabla\mathbf{u}^M)$ and $\Delta\varepsilon_\alpha^m = {}_{n+1}(\nabla\mathbf{u}_\alpha^m) - {}_n(\nabla\mathbf{u}_\alpha^m)$. The system of equations defined by $\mathbf{P}$, $\mathbf{R}$ along with $\boldsymbol{\Psi}^M$ and $\boldsymbol{\Psi}_\alpha^m$ are evaluated using the Newton-Raphson iterative scheme. In what follows, we seek to evaluate the nonlinear multiscale system between $[{}_nt,\ {}_{n+1}t]$ from the " known" equilibrium configuration ${}_nt$ to the current configuration at ${}_{n+1}t$. In what follows, the subscript $n+1$ from the fields at current configuration is omitted for clarity of presentation. Considering a first order Taylor series approximation of Eq. (2.36) and forming a Newton iteration yield the following residual for the stress-strain equation:

$$\begin{aligned}\mathbf{R}^{k+1} \approx \mathbf{R}^k + (\mathbf{I} + \theta\ \Delta t\ \mathbf{L} : \mathbf{C}^k) : \delta\boldsymbol{\sigma} - \mathbf{L} : \nabla(\delta\mathbf{u}^M) \\ - \sum_{\alpha=1}^{n_{\text{en}}} \mathscr{H}(\Omega_\alpha)\mathbf{L} : \nabla(\delta\mathbf{u}_\alpha^m) + \theta\ \Delta t\ \mathbf{L} : \mathbf{G}^k : \delta\varepsilon^{vp} = 0\end{aligned} \tag{2.37}$$

in which, superscript k denotes Newton iteration counter; $\delta(\cdot)$ indicates the increment of response field $(\cdot)$ during the current iteration (e.g., $\delta\mathbf{u}^M = \mathbf{u}^{M,k+1} - \mathbf{u}^{M,k}$); $\mathbf{I}$ the fourth order identity tensor; and:

$$\mathbf{C}^k = \left(\frac{\partial \dot{\varepsilon}^{vp}}{\partial \boldsymbol{\sigma}}\right)^k; \quad \mathbf{G}^k = \left(\frac{\partial \dot{\varepsilon}^{vp}}{\partial \varepsilon^{vp}}\right)^k \tag{2.38}$$

The expression for derivatives $\mathbf{C}^k$ and $\mathbf{G}^k$ are provided in Ref. [24]. The linearization of the kinematic equation residual expression (Eq. (2.35)) yields the following expression:

$$\mathbf{P}^{k+1} \approx \mathbf{P}^k + (\mathbf{I} - \theta\ \Delta t\ \mathbf{G}^k) : \delta\varepsilon^{vp} - \theta\ \Delta t\ \mathbf{C}^k : \delta\boldsymbol{\sigma} = 0 \tag{2.39}$$

Rearranging Eq. (2.39), the viscoplastic strain increment at the current Newton iteration is expressed in terms of the stress increment as:

$$\delta\varepsilon^{vp} = (\mathbf{I} - \theta\ \Delta t\ \mathbf{G}^k)^{-1} : (\theta\ \Delta t\ \mathbf{C}^k) : \delta\boldsymbol{\sigma} - (\mathbf{I} - \theta\ \Delta t\ \mathbf{G}^k)^{-1} : \mathbf{P}^k \tag{2.40}$$

Substituting Eq. (2.40) into Eq. (2.37) condenses out the viscoplastic strain and yields:

$$\mathbf{R}^k - \mathbf{Z}^k + (\mathbf{I} + \theta\ \Delta t\ \mathbf{L} : \mathbf{C}^k + \mathbf{H}^k) : \delta\boldsymbol{\sigma} - \mathbf{L} : \nabla(\delta\mathbf{u}^M) - \sum_{\alpha=1}^{n_{\text{en}}} \mathscr{H}(\Omega_\alpha)\mathbf{L} : \nabla(\delta\mathbf{u}_\alpha^m) = 0 \tag{2.41}$$

where,

$$\mathbf{H}^k = (\theta\Delta t)^2\ \mathbf{L} : \mathbf{G}^k : (\mathbf{I} - \theta\ \Delta t\ \mathbf{G}^k)^{-1} : \mathbf{C}^k \tag{2.42a}$$

$$\mathbf{Z}^k = \theta\ \Delta t\ \mathbf{L} : \mathbf{G}^k : (\mathbf{I} - \theta\ \Delta t\ \mathbf{G}^k)^{-1} : \mathbf{P}^k \tag{2.42b}$$

Equation (2.41) can be solved with respect to the stress increment, resulting in

$$\delta\boldsymbol{\sigma}(\delta\mathbf{u}^M, \delta\mathbf{u}_\alpha^m) = \hat{\mathbf{L}}^k : \nabla(\delta\mathbf{u}^M) + \sum_{\alpha=1}^{n_{\text{en}}} \mathscr{H}(\Omega_\alpha)\ \hat{\mathbf{L}}^k : \nabla(\delta\mathbf{u}_\alpha^m) - \mathbf{Q}^k : (\mathbf{R}^k - \mathbf{Z}^k) \tag{2.43}$$

where

$$\hat{\mathbf{L}}^k = \left(\mathbf{L}^{-1} + \theta\ \Delta t\ \mathbf{C}^k + \mathbf{L}^{-1} : \mathbf{H}^k\right)^{-1} \tag{2.44}$$

$$\mathbf{Q}^k = \left(\mathbf{I} + \theta\ \Delta t\ \mathbf{L} : \mathbf{C}^k + \mathbf{H}^k\right)^{-1} \tag{2.45}$$

The linearized weak form equilibrium equation for the macroscale is expressed in terms of the stress and the microscale displacement increments as:

$$\boldsymbol{\Psi}^{M,k+1} \approx \boldsymbol{\Psi}^{M,k} + \int_{\Omega} \nabla \mathbf{w}^M : \delta\boldsymbol{\sigma}\ d\Omega + \sum_{\alpha=1}^{n_{\text{en}}} \kappa_{\infty} \int_{\Gamma_\alpha^s} \mathbf{w}^M \cdot \delta\mathbf{u}_\alpha^m\ d\Gamma = 0 \tag{2.46}$$

Similarly, the linearization of the microscale problem over Ω_α ($\alpha = 1, 2, ...n_{\text{en}}$):

$$\begin{aligned} \boldsymbol{\Psi}_\alpha^{m,k+1} \approx\ & \boldsymbol{\Psi}_\alpha^{m,k} + \int_{\Omega_\alpha} \nabla \mathbf{w}_\alpha^m : \delta\boldsymbol{\sigma}\ d\Omega - \int_{\Gamma_\alpha} \mathbf{w}_\alpha^m \cdot \delta\mathbf{t}^M\ d\Gamma + \kappa_{\infty} \int_{\Gamma_\alpha^s} \mathbf{w}_\alpha^m \cdot \delta\mathbf{u}_\alpha^m\ d\Gamma \\ & + \sum_{\beta \in I_\alpha^m} \kappa \int_{\Gamma_\alpha^\beta} \mathbf{w}_\alpha^m \cdot \delta\mathbf{u}_\alpha^m\ d\Gamma + \sum_{\beta \in I_\alpha^s} \kappa_{\infty} \int_{\Gamma_\alpha^\beta} \mathbf{w}_\alpha^m \cdot \left(\delta\mathbf{u}_\alpha^m - \delta\mathbf{u}_\beta^m\right)\ d\Gamma = 0 \end{aligned} \tag{2.47}$$

where $\delta\mathbf{t}^M = \boldsymbol{\sigma}^{k+1}(\mathbf{u}^{M,k+1}, \mathbf{0}) - \boldsymbol{\sigma}^k(\mathbf{u}^{M,k}, \mathbf{0})$ is the macroscale traction over the microscale domain boundaries computed from Eq. (2.43). Substituting Eq. (2.43) into Eqs. (2.46) and (2.47), the linearized governing equations for the macroscale problems is expressed as:

$$\begin{aligned} \int_{\Omega} \nabla \mathbf{w}^M : \hat{\mathbf{L}}^k : \nabla(\delta\mathbf{u}^M)\ d\Omega =\ & -\sum_{\alpha=1}^{n_{\text{en}}} \int_{\Omega_\alpha} \nabla \mathbf{w}^M : \hat{\mathbf{L}}^k : \nabla(\delta\mathbf{u}_\alpha^m)\ d\Omega \\ & + \int_{\Omega} \nabla \mathbf{w}^M : \mathbf{Q}^k : (\mathbf{R}^k - \mathbf{Z}^k)\ d\Omega - \sum_{\alpha=1}^{n_{\text{en}}} \kappa_{\infty} \int_{\Gamma_\alpha^s} \mathbf{w}^M \cdot \delta\mathbf{u}_\alpha^m\ d\Gamma - \boldsymbol{\Psi}^{M,k} \end{aligned} \tag{2.48}$$

and for the microscale domains over Ω_α ($\alpha = 1, 2, ...n_{\text{en}}$):

$$\begin{aligned} \int_{\Omega_\alpha} \nabla \mathbf{w}_\alpha^m : \hat{\mathbf{L}}^k : \nabla(\delta\mathbf{u}_\alpha^m)\ d\Omega =\ & -\int_{\Omega_\alpha} \nabla \mathbf{w}_\alpha^m : \hat{\mathbf{L}}^k : \nabla(\delta\mathbf{u}^M)\ d\Omega + \int_{\Omega_\alpha} \nabla \mathbf{w}_\alpha^m : \mathbf{Q}^k : (\mathbf{R}^k - \mathbf{Z}^k)\ d\Omega \\ & + \int_{\Gamma_\alpha} \mathbf{w}_\alpha^m \cdot \left[\hat{\mathbf{L}}^k : \nabla(\delta\mathbf{u}^M) - \mathbf{Q}^k : (\mathbf{R}^k - \mathbf{Z}^k)\right]\ d\Gamma - \kappa_{\infty} \int_{\Gamma_\alpha^s} \mathbf{w}_\alpha^m \cdot \delta\mathbf{u}_\alpha^m\ d\Gamma \\ & - \sum_{\beta \in I_\alpha^m} \kappa \int_{\Gamma_\alpha^\beta} \mathbf{w}_\alpha^m \cdot \delta\mathbf{u}_\alpha^m\ d\Gamma - \sum_{\beta \in I_\alpha^s} \kappa_{\infty} \int_{\Gamma_\alpha^\beta} \mathbf{w}_\alpha^m \cdot \left(\delta\mathbf{u}_\alpha^m - \delta\mathbf{u}_\beta^m\right)\ d\Gamma - \boldsymbol{\Psi}_\alpha^{m,k} \end{aligned} \tag{2.49}$$

It can be observed from Eqs. (2.48) and (2.49) the value of the boundary parameter κ for all inter-enrichment domain boundaries is set as a fixed value for all inter-enrichment domains and throughout the loading process. The value of the boundary parameter for the parts of the enrichment domain boundaries that overlap with prescribed Dirichlet boundaries and enrichment domain-substrate domain interface is set to a very large value (κ_∞). The κ parameter is set to zero when the enrichment domain boundary lies along prescribed Neumann boundaries, as described in Section 3.1.

2.4.2 Finite element discretization

Equations (2.48) and (2.49) are evaluated using the finite element method. Consider the following finite element spaces for the macro- and microscale response fields:

$$\mathscr{V}^M(\Omega) \equiv \left\{ \mathbf{u}^M(\mathbf{x},t) \,\middle|\, \mathbf{u}^M(\mathbf{x},t) = \sum_{A=1}^{N_D} N_A(\mathbf{x})\, \hat{\mathbf{u}}_A^M(t);\ \hat{\mathbf{u}}_A^M(t) = \hat{\mathbf{u}}^M(\mathbf{x}_A,t) \text{ if } \mathbf{x}_A \in \Gamma^u \right\} \tag{2.50}$$

$$\mathscr{V}_\alpha^m(\Omega_\alpha) \equiv \left\{ \mathbf{u}_\alpha^m(\mathbf{x},t) \,\middle|\, \mathbf{u}_\alpha^m(\mathbf{x},t) = \sum_{a=1}^{n_{d\alpha}} n_{\alpha,a}(\mathbf{x})\, \hat{\mathbf{u}}_{\alpha,a}^m(t);\ \hat{\mathbf{u}}_{\alpha,a}^m(t) = \hat{\mathbf{u}}_\alpha(\mathbf{x}_\alpha,t) \text{ if } \mathbf{x}_\alpha \in \Gamma_\alpha^u \right\} \tag{2.51}$$

in which, N_D and n_{d_α} denote the number of nodes in the macroscale discretization Ω, and the microscale discretization of Ω_α, respectively; N_A and $n_{\alpha,a}$ are the shape functions for the macroscale and microscale fields, respectively; $\mathbf{x}_A$ and $\mathbf{x}_\alpha$ are the corresponding nodal coordinates. Overhat denotes the nodal coordianates of the corresponding response field. The present formulation considers the macroscale and microscale grids to be nested, which means each enriched macroscale finite element coincides with a corresponding enrichment domain in the enrichment region. It is also possible to consider enrichment domains to be independent of the macroscale mesh, i.e., each enrichment domain may occupy multiple macroscale elements. While the general formulation is unaffected by this generalization, the implementation could be quite different and not considered in this study. Employing the standard Bubnov-Galerkin approach, the test functions are taken to be discretized using the same macro- and microscale shape functions.

Substitute Eqs. (2.50) and (2.51) into the macroscale weak form (Eq. (2.48)) yields the discrete macroscale system. At the $(k+1)$th iteration of the current time step, ${}_{n+1}t$, the macroscale weak form takes the form expressed as:

$$\mathbf{K}\ \delta\hat{\mathbf{u}}^{M} = \delta\mathbf{f} \tag{2.52}$$

where,

$$\delta\hat{\mathbf{u}}^{M} = \left\{ \left(\delta\hat{\mathbf{u}}_1^{M,k+1}\right)^T, \left(\delta\hat{\mathbf{u}}_2^{M,k+1}\right)^T, ..., \left(\delta\hat{\mathbf{u}}_{N_D}^{M,k+1}\right)^T \right\}^T \tag{2.53}$$

in which, $\delta\hat{\mathbf{u}}_A^{M,k+1} = \hat{\mathbf{u}}_A^{M,k+1} - \hat{\mathbf{u}}_A^{M,k}$ $(A = 1,2,...,N_D)$ and $\delta\hat{\mathbf{u}}^{M}$ denotes the increment of the macroscale nodal displacement coefficients at the $(k+1)$th iteration. The tangent stiffness matrix is expressed as:

$$\mathbf{K} = \underset{A,B}{\mathbf{A}} \int_{\Omega} \nabla N_A \cdot \hat{\mathbf{L}}^{k} \cdot \nabla N_B \, d\Omega \tag{2.54}$$

in which $\mathbf{A}$ denotes the standard finite element assembly operator. Within the macroscale elements associated with an enrichment domain, the tensor of tangent moduli, $\hat{\mathbf{L}}$ oscillates due to the heterogeneity of the microstructure. The integral is resolved and evaluated based on the underlying coarse grid on enriched elements. The force increment in the current iteration, $\delta\mathbf{f}$ is expressed as:

$$\begin{aligned}\delta\mathbf{f} = \underset{A}{\mathbf{A}} \Bigg\{ &- \sum_{\alpha=1}^{n_{\text{en}}} \sum_{a=1}^{n_{d\alpha}} \left[\int_{\Omega_\alpha} \nabla N_A \cdot \hat{\mathbf{L}}^{k} \cdot \nabla n_{\alpha,a} \, d\Omega \ \delta\hat{\mathbf{u}}_{\alpha,a}^{m} + \kappa_\infty \int_{\Gamma_\alpha^s} N_A \, n_{\alpha,a} \, d\Gamma \ \delta\hat{\mathbf{u}}_{\alpha}^{m} \right] \\ &+ \int_{\Omega} \nabla N_A \cdot \mathbf{Q}^{k} : (\mathbf{R}^{k} - \mathbf{Z}^{k}) \, d\Omega \Bigg\} - \boldsymbol{\Psi}^{M,k}\end{aligned} \tag{2.55}$$

The discrete microscale system for the enriched domain, α, is obtained by substituting Eqs. (2.50) and (2.51) into the microscale weak form (Eq. (2.49)):

$$\mathbf{K}_\alpha\ \delta\hat{\mathbf{u}}_\alpha^{m} = \delta\mathbf{f}_\alpha \tag{2.56}$$

where,

$$\delta\hat{\mathbf{u}}_\alpha^{m} = \left\{ \left(\delta\hat{\mathbf{u}}_{\alpha,1}^{m,k+1}\right)^T, \left(\delta\hat{\mathbf{u}}_{\alpha,2}^{m,k+1}\right)^T, ..., \left(\delta\hat{\mathbf{u}}_{\alpha,nd_\alpha}^{m,k+1}\right)^T \right\}^T \tag{2.57}$$

in which, $\delta\hat{\mathbf{u}}^{m,k+1}_{\alpha,a} = \hat{\mathbf{u}}^{m,k+1}_{\alpha,a} - \hat{\mathbf{u}}^{m,k}_{\alpha,a}$ $(a = 1,2,...,n_{d_\alpha})$ and $\delta\hat{\mathbf{u}}^{m}_{\alpha}$ denotes the increment of the microscale nodal displacement coefficients at the $(k+1)$th iteration . The microscale tangent stiffness matrix is assembled as:

$$\begin{aligned}\mathbf{K}_\alpha = \underset{a,b}{\mathbf{A}} \Bigg\{ & \int_{\Omega_\alpha} \nabla n_{\alpha,a} \cdot \hat{\mathbf{L}}^k \cdot \nabla n_{\alpha,b}\, d\Omega_\alpha + \kappa_\infty \int_{\Gamma^s_\alpha} n_{\alpha,a}\, n_{\alpha,b}\, d\Gamma \\ & + \kappa \int_{\Gamma^{\beta m}_\alpha} n_{\alpha,a}\, n_{\alpha,b}\, d\Gamma + \kappa_\infty \int_{\Gamma^{\beta s}_\alpha} n_{\alpha,a}\, n_{\alpha,b}\, d\Gamma \Bigg\}\end{aligned} \tag{2.58}$$

and the corresponding force increment is expressed as:

$$\begin{aligned}\delta\mathbf{f}_\alpha = \underset{a}{\mathbf{A}} \Bigg\{ & - \int_{\Omega_\alpha} \nabla n_{\alpha,a} \cdot \hat{\mathbf{L}}^k \cdot \nabla N_B\, d\Omega\, \delta\hat{\mathbf{u}}^M_B(t) + \int_{\Omega_\alpha} \nabla n_{\alpha,a} \cdot \mathbf{Q}^k : (\mathbf{R}^k - \mathbf{Z}^k)\, d\Omega \\ & + \int_{\Gamma_\alpha} n_{\alpha,a} \left[\hat{\mathbf{L}}^k : \nabla(\delta\mathbf{u}^M) - \mathbf{Q}^k : (\mathbf{R}^k - \mathbf{Z}^k) \right] d\Gamma + \kappa_\infty \int_{\Gamma^{\beta s}_\alpha} n_{\alpha,a}\, \delta\mathbf{u}^m_\beta\, d\Gamma \Bigg\} - \Psi^{m,k}_\alpha\end{aligned} \tag{2.59}$$

where, $\Gamma^{\beta m}_\alpha \equiv \{\Gamma^\beta_\alpha \ | \beta \in I^m_\alpha\}$, $\Gamma^{\beta s}_\alpha \equiv \{\Gamma^\beta_\alpha \ | \beta \in I^s_\alpha\}$ and subscript B indicates the corresponding coarse scale element. Equations (2.52) and (2.56) constitute the linearized system of equations that are evaluated for the macro- and microscale problems. Each microscale problem defined over an enrichment domain is coupled to the macroscale problem as well as the enrichment domain problems that share a common boundary and has a master surface (i.e., all enrichment domain problems in I^s_α). The coupling is through the force vector (i.e., $\delta\mathbf{f}_\alpha(\hat{\mathbf{u}}^M, \{\delta\mathbf{u}^m_\beta | \beta \in I^s_\alpha\}$)). The macroscale problem is coupled to the enrichment domain problems (i.e., $\delta\mathbf{f}(\{\hat{\mathbf{u}}^m_\alpha\}^{n_{\text{en}}}_{\alpha=1})$). This coupled system of equations is evaluated using a staggered solution algorithm defined below.

2.4.3 Computational algorithm

The VME formulation for the elasto-viscoplastic problem is implemented using the C++ computer language with the commercial software package, Diffpack [68]. Diffpack is an object-oriented development framework for the numerical solution of partial differential equations. It provides a library of C++ classes to facilitate development of solution algorithms for complex

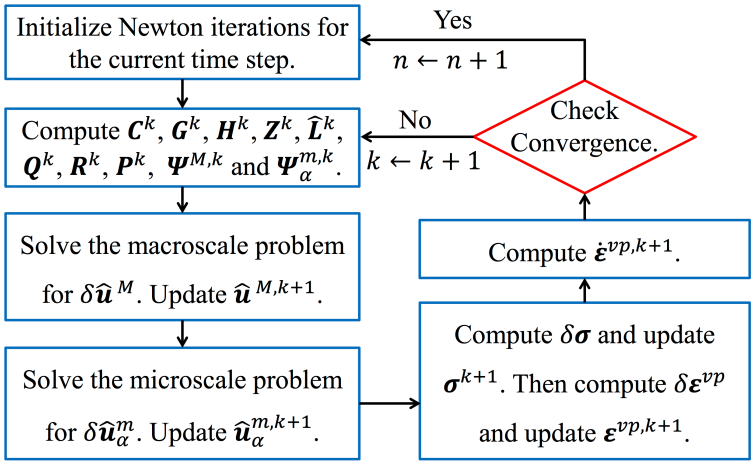

Figure 2.2: Solution algorithm

PDEs [68]. The overall solution strategy is to evaluate the coupled system of multiscale equations summarized in Fig. 2.2. At an arbitrary time ${}_nt$, the system is in equilibrium with the constitutive relations satisfied at macro- and microscale. The algorithm seeks to find the equilibrium state at ${}_{n+1}t$ as follows:

Given: ${}_n\hat{\mathbf{u}}^M, {}_n\hat{\mathbf{u}}_\alpha^m, {}_n\boldsymbol{\varepsilon}^{vp}, {}_n\dot{\boldsymbol{\varepsilon}}^{vp}, {}_n\boldsymbol{\sigma}$ at time ${}_nt$.

Find: $\hat{\mathbf{u}}^M, \hat{\mathbf{u}}_\alpha^m, \boldsymbol{\varepsilon}^{vp}, \dot{\boldsymbol{\varepsilon}}^{vp}, \boldsymbol{\sigma}$ at time ${}_{n+1}t$.

1. Initialize Newton iterations by setting: k=0, $\hat{\mathbf{u}}^{M,0} = {}_n\hat{\mathbf{u}}^M$, $\hat{\mathbf{u}}_\alpha^{m,0} = {}_n\hat{\mathbf{u}}_\alpha^m$, $\boldsymbol{\varepsilon}^{vp,0} = {}_n\boldsymbol{\varepsilon}^{vp}$, $\dot{\boldsymbol{\varepsilon}}^{vp,0} = {}_n\dot{\boldsymbol{\varepsilon}}^{vp}$, $\boldsymbol{\sigma}^0 = {}_n\boldsymbol{\sigma}$, and $\delta\mathbf{u}_\alpha^m = 0$, where $1 \leq \alpha \leq n_{\text{en}}$.

2. While not converged:

   a) Compute $\mathbf{C}^k$, $\mathbf{G}^k$, $\mathbf{H}^k$, $\mathbf{Z}^k$, $\hat{\mathbf{L}}^k$, $\mathbf{Q}^k$, $\mathbf{R}^k$, $\mathbf{P}^k$, $\boldsymbol{\Psi}^{M,k}$ and $\boldsymbol{\Psi}_\alpha^{m,k}$ for the multiscale system from Eqs. (2.38), (2.42a), (2.42b), (2.44), (2.45), (2.36), (2.35), (2.32) and (2.31), respectively.

   b) Solve the macroscale problem (Eq. (2.52)) for $\delta\hat{\mathbf{u}}^M$ over the structural domain, Ω, using the microscale increments $\delta\mathbf{u}_\alpha^m$ from the previous iteration.

   c) Update the macroscopic displacement coefficients, $\hat{\mathbf{u}}^{M,k+1} = \hat{\mathbf{u}}^{M,k} + \delta\hat{\mathbf{u}}^M$.

d) Solve the microscale problem (i.e., Eq. (2.56)) for $\delta\hat{\mathbf{u}}_\alpha^m$ over each enriched domain, Ω_α $(1 \leq \alpha \leq n_{\text{en}})$.

e) Update the microscopic displacement coefficients, $\hat{\mathbf{u}}_\alpha^{m,k+1} = \hat{\mathbf{u}}_\alpha^{m,k} + \delta\hat{\mathbf{u}}_\alpha^m$.

f) At every integration point in macro, and micro problems:

i) Employing $\delta\hat{\mathbf{u}}^M$ and $\delta\hat{\mathbf{u}}_\alpha^m$, compute current stress increment $\delta\boldsymbol{\sigma}$ using Eq. (2.43). Update stress $\boldsymbol{\sigma}^{k+1} = \boldsymbol{\sigma}^k + \delta\boldsymbol{\sigma}$.

ii) Compute $\delta\varepsilon^{vp}$ using Eq. (2.40). Update viscoplastic strain $\varepsilon^{vp,k+1} = \varepsilon^{vp,k} + \delta\varepsilon^{vp}$.

g) Compute viscoplastic strain rate $\dot{\varepsilon}^{vp,k+1}$ using Eq. (2.5).

h) Check for convergence at macroscale and microscale problems:

$$\begin{cases} \mathrm{e}^M & = \|\hat{\mathbf{u}}^{M,k+1} - \hat{\mathbf{u}}^{M,k}\|_2 \leq \text{Convergence tolerance} \\ \mathrm{e}_\alpha^m & = \|\hat{\mathbf{u}}_\alpha^{m,k+1} - \hat{\mathbf{u}}_\alpha^{m,k}\|_2 \leq \text{Convergence tolerance} \end{cases} \tag{2.60}$$

i) If convergence criterion are not satisfied, set iteration counter $k \leftarrow k+1$ and proceed with the next iteration.

3. Repeat step 2 with $n \leftarrow n+1$ until the end of the observation period.

The staggered form of the solution algorithm is achieved by solving the macroscale system using the microscale displacement coefficients from the previous iteration (Step 3b)). The staggering order, which is evaluating the macroscale problem prior to the microscale problems, is natural since the loading on the domain is expected to be primarily at the macroscale (i.e., typically but not necessarily $\hat{\mathbf{u}}_\alpha = 0$ on Γ_α^u and $\hat{\mathbf{t}}_\alpha = 0$ on Γ_α^t). The effect of stagger ordering does not have a notable effect on the solution. The convergence of the multiscale system is assessed when both the macroscale system and the enrichment domain problems simultaneously converge. A detailed convergence study on the staggered solution algorithm in the context of elasticity has been provided in Ref. [2] and not included in this chapter.

Table 2.1: Materials parameters for the verification studies of VME.

Material type	E [GPa]	ν	A [MPa]	B [MPa]	n	q	γ [MPa-hr]$^{-1}$
Phase I	130.8	0.32	600	1200	0.90	1.0	1.0
Phase II	110.8	0.32	400	200	0.96	1.0	1.0
Substrate	120.8	0.32	500	700	0.93	1.0	1.0

2.5 Numerical Verification

The implementation of the VME method for elasto-viscoplastic problems is verified using numerical simulations. The VME model predictions are compared to the direct numerical simulations using the finite element method. In the direct numerical simulations, the heterogeneities within the problem domain is fully resolved. In all simulations below, the domain is taken to consist of three separate materials. The heterogeneous material microstructure consists of two phases. A third material that approximates the properties of the composite domain is employed to idealize the behavior at the substrate domain. The material properties of the two phases and the substrate are provided in Table 2.1 and the constitutive relationship of these materials under unidirectional tension is plotted in Fig. 2.3.

The boundary condition parameter κ is relatively sensitive to the microstructural topology as well as the constituent material parameters. A sensitivity analysis and a parameter selection strategy are outlined in Ref. [23]. In this chapter, the selection of the boundary parameter is performed by subjecting a representative cell to pure uniaxial and shear loading, and choosing the boundary parameter which minimizes the discrepancy between the direct finite element analysis of the microstructure and the corresponding VME model (described in Section 2.5.1). The boundary parameter employed in the analysis of the specimen with a center notch (Section 2.5.2) uses the boundary parameter selected as such.

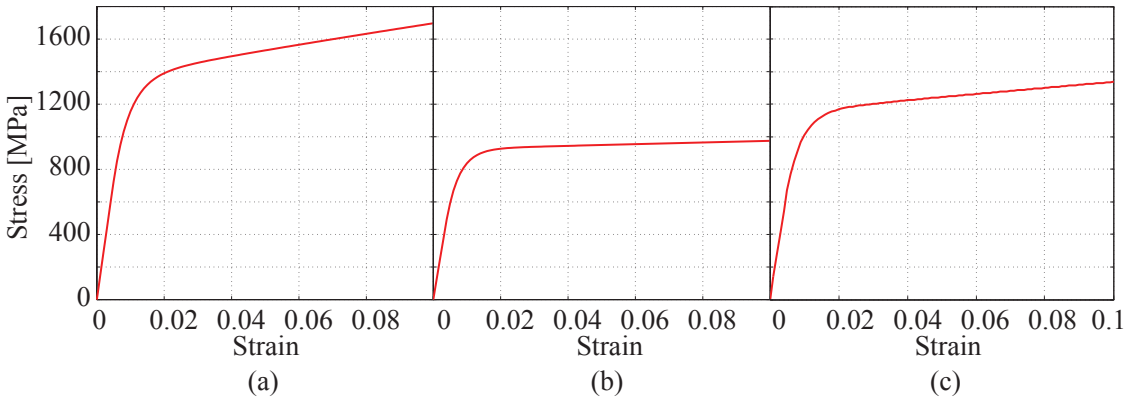

Figure 2.3: Stress-strain behavior of the constituent materials under uniaxial tension: (a) phase I; (b) phase II; and (c) substrate material.

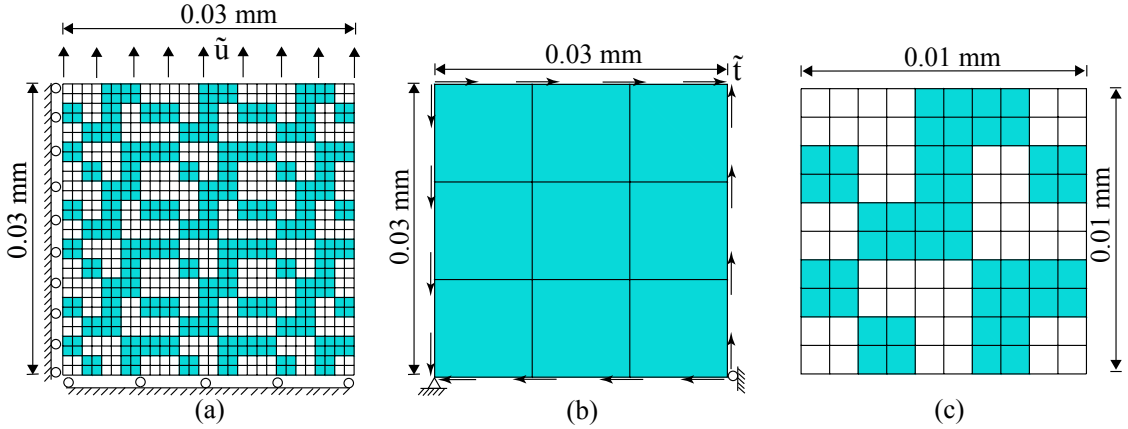

Figure 2.4: Numerical models of the square specimen: (a) direct finite element discretization and sketch for uniform tensile load; (b) macroscale discretization and sketch for pure shear load; and (c) microscale discretization of an enrichment domain.

2.5.1 Effect of the boundary parameter

In this section, the effect of the mixed boundary parameter, κ, on the accuracy characteristics of the VME method in the context of elasto-viscoplastic behavior is investigated. The effect of the mixed boundary parameter on composite media with elastic modulus contrast has been previously investigated in Ref. [23]. A 2-D plane strain, composite domain with a two-phase microstructure is considered as shown in Fig 2.4a. The geometry and the discretization used in the VME simulations are shown in Figs. 2.4b,c. The heterogeneity in the original problem domain is exactly obtained by the repetition of the microstructure (Fig. 2.4c) in a 3-by-3 tile. Phase I and phase II materials are identified as dark and light elements, respectively. The behavior of the square composite domain was investigated under displacement controlled uniform tension and shear conditions. The loading was applied at the uniform strain rate of approximately 3×10^{-4}/s. All 9 macroscale elements are taken to be enriched in the VME simulations, which means that the enrichment region is the entire problem domain. The ratio between the size of the enrichment domain and the specimen domain is 1/3 which exhibits the scale inseparable feature. The macroscale grid ensures that the central enriched domain has all four boundaries of inter-enrichment type. Each of the enrichment domains are discretized fine enough to ensure that further discretization does not noticeably affect the simulation accuracy. The direct finite element discretization and the microscale discretization are taken to have the same element size. The time step size is determined such that further refinement does not change the results significantly. The convergence tolerance employed in the simulations is set to 1×10^{-6}.

Figure 2.5 illustrates the time averaged errors in displacement and stress under tensile and shear loading conditions. The errors of the proposed multiscale method are compared to the direct finite element analysis as a function of the boundary parameter, κ. The error over the entire boundary

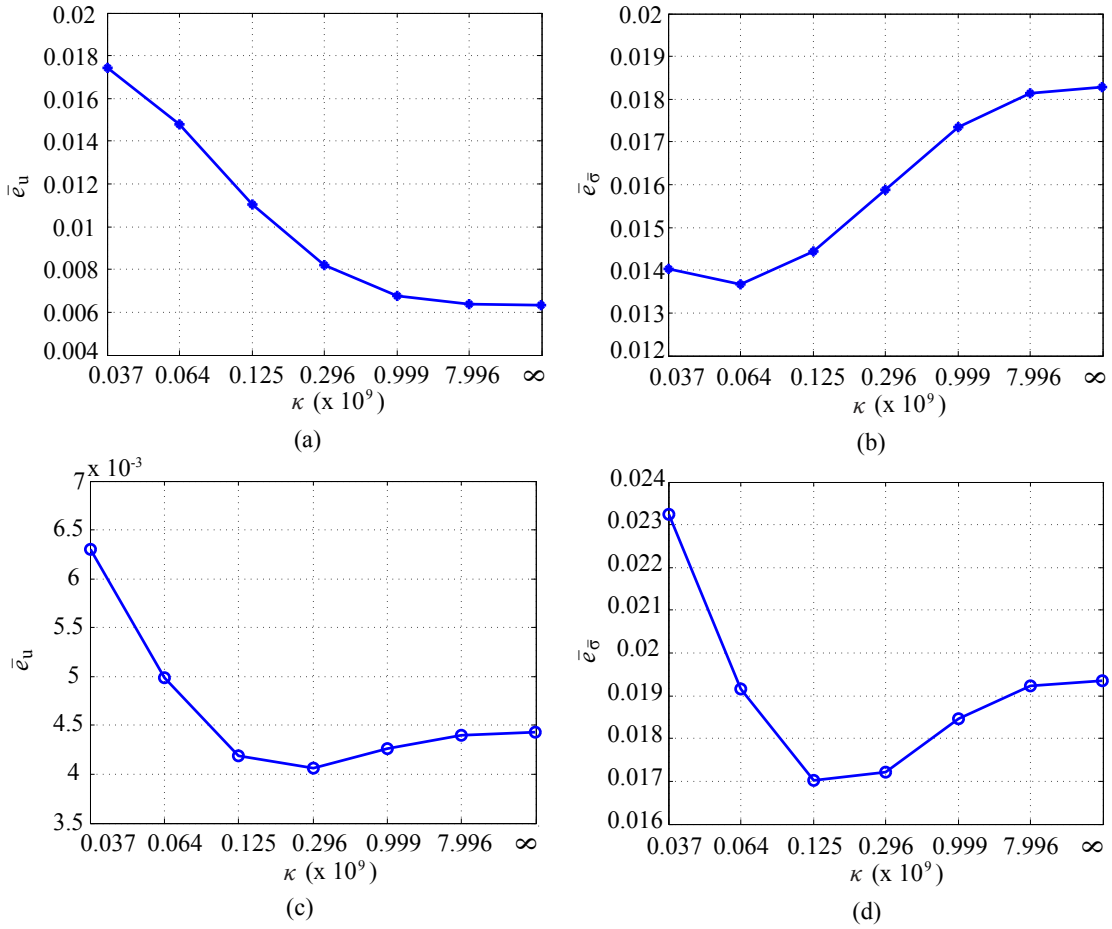

Figure 2.5: Time averaged error as a function of the boundary parameter: (a) displacement error under tensile loading; (b) equivalent stress error under tensile loading; (c) displacement error under shear loading; and (d) equivalent stress error under shear loading.

domain at an arbitrary time, t, is computed as:

$$e_\phi(t) = \frac{\sum_{\alpha=1}^{n_{\text{en}}} \left\| \phi^{\text{FEM}}(\mathbf{x},t) - \phi^{\text{VME}}(\mathbf{x},t) \right\|_{2,\Omega_\alpha}}{\sum_{\alpha=1}^{n_{\text{en}}} \left\| \phi^{\text{FEM}}(\mathbf{x},t) \right\|_{2,\Omega_\alpha}} \tag{2.61}$$

where, ϕ^{FEM} and ϕ^{VME} denotes a response field (i.e., displacement or equivalent stress) computed using the direct finite element method and the VME, respectively, $\|\cdot\|_{2,\Omega_\alpha}$ is the L_2 norm of the response field computed over Ω_α. When the numerical specimen is subjected to uniform tension, the displacement error is minimized when homogeneous Dirichlet boundary conditions are

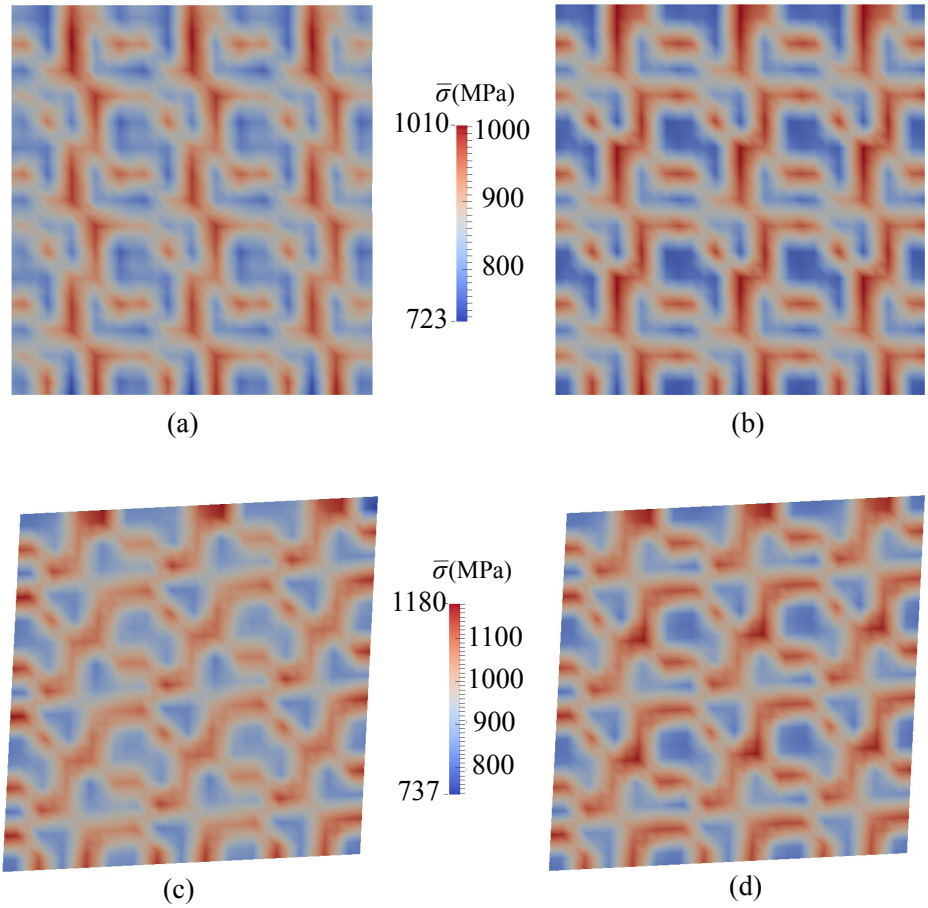

Figure 2.6: Equivalent stress contours at 3.0×10^{-4} mm applied displacement. (a) Reference model under uniform tension; (b) VME model under uniform tension; (c) reference model under shear; and (d) VME model under shear.

employed. In contrast, the time averaged error in the equivalent stress is minimized at a slightly relaxed boundary parameter with $\kappa \in [3.7 \times 10^7, 1.25 \times 10^8]$. Under the shear load, the displacement and equivalent stress errors are minimized at the boundary parameter values of $\kappa = 2.96 \times 10^8$ and $\kappa = 1.25 \times 10^8$, respectively. The results indicate limited improvement of accuracy in the displacement and stress fields when the boundary condition is slightly relaxed from the homogeneous Dirichlet conditions. In the case of uniaxial tension loading, the errors in the stress computations improve by approximately 32% when the optimal boundary parameter is employed. The trends in errors follow a similar trend to those computed in the context of elasticity problems provided in Ref. [23]. Figures 2.6a,b compare the contours of equivalent stress fields computed by the proposed model and the direct finite element method at time $t = 36$ seconds and under an applied

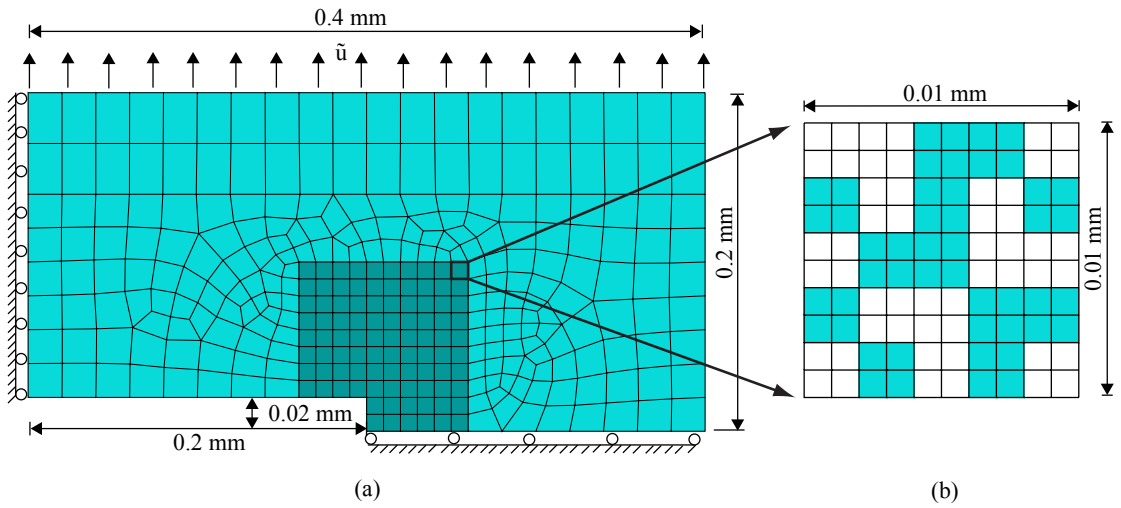

Figure 2.7: Multiscale variational enrichment model of the specimen with a notch: (a) sketch and discretization of the macroscale discretization; and (b) microscale discretization of an enrichment domain in the enrichment region.

uniform tensile displacement of 3.0×10^{-4} mm. Equivalent contours at $t = 36$ seconds and under an applied shear displacement of 3.0×10^{-4} mm are shown in Figs. 2.6c,d for the VME and direct FEM methods, respectively. The contours from the VME simulations are reconstructed from the micro- and macroscale solutions at the post-processing stage. In both cases, there is a close agreement in the stress fields computed by the reference and the multiscale simulations.

2.5.2 Specimen with a center notch

The proposed multiscale method is further verified using the numerical analysis of a specimen with a center notch subjected to uniform tensile loading in the vertical direction. The dimensions of the rectangular specimen and the center notch are 0.8 mm $\times$ 0.4 mm with a 0.4 mm $\times$ 0.04 mm, respectively. The ratio between the size of the enrichment domain and the stress localization region around the corner is approximately 1/10 which exhibits the scale inseparable nature. Due to symmetry, only a quarter of the specimen is modeled. The two-phase microstructure of the domain and the material properties of the phases are taken to be identical to the example provided in Section 2.5.1. The specimen was subjected to uniform displacement controlled tensile loading

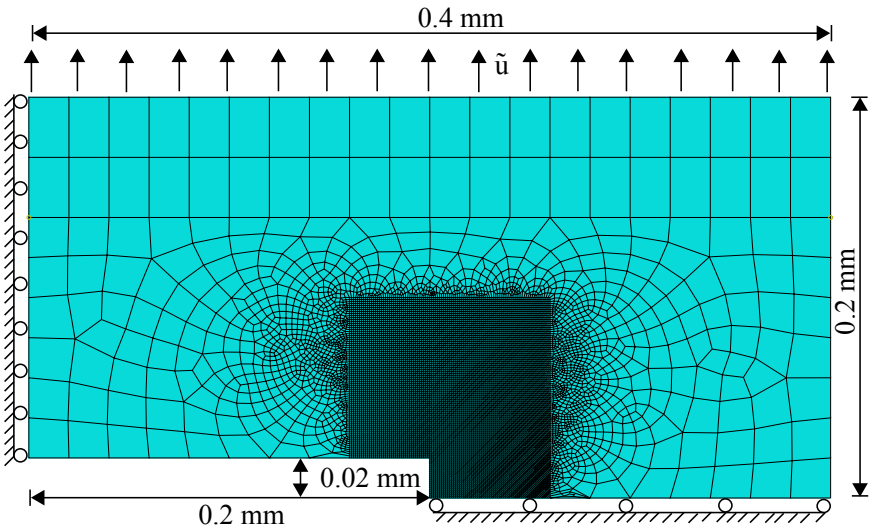

Figure 2.8: Discretization of the direct finite element model of the notched specimen.

in the vertical direction. The maximum amplitude of the loading was 0.01 mm applied at a rate of 5.6×10^{-5} mm/sec.

The geometry, boundary conditions of the problem domain, as well as the macro- and microscale discretization employed in the VME approach is shown in Fig. 2.7. A 0.1 mm $\times$ 0.1 mm square domain at the center of the specimen is chosen as the enrichment region. The macroscale mesh consists of 314 quadrilateral macroscale elements, 92 of which are enriched. Each enriched element is associated with an identical microscale geometry shown in Fig. 2.7b. The microscale mesh consists of 100 quadrilateral elements. Outside the enrichment region (i.e., the substrate region), substrate material properties shown in Table 2.1 are employed. The VME simulations were conducted using homogeneous Dirichlet boundary conditions, as well as using the mixed boundary conditions with $\kappa = 2.96 \times 10^8$. The optimal mixed boundary parameter identified under the shear loading in the previous section is employed since the plastic deformation occurs under shear. The performance of the VME approach was assessed by comparing the model results to the direct numerical simulations, in which the enrichment region is fully resolved. The reference mesh is shown in Fig. 2.8 and consists of 11276 quadrilateral elements. The size of the elements within the enrichment domain is taken to be the same as the size of the elements in the microscale mesh used in the VME approach. The substrate region is meshed with coarser elements. A transition region

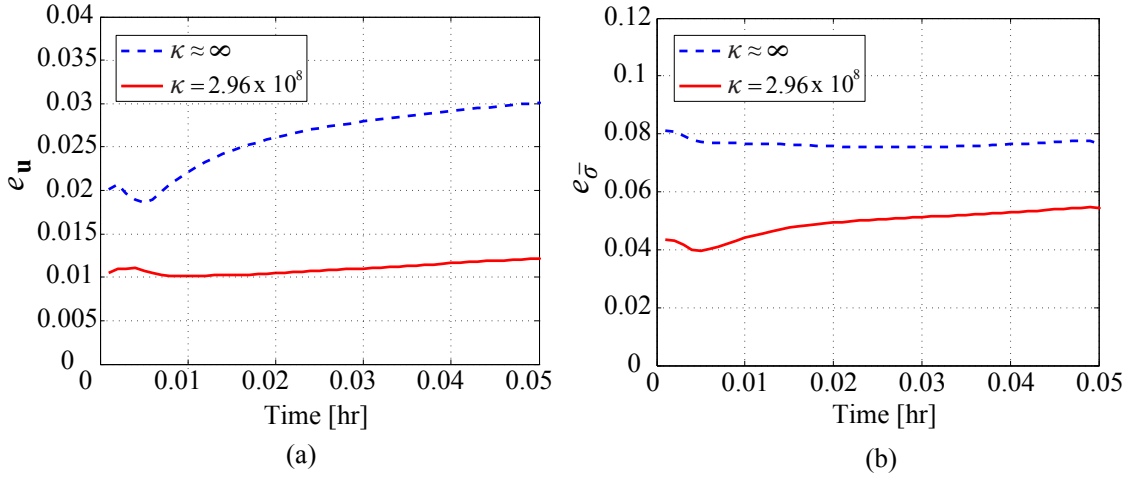

Figure 2.9: Errors as a function of simulation time: (a) error in displacement; and (b) error in equivalent stress.

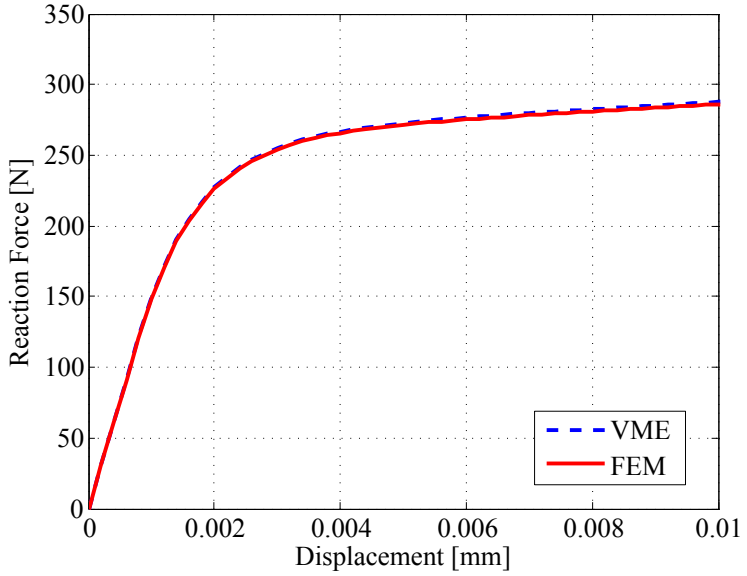

Figure 2.10: Overall reaction force - displacement comparison between the reference simulation and the VME method.

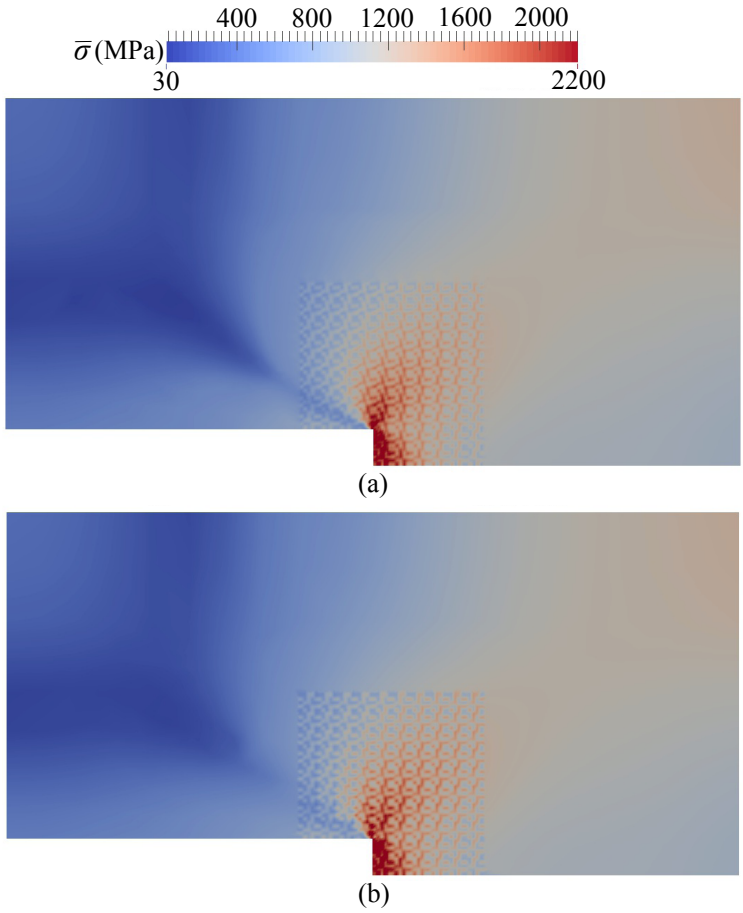

Figure 2.11: Comparison of equivalent stress contours at the end of the simulation: (a) reference model; and (b) the VME method with $\kappa = 2.96 \times 10^8$.

is included to ensure mesh conformity.

Figure 2.9 illustrates the evolution of the errors in the displacement and equivalent stress within the enrichment region as a function of simulation time. The errors are computed using Eq. (2.61). The figure includes the VME simulations performed using the homogeneous Dirichlet and optimal shear boundary conditions. The errors in the displacement computed using the homogeneous Dirichlet and the optimal shear boundary conditions remained within 3% and 1.5%, respectively. The errors in the stress computed using the two boundary conditions are within 8.5% and 6%, respectively. In the case of the homogeneous Dirichlet boundary conditions, the displacement errors accumulate as a function of increasing plastic strain, whereas the optimal shear boundary condition has less sensitivity to the plastic strain magnitude. The proposed multiscale approach has

reasonable accuracy characteristics compared to the reference model for both types of boundary conditions.

Figure 2.10 shows the comparison of the overall force displacement curves computed using the reference finite element method and the proposed VME method. The VME simulations performed using the two types of boundary conditions resulted in near identical force-displacement curves. Figure 2.10 clearly shows that the proposed approach is able to accurately capture the overall elasto-viscoplastic response. In addition to the overall behavior, the local deformation and stresses are very accurately captured using the proposed VME approach. The equivalent stress contours obtained based on the reference and the VME method are compared in Fig. 2.11. The equivalent stress contours correspond to the applied peak load at the end of the simulations. The stress contours for the VME approach is reconstructed using the enrichment domain solutions at the post-processing stage. The local stress distributions show an oscillatory behavior around the notch tip, due to the heterogeneous microstructure. The oscillatory behavior is well captured using the proposed VME approach, pointing to its ability to reproduce the local stress fields within the critical regions of the problem domain.

Chapter 3

REDUCED ORDER VARIATIONAL MULTISCALE ENRICHMENT METHOD FOR ELASTO-VISCOPLASTIC PROBLEMS

3.1 Introduction

The numerical assessment of the VME microscale problems could be computationally expensive, especially when the geometry of the microstructure is complicated and the number of enrichment domains is large. In the current chapter, we provide a reduced order modeling approach for the VME method to address global-local problems in a more efficient manner. The proposed model order reduction approach is based on the concepts of transformation field analysis pioneered by Dvorak and coworkers [31]. The main idea is to express the response field as a function of influence functions and coefficient tensors that are computed at the preprocessing stage prior to a structural analysis. The influence functions ensure that the microstructural equilibrium is a-priori satisfied for arbitrary states of deformation. While this approach has been previously applied in the context of computational homogenization [34, 37, 69], it has not been previously formulated for scale inseparable multiscale methods. This chapter presents the reduced order variational multiscale enrichment (ROVME) formulation for heterogeneous materials that exhibit elasto-viscoplastic behavior. The implementation procedure and numerical approaches employed are described. The proposed ROVME approach is thoroughly verified against the direct variational multiscale enrichment method [24]. The proposed approach is able to capture the local and global response mechanisms with reasonable accuracy at the fraction of the cost.

This chapter provides the following novel contributions: (1) The eigenstrain-based reduced order modeling approach is extended to scale inseparable problems; (2) The local problem within the VME framework is evaluated based on a much reduced approximation basis without significant loss in accuracy; and (3) The ROVME approach provides the ability to control efficiency/accuracy characteristics since the model order is controlled within the reduced order modeling framework.

The remainder of this chapter is organized as follows: Section 3.2 presents the reduced order VME formulation for inelastic mechanical problems with elasto-viscoplastic material behavior. Section 3.3 illustrates the implementation strategy of the ROVME methodology. Section 3.4 presents the numerical verification studies including global-local response and assessment of computation efficiency.

3.2 Reduced Order Variational Multiscale Enrichment (ROVME)

In the current section, an eigenstrain-based model reduction technique [37] is employed for efficient evaluation of the microscale problems. The governing equations are identical to those provided in Chapter 2. The only difference in the current chapter is the homogeneous Dirichlet boundary conditions for the enrichment domains are employed (Eq. (2.25)), instead of the mixed boundary conditions. The resulting macroscale weak form is obtained as:

$$\int_{\Omega} \nabla \mathbf{w}^M : \boldsymbol{\sigma} \, d\Omega - \int_{\Gamma^t} \mathbf{w}^M \cdot \tilde{\mathbf{t}} \, d\Gamma = 0 \tag{3.1}$$

The weak form of the microscale problem at an arbitrary enrichment domain, α, yields:

$$\int_{\Omega_\alpha} \nabla \mathbf{w}^m_\alpha : \boldsymbol{\sigma} \, d\Omega = 0; \quad \alpha = 1,2,...n_{\text{en}}. \tag{3.2}$$

3.2.1 Numerical evaluation of the microscale problem

We start by decomposing the microscale displacement field as follows:

$$\mathbf{u}^m_\alpha(\mathbf{x},t) = \sum_{A=1}^{N_D} \mathbf{H}^\alpha_A(\mathbf{x}) \cdot \hat{\mathbf{u}}^{M\alpha}_A(t) + \int_{\Omega_\alpha} \mathbf{h}^\alpha(\mathbf{x},\hat{\mathbf{x}}) : \varepsilon^{vp}(\hat{\mathbf{x}},t) \, d\hat{\mathbf{x}} \tag{3.3}$$

where, $\hat{\mathbf{u}}^{M\alpha}_A$ denotes the macroscale nodal coefficient corresponding to the A^{th} node of the enrichment domain, Ω_α. $\mathbf{H}^\alpha_A$, a second order tensor, is the linear elastic influence function in Ω_α. $\mathbf{h}^\alpha(\mathbf{x},\hat{\mathbf{x}})$ $(\mathbf{x},\hat{\mathbf{x}} \in \Omega_\alpha)$, a third order tensor, is the influence function associated with the inelastic de-

formation within the enrichment domain. In the absence of inelastic processes, the second term on the right hand side of Eq. (3.3) vanishes. The microscale displacement field is then expressed using influence functions ($\mathbf{H}_A^\alpha$) acting on the finite element basis (described by the nodal coefficients of the macroscale element over the enrichment domain) leveraging the linearity of the problem as proposed by Refs. [21, 22]. In the presence of inelastic deformation, the second component is obtained by considering the inelastic strain field as spatially variable force acting on the microstructure, and using the Green's function idea to compute the microscale displacement contribution as a function of the spatially variable inelastic strain (eigenstrain) field [70]. Equation (3.3) is valid under the conditions of small deformation theory and additive split of the strain tensor. In the presence of geometric nonlinearity and plasticity models that employ multiplicative split, this decomposition is not directly valid as the inelastic influence functions become time (or load amplitude) dependent.

The influence functions $\mathbf{H}_A^\alpha$ and $\mathbf{h}^\alpha$ are determined from the microscale weak form shown in Eq. (3.2). Employing the constitutive equation (i.e., Eq. (2.22)) and the microscale displacement field discretization defined in Eq. (3.3), the weak form of the microscale problem becomes ($\alpha = 1, 2, ...n_{\text{en}}$):

$$\begin{aligned}\sum_{A=1}^{N_D}\left[\left(\int_{\Omega_\alpha}\nabla\mathbf{w}_\alpha^m:\mathbf{L}:\nabla\mathbf{H}_A^\alpha\,d\Omega+\int_{\Omega_\alpha}\nabla\mathbf{w}_\alpha^m:\mathbf{L}\cdot\nabla N_A\,d\Omega\right)\cdot\hat{\mathbf{u}}_A^{M\alpha}(t)\right]\\+\int_{\Omega_\alpha}\nabla\mathbf{w}_\alpha^m:\mathbf{L}:\left[\int_{\Omega_\alpha}\nabla\mathbf{h}^\alpha(\mathbf{x},\hat{\mathbf{x}}):\boldsymbol{\varepsilon}^{vp}(\hat{\mathbf{x}},t)\,d\hat{\mathbf{x}}-\boldsymbol{\varepsilon}^{vp}(\mathbf{x},t)\right]\,d\Omega=0\end{aligned}\tag{3.4}$$

Considering the elastic state (i.e., when the enrichment domain undergoes deformation in the absence of the inelastic process), Eq. (3.4) is reduced to:

$$\sum_{A=1}^{N_D}\left[\left(\int_{\Omega_\alpha}\nabla\mathbf{w}_\alpha^m:\mathbf{L}:\nabla\mathbf{H}_A^\alpha\,d\Omega+\int_{\Omega_\alpha}\nabla\mathbf{w}_\alpha^m:\mathbf{L}\cdot\nabla N_A\,d\Omega\right)\cdot\hat{\mathbf{u}}_A^{M\alpha}(t)\right]=0\tag{3.5}$$

We note that the displacement coefficients, $\hat{\mathbf{u}}_A^M$ vary with time only, while $\nabla\mathbf{w}_\alpha^m$ and ∇N_A are functions of the space coordinates with no variation in time. The governing equation for the linear-

elastic influence function, $\mathbf{H}_A^\alpha$, then becomes:

$$\int_{\Omega_\alpha} \nabla \mathbf{w}_\alpha^m : \mathbf{L} : \nabla \mathbf{H}_A^\alpha \, d\Omega = \; - \int_{\Omega_\alpha} \nabla \mathbf{w}_\alpha^m : \mathbf{L} \cdot \nabla N_A \, d\Omega; \quad \forall \, A = 1,2,...,N_D \tag{3.6}$$

In the presence of inelastic deformation and in view of Eq. (3.5), Eq. (3.4) yields:

$$\int_{\Omega_\alpha} \nabla \mathbf{w}_\alpha^m : \mathbf{L} : \left[\int_{\Omega_\alpha} \nabla \mathbf{h}^\alpha(\mathbf{x}, \hat{\mathbf{x}}) : \varepsilon^{vp}(\hat{\mathbf{x}}, t) \, d\hat{\mathbf{x}} - \varepsilon^{vp}(\mathbf{x}, t) \right] \, d\Omega = 0 \tag{3.7}$$

The viscoplastic strain field within the enrichment domain Ω_α is expressed as:

$$\varepsilon^{vp}(\mathbf{x}, t) = \int_{\Omega_\alpha} \delta^d(\mathbf{x} - \hat{\mathbf{x}}) \varepsilon^{vp}(\hat{\mathbf{x}}, t) \, d\hat{\mathbf{x}}; \quad \forall \mathbf{x} \in \Omega_\alpha \tag{3.8}$$

where δ^d denotes the Dirac delta distribution. Substituting Eq. (3.8) into Eq. (3.7) yields the weak form equation for the inelastic influence function $\mathbf{h}^\alpha(\mathbf{x}, \hat{\mathbf{x}})$:

$$\int_{\Omega_\alpha} \nabla \mathbf{w}_\alpha^m : \mathbf{L} : \nabla \mathbf{h}^\alpha(\mathbf{x}, \hat{\mathbf{x}}) \, d\Omega = \int_{\Omega_\alpha} \nabla \mathbf{w}_\alpha^m : \mathbf{L} \; \delta^d(\mathbf{x} - \hat{\mathbf{x}}) \, d\Omega; \quad \forall \hat{\mathbf{x}} \in \Omega_\alpha \tag{3.9}$$

The influence functions, $\mathbf{H}_A^\alpha$ and $\mathbf{h}^\alpha$, are evaluated numerically. The detailed finite element solution of Eq. (3.6) is provided in [21, 22]. The numerical evaluation of the inelastic influence function, involving the approximation of the Dirac distribution and the details of a numerical treatment, is provided in Ref. [37]. Representing the microscale displacement field with the influence functions $\mathbf{H}_A^\alpha$ $(A = 1,2,...,N_D)$ and $\mathbf{h}^\alpha$, the microscale weak form, Eq. (3.4), is automatically satisfied for arbitrary inelastic strain of macroscale displacement states.

3.2.2 Reduced order microscale problem

The total number of degrees of freedom in the enrichment domain problem is reduced by replacing the fully resolved microscale discretization with a reduced order microscale partitioning. The reduced order partitioning is performed such that each enrichment domain is decomposed into

NP_α subdomains (parts):

$$\Omega_\alpha = \bigcup_{\gamma=1}^{NP_\alpha} \Omega_\gamma^\alpha; \;\; \Omega_\gamma^\alpha \cap \Omega_\eta^\alpha \equiv \emptyset \;\text{ when }\; \gamma \neq \eta \tag{3.10}$$

where γ and η are the indices of parts in an arbitrary enrichment domain Ω_α. The stress and inelastic strain fields are discretized using the separation of variables as [37]:

$$\boldsymbol{\sigma}(\mathbf{x},t) = \sum_{\gamma=1}^{NP_\alpha} N_\gamma^\alpha(\mathbf{x})\; \boldsymbol{\sigma}_\gamma^\alpha(t); \quad \boldsymbol{\varepsilon}^{vp}(\mathbf{x},t) = \sum_{\gamma=1}^{NP_\alpha} N_\gamma^\alpha(\mathbf{x})\; \boldsymbol{\mu}_\gamma^\alpha(t); \quad \mathbf{x} \in \Omega_\alpha \tag{3.11}$$

where, $\boldsymbol{\sigma}_\gamma^\alpha$ and $\boldsymbol{\mu}_\gamma^\alpha$ are the stress and inelastic strain coefficients, respectively. N_γ^α denotes shape function associated with part Ω_γ^α, such that:

$$N_\gamma^\alpha(\mathbf{x}) = \begin{cases} 1, & \text{if } \mathbf{x} \in \Omega_\gamma^\alpha \\ 0, & \text{elsewhere} \end{cases} \tag{3.12}$$

The above discretization therefore leads to a piecewise constant approximation of the stress and inelastic strain fields over the enrichment domain. The stress and inelastic strain fields are discontinuous within the enrichment domain, which is consistent with the C^0 continuous finite element approximation of the displacement field. For instance, as the number of parts NP_α reaches the number of elements in the microscale discretization for constant strain elements, the approximations are of the same order. Substituting the reduced order microscale partitioning (Eq. (3.11)) into Eq. (3.3), the microscale displacement field becomes:

$$\begin{aligned} \mathbf{u}_\alpha^m(\mathbf{x},t) &= \sum_{A=1}^{N_D} \mathbf{H}_A^\alpha(\mathbf{x}) \cdot \hat{\mathbf{u}}_A^{M\alpha}(t) + \sum_{\gamma=1}^{NP_\alpha} \left[\int_{\Omega^\alpha} \mathbf{h}^\alpha(\mathbf{x},\hat{\mathbf{x}})\; N_\gamma^\alpha(\mathbf{x})\; d\hat{\mathbf{x}} : \boldsymbol{\mu}_\gamma^\alpha(t) \right] \\ &= \sum_{A=1}^{N_D} \mathbf{H}_A^\alpha(\mathbf{x}) \cdot \hat{\mathbf{u}}_A^{M\alpha}(t) + \sum_{\gamma=1}^{NP_\alpha} \left[\int_{\Omega_\gamma^\alpha} \mathbf{h}^\alpha(\mathbf{x},\hat{\mathbf{x}})\; d\hat{\mathbf{x}} : \boldsymbol{\mu}_\gamma^\alpha(t) \right] \end{aligned} \tag{3.13}$$

Similarly, substituting Eq. (3.11) into Eq. (2.22), the constitutive equation for enrichment domain Ω_α yields:

$$\sum_{\gamma=1}^{NP_\alpha} N_\gamma^\alpha(\mathbf{x})\ \boldsymbol{\sigma}_\gamma^\alpha(t) = \sum_{A=1}^{N_D} \mathbf{S}_A^\alpha(\mathbf{x}) \cdot \hat{\mathbf{u}}_A^{M\alpha}(t) + \sum_{\gamma=1}^{NP_\alpha} \mathbf{P}_\gamma^\alpha(\mathbf{x}) : \boldsymbol{\mu}_\gamma^\alpha(t) \tag{3.14}$$

in which, the coefficient tensors are defined for an arbitrary enrichment domain Ω_α ($\alpha = 1,2,...,n_{\text{en}}$):

$$\mathbf{S}_A^\alpha(\mathbf{x}) = \mathbf{L}(\mathbf{x}) \cdot \nabla N_A(\mathbf{x}) + \mathbf{L}(\mathbf{x}) : \nabla \mathbf{H}_A^\alpha(\mathbf{x}); \quad \forall\, A = 1,2,...,N_D \tag{3.15}$$

and for each part Ω_γ^α ($\gamma = 1,2,...,NP_\alpha$):

$$\mathbf{P}_\gamma^\alpha(\mathbf{x}) = \mathbf{L}(\mathbf{x}) : \int_{\Omega_\gamma^\alpha} \nabla \mathbf{h}^\alpha(\mathbf{x},\hat{\mathbf{x}})\ d\hat{\mathbf{x}} - \mathbf{L}(\mathbf{x})\ N_\gamma^\alpha(\mathbf{x}) \tag{3.16}$$

Integrating both sides of Eq. (3.14) over part Ω_η^α of enrichment domain Ω_α, the constitutive equation on part η ($\mathbf{x} \in \Omega_\eta^\alpha$) is simplified to:

$$\boldsymbol{\sigma}_\eta^\alpha(t) = \sum_{A=1}^{N_D} \mathbf{S}_{\eta A}^\alpha \cdot \hat{\mathbf{u}}_A^{M\alpha}(t) + \sum_{\gamma=1}^{NP_\alpha} \mathbf{P}_{\eta\gamma}^\alpha : \boldsymbol{\mu}_\gamma^\alpha(t) \tag{3.17}$$

Since the stress and inelastic strain coefficients are constant on each part, the homogenized coefficient tensors on each part Ω_η^α within the enrichment domain Ω_α is defined as:

$$\mathbf{S}_{\eta A}^\alpha = \frac{1}{|\Omega_\eta^\alpha|} \int_{\Omega_\eta^\alpha} \mathbf{S}_A^\alpha(\mathbf{x})\ d\Omega; \quad \mathbf{x} \in \Omega_\eta^\alpha \tag{3.18}$$

$$\mathbf{P}_{\eta\gamma}^\alpha = \frac{1}{|\Omega_\eta^\alpha|} \int_{\Omega_\eta^\alpha} \mathbf{P}_\gamma^\alpha(\mathbf{x})\ d\Omega; \quad \mathbf{x} \in \Omega_\eta^\alpha \tag{3.19}$$

The time-independent coefficient tensors, $\mathbf{S}_{\eta A}^\alpha$ and $\mathbf{P}_{\eta\gamma}^\alpha$, are obtained using the influence functions, $\mathbf{H}_A^\alpha$ and $\mathbf{h}^\alpha$. Since the influence functions satisfy the microscale equilibrium, as discussed in Section 3.1, the stresses computed using the coefficient tensors, $\mathbf{S}_{\eta A}^\alpha$ and $\mathbf{P}_{\eta\gamma}^\alpha$, automatically satisfy microscale equilibrium for arbitrary macroscale displacement and inelastic strain coefficients. The

corresponding rate-form constitutive equation is:

$$\dot{\boldsymbol{\sigma}}_{\eta}^{\alpha}(t) = \sum_{A=1}^{N_D} \mathbf{S}_{\eta A}^{\alpha} \cdot \hat{\dot{\mathbf{u}}}_{A}^{M\alpha}(t) + \sum_{\gamma=1}^{NP_\alpha} \mathbf{P}_{\eta\gamma}^{\alpha} : \dot{\boldsymbol{\mu}}_{\gamma}^{\alpha}(t) \tag{3.20}$$

3.3 Computational Implementation

This section provides the detailed decomposition of the numerical implementation of the reduced order variational multiscale enrichment method, including the implementation of the reduced order microscale problem, upscaled macroscale problem and a solution algorithm.

A Newton-Raphson iterative scheme is employed to numerically assess the elasto-viscoplastic problem described in this chapter. Considering the discrete set of instances with the observation period: $\{0, {}_1t, {}_2t, ..., {}_nt, {}_{n+1}t, ..., t_o\}$ and employing the rate form of the inelastic strain coefficients (i.e., Eq. (3.11)) for each part Ω_{γ}^{α} in the enrichment domain Ω_{α}, The viscoplastic slip evolution equation (Eq. (2.34)) is equivalent to:

$$\dot{\boldsymbol{\mu}}_{\gamma}^{\alpha}(t) = (1-\theta)\ \dot{\boldsymbol{\mu}}_{\gamma}^{\alpha}(\mathbf{x}, {}_nt) + \theta\ \dot{\boldsymbol{\mu}}_{\gamma}^{\alpha}(\mathbf{x}, {}_{n+1}t); \quad t \in [{}_nt,\ {}_{n+1}t] \tag{3.21}$$

The left subscript n and $n+1$ indicate the value of a field variable at ${}_nt$ and ${}_{n+1}t$, respectively. Correspondingly, the evolution equation for the inelastic coefficient, $\dot{\boldsymbol{\mu}}_{\gamma}^{\alpha}$, is obtained from Eq. (2.5) as:

$$\dot{\boldsymbol{\mu}}_{\gamma}^{\alpha}(\boldsymbol{\sigma}_{\gamma}^{\alpha}, \boldsymbol{\mu}_{\gamma}^{\alpha}) = \gamma \left\langle \frac{\sqrt{3}\bar{\sigma}(\boldsymbol{\sigma}_{\gamma}^{\alpha}) - \sigma_y(\boldsymbol{\mu}_{\gamma}^{\alpha})}{\sigma_y(\boldsymbol{\mu}_{\gamma}^{\alpha})} \right\rangle^{q} \frac{\partial f(\boldsymbol{\sigma}_{\gamma}^{\alpha}, \boldsymbol{\mu}_{\gamma}^{\alpha})}{\partial \boldsymbol{\sigma}_{\gamma}^{\alpha}} \tag{3.22}$$

3.3.1 Numerical evaluation of the reduced order microscale problem

The nonlinear microscale problem defined by Eqs. (3.20), (3.21) and (3.22) is evaluated using the Newton-Raphson iterative scheme. Substituting Eq. (3.21) into Eq. (3.20), the time discretiza-

tion of the residual of the constitutive equation for an arbitrary part Ω_η^α becomes:

$$\begin{aligned}\mathbf{R}_\eta^\alpha \equiv\ & {}_{n+1}\boldsymbol{\sigma}_\eta^\alpha - {}_n\boldsymbol{\sigma}_\eta^\alpha - \sum_{A=1}^{N_D} \mathbf{S}_{\eta A}^\alpha \cdot \left({}_{n+1}\hat{\mathbf{u}}_A^{M\alpha} - {}_n\hat{\mathbf{u}}_A^{M\alpha}\right) \\ & - (1-\theta)\,\Delta t \sum_{\gamma=1}^{NP_\alpha} \mathbf{P}_{\eta\gamma}^\alpha : {}_n\dot{\boldsymbol{\mu}}_\gamma^\alpha - \theta\,\Delta t \sum_{\gamma=1}^{NP_\alpha} \mathbf{P}_{\eta\gamma}^\alpha : {}_{n+1}\dot{\boldsymbol{\mu}}_\gamma^\alpha = 0\end{aligned} \tag{3.23}$$

In what follows, the left subscript $n+1$ of the fields at current configuration is omitted for clarity of presentation. Considering a first order Taylor series approximation of Eq. (3.23) and forming a Newton iteration yield the following residual for the stress-strain equation:

$$\begin{aligned}\mathbf{R}_\eta^{\alpha,k+1} \approx \mathbf{R}_\eta^{\alpha,k} + & \sum_{\gamma=1}^{NP_\alpha} \left[\left(\delta_{\eta\gamma}^K \mathbf{I} - \theta\,\Delta t\, \mathbf{P}_{\eta\gamma}^\alpha : \mathbf{C}_\gamma^{\alpha,k}\right) : \delta\boldsymbol{\sigma}_\gamma^\alpha\right] \\ & - \theta\,\Delta t \sum_{\gamma=1}^{NP_\alpha} \left[\mathbf{P}_{\eta\gamma}^\alpha : \mathbf{G}_\gamma^{\alpha,k} : \delta\boldsymbol{\mu}_\gamma^\alpha\right] - \sum_{A=1}^{N_D} \left[\mathbf{S}_{\eta A}^\alpha \cdot \delta\hat{\mathbf{u}}_A^{M\alpha}\right] = 0\end{aligned} \tag{3.24}$$

in which, superscript k denotes Newton iteration counter; $\delta(\cdot)$ indicates the increment of response field $(\cdot)$ during the current iteration (e.g., $\delta\hat{\mathbf{u}}_A^M = \hat{\mathbf{u}}_A^{M,k+1} - \hat{\mathbf{u}}_A^{M,k}$). $\delta_{\eta\gamma}^K$ is the Kronecker delta; $\mathbf{I}$ the fourth order identity tensor; and

$$\mathbf{C}_\gamma^{\alpha,k} = \left(\frac{\partial\dot{\boldsymbol{\mu}}_\gamma^\alpha}{\partial\boldsymbol{\sigma}_\gamma^\alpha}\right)^k; \quad \mathbf{G}_\gamma^{\alpha,k} = \left(\frac{\partial\dot{\boldsymbol{\mu}}_\gamma^\alpha}{\partial\boldsymbol{\mu}_\gamma^\alpha}\right)^k \tag{3.25}$$

The explicit expressions for $\mathbf{C}_\gamma^{\alpha,k}$ and $\mathbf{G}_\gamma^{\alpha,k}$ are provided in Ref. [39]. Note $\mathbf{C}_\gamma^{\alpha,k}$ and $\mathbf{G}_\gamma^{\alpha,k}$ are constant over each part Ω_γ^α.

The residual of the kinematic equation (i.e., Eq. (3.21)) is defined as:

$$\boldsymbol{\lambda}_\gamma^\alpha \equiv \boldsymbol{\mu}_\gamma^\alpha - {}_n\boldsymbol{\mu}_\gamma^\alpha - \Delta t\,(1-\theta)\,{}_n\dot{\boldsymbol{\mu}}_\gamma^\alpha - \Delta t\,\theta\,\dot{\boldsymbol{\mu}}_\gamma^\alpha = 0 \tag{3.26}$$

Expanding Eq. (3.26) using the first order Taylor series approximation, the inelastic coefficient

increment at the current Newton iteration is expressed in terms of the stress coefficient as:

$$\delta\boldsymbol{\mu}_{\gamma}^{\alpha}=\left(\mathbf{I}-\theta\ \Delta t\ \mathbf{G}_{\gamma}^{\alpha,k}\right)^{-1}:\left(\theta\ \Delta t\ \mathbf{C}_{\gamma}^{\alpha,k}\right):\delta\boldsymbol{\sigma}_{\gamma}^{\alpha}-\left(\mathbf{I}-\theta\ \Delta t\ \mathbf{G}_{\gamma}^{\alpha,k}\right)^{-1}:\boldsymbol{\lambda}_{\gamma}^{\alpha,k} \tag{3.27}$$

Substituting Eq. (3.27) into Eq. (3.24), the inelastic coefficients are condensed out to yield:

$$\sum_{\gamma=1}^{NP_{\alpha}}\left(\mathbf{Q}_{\eta\gamma}^{\alpha,k}:\delta\boldsymbol{\sigma}_{\gamma}^{\alpha}\right)=\sum_{A=1}^{N_D}\left(\mathbf{S}_{\eta A}^{\alpha}:\delta\hat{\mathbf{u}}_{A}^{M\alpha}\right)-\mathbf{V}_{\eta}^{\alpha,k} \tag{3.28}$$

where,

$$\mathbf{Q}_{\eta\gamma}^{\alpha,k}=\delta_{\eta\gamma}^{K}\,\mathbf{I}-\theta\ \Delta t\ \mathbf{P}_{\eta\gamma}^{\alpha}:\mathbf{C}_{\gamma}^{\alpha,k}-(\theta\ \Delta t)^{2}\ \mathbf{P}_{\eta\gamma}^{\alpha}:\mathbf{G}_{\gamma}^{\alpha,k}:\left(\mathbf{I}-\theta\ \Delta t\ \mathbf{G}_{\gamma}^{\alpha,k}\right)^{-1}:\mathbf{C}_{\gamma}^{\alpha,k} \tag{3.29}$$

$$\mathbf{V}_{\eta}^{\alpha,k}=\mathbf{R}_{\eta}^{\alpha,k}+\theta\ \Delta t\ \sum_{\gamma=1}^{NP_{\alpha}}\left[\mathbf{P}_{\eta\gamma}^{\alpha}:\mathbf{G}_{\gamma}^{\alpha,k}:\left(\mathbf{I}-\theta\ \Delta t\ \mathbf{G}_{\gamma}^{\alpha,k}\right)^{-1}:\boldsymbol{\lambda}_{\gamma}^{\alpha,k}\right] \tag{3.30}$$

Considering $\eta=1,2,...,NP_{\alpha}$ in Eq. (3.28) separately, the stress increment vector at the enrichment domain Ω_{α} which contains stress increment within each part of the enrichment domain is obtained as:

$$\delta\boldsymbol{\sigma}^{\alpha}=\left(\mathbf{Q}^{\alpha,k}\right)^{-1}\ \mathbf{S}^{\alpha}\ \delta\hat{\mathbf{u}}^{M\alpha}-\left(\mathbf{Q}^{\alpha,k}\right)^{-1}\ \mathbf{V}^{\alpha,k} \tag{3.31}$$

where $\mathbf{Q}^{\alpha,k}$ and $\mathbf{S}^{\alpha}$ are coefficient tensors defined as:

$$\mathbf{Q}^{\alpha,k}=\left[\mathbf{Q}_{\eta\gamma}^{\alpha,k}\right]_{\eta,\gamma\in[1,NP_{\alpha}]};\qquad\mathbf{S}^{\alpha}=\left[\mathbf{S}_{\eta A}^{\alpha}\right]_{\eta\in[1,NP_{\alpha}],A\in[1,N_D]} \tag{3.32}$$

and

$$\delta\boldsymbol{\sigma}^{\alpha}=\left\{\left(\delta\boldsymbol{\sigma}_{1}^{\alpha,k+1}\right)^{T},\left(\delta\boldsymbol{\sigma}_{2}^{\alpha,k+1}\right)^{T},...,\left(\delta\boldsymbol{\sigma}_{NP_{\alpha}}^{\alpha,k+1}\right)^{T}\right\}^{T} \tag{3.33a}$$

$$\delta\hat{\mathbf{u}}^{M\alpha}=\left\{\left(\delta\hat{\mathbf{u}}_{1}^{M\alpha,k+1}\right)^{T},\left(\delta\hat{\mathbf{u}}_{2}^{M\alpha,k+1}\right)^{T},...,\left(\delta\hat{\mathbf{u}}_{N_D}^{M\alpha,k+1}\right)^{T}\right\}^{T} \tag{3.33b}$$

$$\mathbf{V}^{\alpha,k}=\left\{\left(\mathbf{V}_{1}^{\alpha,k}\right)^{T},\left(\mathbf{V}_{2}^{\alpha,k}\right)^{T},...,\left(\mathbf{V}_{NP_{\alpha}}^{\alpha,k}\right)^{T}\right\}^{T} \tag{3.33c}$$

3.3.2 Numerical evaluation of the macroscale problem

For the substrate region Ω_s, the finite element discretization of the macroscale equations is standard [24] and only briefly described when necessary. This subsection particularly focuses on the treatment of the macroscale problem in the enrichment region. The macroscale weak form is linearized to construct a Newton-Raphson iterative scheme, employing the linearized reduced order microscale problem stated in the previous section.

Considering the decomposition of the problem domain, the residual of the macroscale weak form is defined as:

$$\boldsymbol{\Psi}^M \equiv \sum_{\alpha=1}^{n_{\text{en}}} \tilde{\boldsymbol{\Psi}}_\alpha^M + \tilde{\boldsymbol{\Psi}}_s^M - \sum_{\alpha=1}^{n_{\text{en}}} \tilde{\boldsymbol{\Psi}}_\alpha^{MT} - \tilde{\boldsymbol{\Psi}}_s^{MT} = 0 \tag{3.34}$$

where,

$$\tilde{\boldsymbol{\Psi}}_\alpha^M = \int_{\Omega_\alpha} \nabla \mathbf{w}^M : \boldsymbol{\sigma}(\hat{\mathbf{u}}^M, \hat{\mathbf{u}}_\alpha^m)\, d\Omega; \quad \tilde{\boldsymbol{\Psi}}_s^M = \int_{\Omega_s} \nabla \mathbf{w}^M : \boldsymbol{\sigma}(\hat{\mathbf{u}}^M)\, d\Omega \tag{3.35}$$

$$\tilde{\boldsymbol{\Psi}}_\alpha^{MT} = \int_{\Gamma_\alpha^t} \mathbf{w}^M \cdot \tilde{\mathbf{t}}\, d\Gamma; \quad \tilde{\boldsymbol{\Psi}}_s^{MT} = \int_{\Gamma_s^t} \mathbf{w}^M \cdot \tilde{\mathbf{t}}\, d\Gamma \tag{3.36}$$

Γ_α^t is the part of the enrichment domain boundary that intersects with the Neumann boundary of the problem domain ($\Gamma_\alpha^t \equiv \Gamma_\alpha \cap \Gamma^t$); and, Γ_s^t is the part of the substrate region boundary that intersects with the Neumann boundary of the problem domain ($\Gamma_s^t \equiv \Gamma_s \cap \Gamma^t$). Within the substrate region, Ω_s, the microstructural displacement remains unresolved. The stress field therefore is a function of the macroscale displacement field only.

Substituting Eq. (3.11) into Eq. (3.34), the residual of the macroscale weak form within the enrichment domain, Ω_α, is expressed as:

$$\tilde{\boldsymbol{\Psi}}_\alpha^M = \sum_{\gamma=1}^{NP_\alpha} \int_{\Omega_\gamma^\alpha} \nabla \mathbf{w}^M\, d\Omega : \boldsymbol{\sigma}_\gamma^\alpha(t) \tag{3.37}$$

Employing the expression of $\tilde{\boldsymbol{\Psi}}_\alpha^M$ in Eq. (3.37) and considering the first order Taylor series ap-

proximation, the residual of the macroscale weak form (i.e., Eq. (3.34)) becomes:

$$\boldsymbol{\Psi}^{M,k+1} \approx \sum_{\alpha=1}^{n_{\text{en}}} \left(\tilde{\boldsymbol{\Psi}}_{\alpha}^{M,k+1} \right) + \tilde{\boldsymbol{\Psi}}_{s}^{M,k+1} = 0 \tag{3.38}$$

where,

$$\tilde{\boldsymbol{\Psi}}_{\alpha}^{M,k+1} \equiv \tilde{\boldsymbol{\Psi}}_{\alpha}^{M,k} - \tilde{\boldsymbol{\Psi}}_{\alpha}^{MT} + \delta\tilde{\boldsymbol{\Psi}}_{\alpha}^{M}; \quad \tilde{\boldsymbol{\Psi}}_{s}^{M,k+1} \equiv \tilde{\boldsymbol{\Psi}}_{s}^{M,k} - \tilde{\boldsymbol{\Psi}}_{s}^{MT} + \delta\tilde{\boldsymbol{\Psi}}_{s}^{M} \tag{3.39}$$

and

$$\delta\tilde{\boldsymbol{\Psi}}_{\alpha}^{M} = \sum_{\gamma=1}^{NP_{\alpha}} \left(\int_{\Omega_{\gamma}^{\alpha}} \nabla \mathbf{w}^{M} \, d\Omega \right) : \delta\boldsymbol{\sigma}_{\gamma}^{\alpha}; \quad \delta\tilde{\boldsymbol{\Psi}}_{s}^{M} = \int_{\Omega_s} \nabla \mathbf{w}^{M} : \delta\boldsymbol{\sigma}(\delta\hat{\mathbf{u}}^{M}) \, d\Omega \tag{3.40}$$

$\tilde{\boldsymbol{\Psi}}_{\alpha}^{MT}$ and $\tilde{\boldsymbol{\Psi}}_{s}^{MT}$ denote the prescribed boundary traction terms which do not vary with iterations at a given time step.

Using the standard finite element discretization detailed in Eq. (2.50) for the macroscale test function $\mathbf{w}^{M}$, $\delta\tilde{\boldsymbol{\Psi}}_{\alpha}^{M}$ (Eq. (3.40)) yields:

$$\delta\tilde{\boldsymbol{\Psi}}_{\alpha}^{M} = \sum_{\gamma=1}^{NP_{\alpha}} \left[\sum_{A=1}^{N_D} \left(\int_{\Omega_{\gamma}^{\alpha}} \nabla N_A \, d\Omega \, \hat{\mathbf{w}}_{A}^{M} \right) : \delta\boldsymbol{\sigma}_{\gamma}^{\alpha} \right] \tag{3.41}$$

Considering the stress increment (i.e., $\delta\boldsymbol{\sigma}^{\alpha}$) defined in Eq. (3.33a), the matrix form of Eq. (3.41) is presented as:

$$\delta\tilde{\boldsymbol{\Psi}}_{\alpha}^{M} = \left(\mathbf{B}^{\alpha}\right)^{\mathrm{T}} \, \delta\boldsymbol{\sigma}^{\alpha} \tag{3.42}$$

where,

$$\mathbf{B}^{\alpha} = \left[\mathbf{B}_{\gamma A}^{\alpha} \right]_{\gamma \in [1, NP_{\alpha}], A \in [1, N_D]}; \qquad \mathbf{B}_{\gamma A}^{\alpha} = \int_{\Omega_{\gamma}^{\alpha}} \nabla N_A \, d\Omega \, \hat{\mathbf{w}}_{A}^{M} \tag{3.43}$$

Substituting the stress coefficient increment (i.e. Eq. (3.31)) and Eq. (3.42) into Eq. (3.39), the weak form residual of the enrichment domain at the current iteration is presented in the vector-matrix form as:

$$\tilde{\boldsymbol{\Psi}}_{\alpha}^{M,k+1} = \mathbf{K}^{\alpha} \, \delta\hat{\mathbf{u}}^{M\alpha} - \delta\mathbf{f}^{\alpha} \tag{3.44}$$

where,

$$\mathbf{K}^{\alpha} = \left(\mathbf{B}^{\alpha}\right)^{\mathrm{T}} \left(\mathbf{Q}^{\alpha,k}\right)^{-1} \mathbf{S}^{\alpha} \tag{3.45}$$

$$\delta\mathbf{f}^{\alpha} = \left(\mathbf{B}^{\alpha}\right)^{\mathrm{T}} \left(\mathbf{Q}^{\alpha,k}\right)^{-1} \mathbf{V}^{\alpha,k} - \tilde{\mathbf{\Psi}}_{\alpha}^{M,k} + \tilde{\mathbf{\Psi}}_{\alpha}^{MT} \tag{3.46}$$

The detailed formulation and the standard finite element discretization of $\tilde{\mathbf{\Psi}}_{s}^{M,k+1}$ is presented in [24] and not repeated in the current chapter for brevity.

Assembling the macroscale element stiffness matrices and force increment vectors, the discrete macroscale weak form (i.e., Eq. (3.38)) at the $(k+1)^{\text{th}}$ iteration of the current time step, ${}_{n+1}t$, is expressed as:

$$\mathbf{K}\ \delta\hat{\mathbf{u}}^{M} = \delta\mathbf{f} \tag{3.47}$$

where,

$$\mathbf{K} = \mathop{\mathbf{A}}_{e} \mathbf{K}^{e} \tag{3.48}$$

$$\delta\hat{\mathbf{u}}^{M} = \left\{ \left(\delta\hat{\mathbf{u}}_{1}^{M,k+1}\right)^{T}, \left(\delta\hat{\mathbf{u}}_{2}^{M,k+1}\right)^{T}, ..., \left(\delta\hat{\mathbf{u}}_{N_D}^{M,k+1}\right)^{T} \right\}^{T} \tag{3.49}$$

$$\delta\mathbf{f} = \mathop{\mathbf{A}}_{e} \delta\mathbf{f}^{e} \tag{3.50}$$

$\mathbf{A}$ denotes the standard finite element assembly operator and e is the dummy index for all the macroscale finite elements in the problem domain. The linearized system of equations is evaluated incrementally using the implementation algorithm described in the next subsection.

3.3.3 Implementation algorithm

The reduced order variational multiscale enrichment (ROVME) method is implemented using the commercial software package, Diffpack [68]. Diffpack provides a library of C++ classes to facilitate the development of solution algorithms for complex PDEs. The overall solution strategy is summarized in Fig. 3.1, in which the enrichment domain superscript (α) and part subscript (γ) are omitted for clarity. In the preprocessing phase prior to the macroscale simulation, $\mathbf{S}_{\eta A}^{\alpha}$, $\mathbf{P}_{\eta\gamma}^{\alpha}$, $\mathbf{S}^{\alpha}$ and $\mathbf{B}^{\alpha}$ for each enrichment domain Ω_{α} are computed using Eqs. (3.18), (3.19), (3.32) (3.43) and

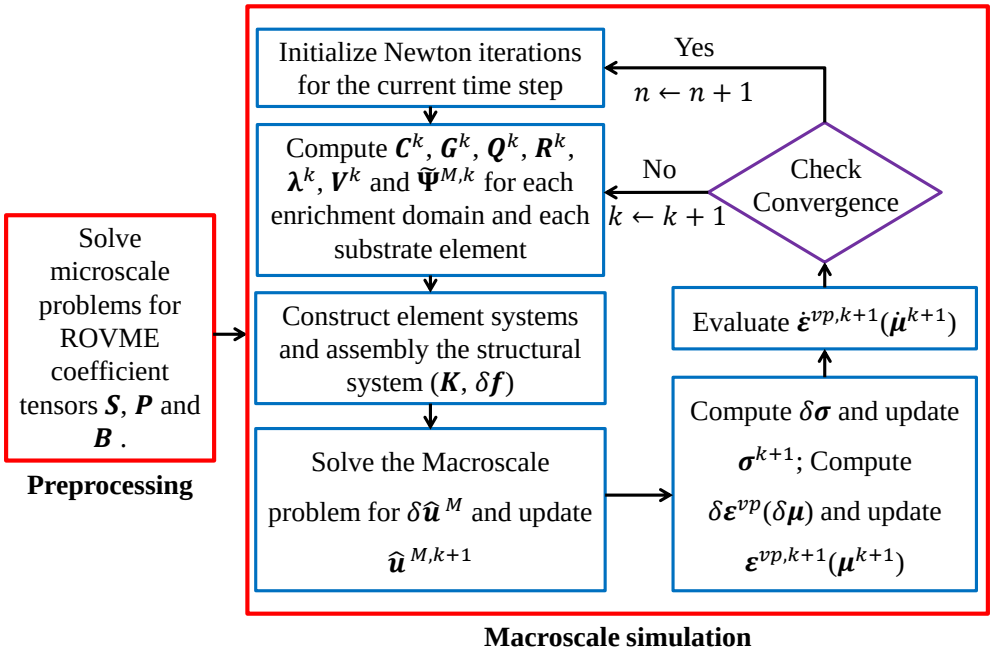

Figure 3.1: Reduced order model implementation strategy.

stored ($A = 1,2,...,N_D; \gamma = 1,2,...,NP_\alpha$ and $\eta = 1,2,...,NP_\alpha$). They remain constant throughout the macroscale simulation. At an arbitrary time ${}_nt$, the system is in equilibrium with the constitutive relations satisfied for the problem domain. The algorithm seeks to find the equilibrium state at ${}_{n+1}t$ as follows:

Given: ${}_n\hat{\mathbf{u}}^M, {}_n\boldsymbol{\sigma}, {}_n\varepsilon^{vp}$ and ${}_n\dot{\varepsilon}^{vp}$ (${}_n\boldsymbol{\mu}_\gamma^\alpha$ and ${}_n\dot{\boldsymbol{\mu}}_\gamma^\alpha$ for enrichment domains) at time ${}_nt$.

Find: $\hat{\mathbf{u}}^M, \boldsymbol{\sigma}, \varepsilon^{vp}$ and $\dot{\varepsilon}^{vp}$ ($\boldsymbol{\mu}_\gamma^\alpha$ and $\dot{\boldsymbol{\mu}}_\gamma^\alpha$ for enrichment domains) at time ${}_{n+1}t$.

1. Initialize Newton iterations by setting: k=0, $\hat{\mathbf{u}}^{M,0} = {}_n\hat{\mathbf{u}}^M$, $\boldsymbol{\sigma}^0 = {}_n\boldsymbol{\sigma}$, $\varepsilon^{vp,0} = {}_n\varepsilon^{vp}$, and $\dot{\varepsilon}^{vp,0} = {}_n\dot{\varepsilon}^{vp}$ ($\boldsymbol{\mu}_\gamma^{\alpha,0} = {}_n\boldsymbol{\mu}_\gamma^\alpha$, and $\dot{\boldsymbol{\mu}}_\gamma^{\alpha,0} = {}_n\dot{\boldsymbol{\mu}}_\gamma^\alpha$ for enrichment domains).

2. While not converged, loop over all the macroscale elements within the problem domain Ω for the current iteration $(k+1)$:

   (1) If the macroscale element is enriched:

   a) Compute $\mathbf{C}_\gamma^{\alpha,k}, \mathbf{G}_\gamma^{\alpha,k}, \mathbf{Q}_{\eta\gamma}^{\alpha,k}, \mathbf{R}_\eta^{\alpha,k}, \boldsymbol{\lambda}_\eta^{\alpha,k}, \mathbf{V}_\eta^{\alpha,k}, \tilde{\boldsymbol{\Psi}}_\alpha^{M,k}$ from Eqs. (3.25), (3.29), (3.23), (3.26), (3.30) and (3.37).

b) Construct $\mathbf{Q}^{\alpha,k}$ and $\mathbf{V}^{\alpha,k}$ from Eqs. (3.32) and (3.33c); and $\mathbf{K}^{\alpha}$ and $\delta\mathbf{f}^{\alpha}$ from Eqs. (3.45) and (3.46).

(2) If the macroscale element is not enriched :

a) Compute $\mathbf{K}^{e}$ and $\delta\mathbf{f}^{e}$ using the standard finite element procedure [24].

(3) Employing Eqs. (3.48) and (3.50), construct the stiffness matrix $\mathbf{K}$ and incremental force vector $\delta\mathbf{f}$ for the macroscale problem.

(4) Solve the macroscale problem (Eq. (3.47)) for $\delta\hat{\mathbf{u}}^{M}$ and update the macroscale displacement field with $\hat{\mathbf{u}}^{M,k+1} = \hat{\mathbf{u}}^{M,k} + \delta\hat{\mathbf{u}}^{M}$.

(5) If the macroscale element is enriched:

a) Compute the stress increment $\delta\boldsymbol{\sigma}^{\alpha}$ using Eq. (3.31) and update the stress field $\boldsymbol{\sigma}^{\alpha,k+1} = \boldsymbol{\sigma}^{\alpha,k} + \delta\boldsymbol{\sigma}^{\alpha}$.

b) Compute the inelastic strain coefficient increment $\delta\boldsymbol{\mu}_{\gamma}^{\alpha}$ using Eq. (3.27). Update the inelastic strain coefficient $\boldsymbol{\mu}_{\gamma}^{\alpha,k+1} = \boldsymbol{\mu}_{\gamma}^{\alpha,k} + \delta\boldsymbol{\mu}_{\gamma}^{\alpha}$.

c) Evaluate the inelastic strain rate coefficient $\dot{\boldsymbol{\mu}}_{\gamma}^{\alpha}$ through Eq. (3.22).

(6) If the macroscale element is not enriched:

a) Determine the stress increment $\delta\boldsymbol{\sigma}$. Update the stress field $\boldsymbol{\sigma}^{k+1} = \boldsymbol{\sigma}^{k} + \delta\boldsymbol{\sigma}$ [24].

b) Determine the inelastic strain increment $\delta\boldsymbol{\varepsilon}^{vp,k+1}$. Update the inelastic strain field $\boldsymbol{\varepsilon}^{vp,k+1} = \boldsymbol{\varepsilon}^{vp,k} + \delta\boldsymbol{\varepsilon}^{vp,k+1}$ [24].

c) Evaluate the inelastic strain rate $\dot{\boldsymbol{\varepsilon}}^{vp,k+1}$ from Eq. (2.5).

(7) Check for convergence:

$$\mathrm{e}^{M} = \frac{\|\hat{\mathbf{u}}^{M,k+1} - \hat{\mathbf{u}}^{M,k}\|_2}{\|\hat{\mathbf{u}}^{M,k+1} - {}_{n}\hat{\mathbf{u}}^{M}\|_2} \leq \text{Convergence tolerance} \tag{3.51}$$

(8) If convergence is not satisfied, set iteration counter $k \leftarrow k+1$ and proceed with the next iteration.

3. Repeat step 2 with $n \leftarrow n+1$ until the end of the observation period.

Table 3.1: Materials parameters for the numerical verification studies of ROVME.

Material type	E [GPa]	ν	A [MPa]	B [MPa]	ε_f	n	q	γ [MPa/hr]
Phase I	107	0.32	480	700	0.15	0.90	1.0	1.0
Phase II	87	0.32	360	100	0.17	0.96	1.0	1.0
Substrate	97	0.32	420	400	0.16	0.93	1.0	1.0

3.4 Numerical Verification

The reduced order VME (ROVME) method for elasto-viscoplastic problems is thoroughly verified using numerical simulations. The performance and accuracy characteristics of the ROVME approach are assessed by comparing the results with those of the direct VME simulations. The accuracy characteristics of the direct VME method compared with full resolution finite element analyses was previously demonstrated in Refs. [2, 23, 24].

In all simulations considered in this section, the domains are taken to consist of three separate materials. The heterogeneous material microstructure consists of two phases. A third material that approximates the properties of the composite domain is employed to idealize the behavior at the substrate. The material properties of the two elasto-viscoplastic phases and the corresponding substrate are summarized in Table 3.1 and the stress-strain curves of these materials under uniaxial tension are plotted in Fig. 3.2. The phase I material of the microstructure behaves similarly to high yield stress commercially pure titanium [71]. The phase II material is based on low yield stress commercially pure titanium [71]. The properties of the substrate material are obtained using the mixed theory. While the numerical examples provided below investigate two-phase microstructures, the proposed formulation is applicable to arbitrary number of phases and microstructural configurations. A number of multiscale approaches, such as computational homogenization [72, 73, 38, 74] and sequential multiscale modeling [75], also remain valid to compute the homogenized macroscale behavior in the presence of multiple phases within the microstructure. These approaches could be used to compute the substrate domain response.

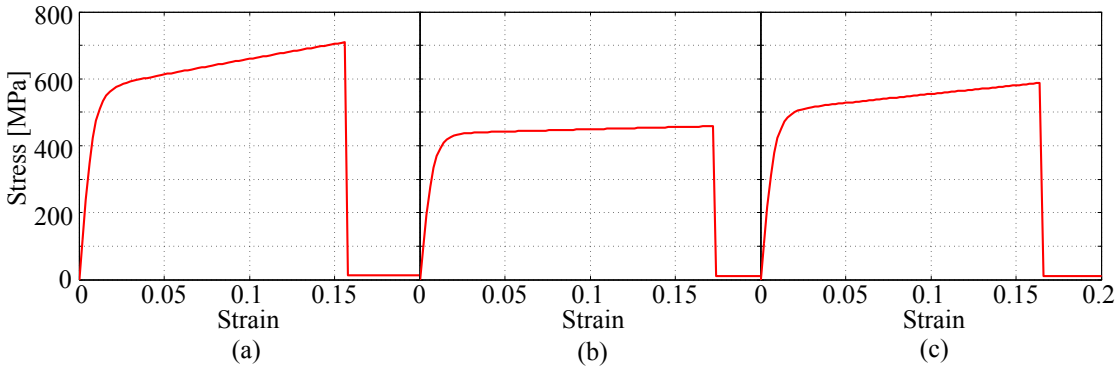

Figure 3.2: Stress-strain behavior of the constituent materials under uniaxial tension: (a) phase I; (b) phase II; and (c) substrate material.

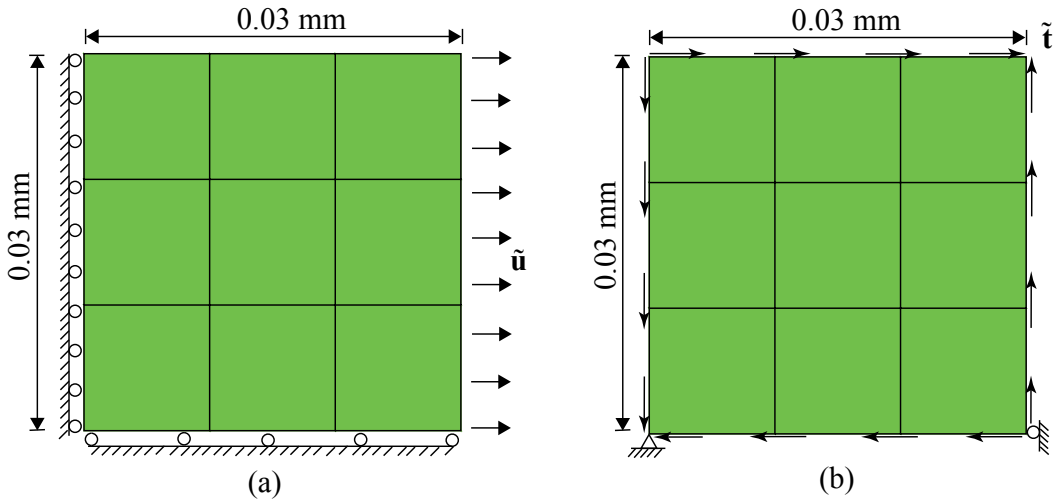

Figure 3.3: Numerical models of the square specimen: (a) macroscale discretization and sketch for uniform tensile load; and (b) macroscale discretization and sketch for pure shear load.

3.4.1 Square specimen with circular inclusions

A 2-D plane strain, 0.03 mm $\times$ 0.03 mm, square composite specimens are considered to assess the performance of the proposed reduced order VME method. The macroscale discretization and the loading conditions of the specimens are presented in Fig. 3.3. The macroscale discretization contains 16 nodes and 9 quadrilateral, bilinear finite elements. Each of the 9 macroscale elements is considered as an enrichment domain and associated with a microstructure containing a circular inclusion at the center, as shown in Fig. 3.4. The ratio between the size of the enrichment domain

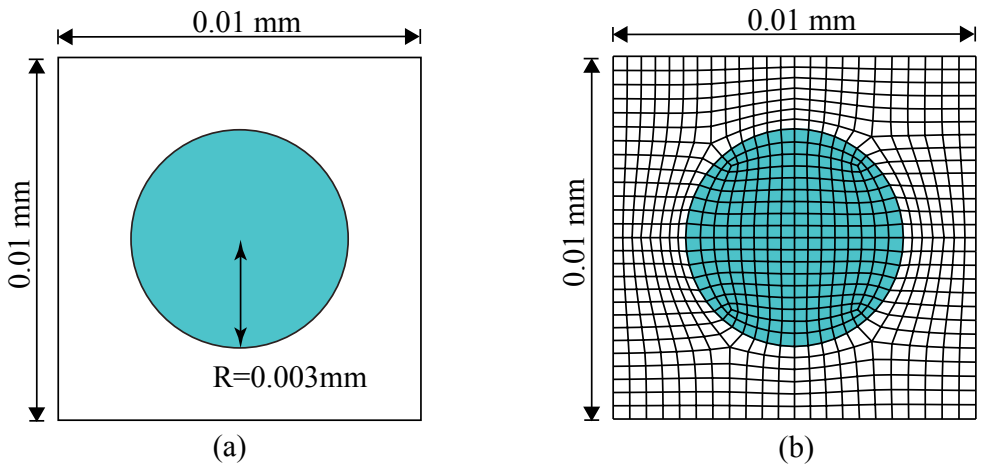

Figure 3.4: Microscale discretization of an enrichment domain with a circular inclusion: (a) reduced order VME method with 2 parts; and (b) direct VME method.

and the specimen domain is therefore 1/3. Phase I and phase II materials are identified as dark and light elements, respectively. The reduced order VME microscale partitioning consists of 2 parts and 6 degrees of freedom (DOFs). The direct VME microscale grid contains 837 nodes, 786 quadrilateral finite elements and 1674 DOFs. The behavior of the square composite domain is investigated under displacement controlled uniform tension and shear loading conditions. The loading is applied at the strain rate of approximately 3×10^{-4}/sec, until the specimen is about to fail (assessed based on ductility stated in Fig. 3.2). The time step size is determined such that further refinement does not change the results significantly. The time step size employed in the simulations is set to 0.36 second and the convergence tolerance is set to 1×10^{-3}.

Figure 3.5 compares the reaction force of the structure vs. the applied displacement as computed by the direct and reduced order VME models. The displacement in the tensile loading case refers to that prescribed at the boundary, whereas in the shear loading case is the displacement of the top right corner (in both vertical and horizontal directions each of which has the same magnitude and rate as stated above). At the end of the observation period of 432 seconds, the tensile specimen is under an applied deformation of 3.6×10^{-3} mm. The pure shear case has 3.3×10^{-3} mm applied displacement in both directions and the total simulation time is 396 seconds. The reaction force-displacement plots demonstrate that both models provide near identical behavior,

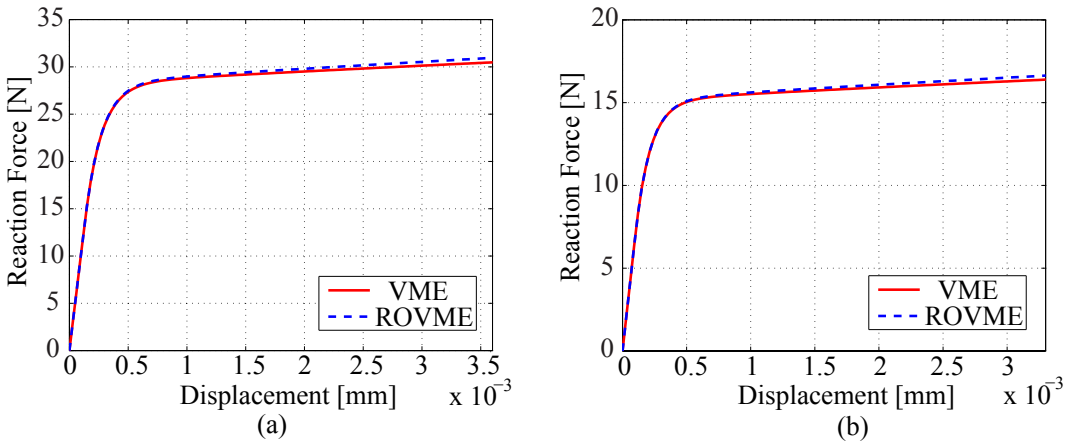

Figure 3.5: Overall reaction force-displacement comparison for the square specimen with circular inclusions between the direct VME simulation and the reduced order VME method: (a) under tension; and (b) under shear.

Table 3.2: Computational time comparison for square specimen with circular inclusions.

Loading case	Computational time		Computational time ratio	Microscopic DOFs ratio
	VME [hr]	ROVME [min]	VME/ROVME	VME/ROVME
Tension	12.50	11.11	67.53	279
Shear	10.70	11.44	56.08	279

in both elastic and plastic regimes. Figure 3.6 presents the contour plots of the equivalent stress of the central enrichment domain (the macroscale element at the center of the structure) for both methods, just before failure. The reduced order VME has only two parts in the microscale structure and the stress field is constant on each of the parts. On the other hand, the stress distribution smoothly transitions from stiffer inclusion to the matrix as computed by the direct VME method. The computational cost of the simulations are compared in Table 3.2 in terms of the total computational time. The computational time for the direct VME simulation is shown in hours [hr], whereas the time for ROVME simulation is presented in minutes [min]. The computational time comparison demonstrates that the reduced order VME approach is much more efficient compared with the direct VME method. We note that the improvement in terms of the computational time is less than the reduction of DOFs.

To further investigate the computational efficiency of the reduced order VME method, sim-

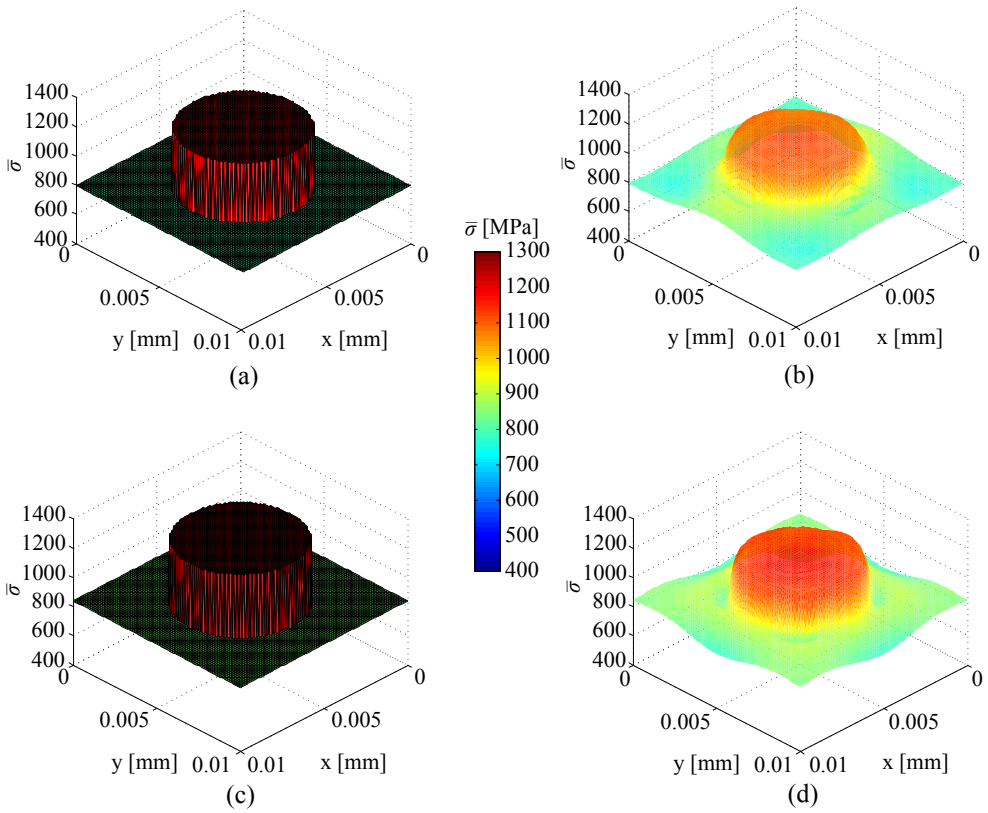

Figure 3.6: Equivalent stress of the central enrichment domain in the square specimen with circular inclusions: (a) reduced order VME under tension at 432 seconds; (b) direct VME under tension at 432 seconds; (c) reduced order VME under shear at 396 seconds; and (d) direct VME under shear at 396 seconds.

ulations with more parts in the ROVME microscale discretization are performed based on the macroscale model and loading condition shown in Fig. 3.3(a). In addition to the two-part model as shown in Fig. 3.4(a), a four-part and a seven-part model as presented in Fig. 3.7 are considered. The error over the entire enrichment region at an arbitrary time, t, is computed as:

$$e_\phi(t) = \frac{\sum_{\alpha=1}^{n_{\text{en}}} \left\| \phi^{\text{VME}}(\mathbf{x},t) - \phi^{\text{ROVME}}(\mathbf{x},t) \right\|_{2,\Omega_\alpha}}{\sum_{\alpha=1}^{n_{\text{en}}} \left\| \phi^{\text{VME}}(\mathbf{x},t) \right\|_{2,\Omega_\alpha}} \tag{3.52}$$

where, ϕ^{VME} and ϕ^{ROVME} denote a response field (e.g., equivalent stress) computed using the direct VME method and the reduced order VME method, respectively. $\|\cdot\|_{2,\Omega_\alpha}$ is the L_2 norm of the response field computed over Ω_α. Since all 9 macroscale elements are taken to be enriched

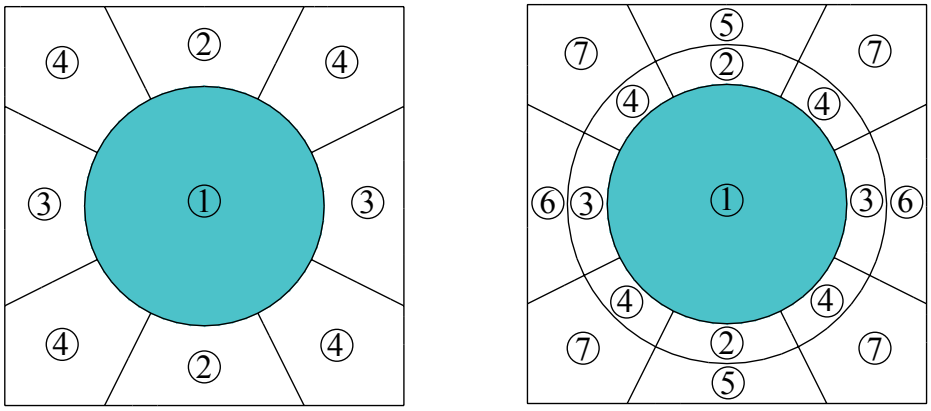

Figure 3.7: Microscale discretization of an enrichment domain with a circular inclusion: (a) reduced order VME method with 4 parts; and (b) reduced order VME method with 7 parts.

in the simulations, the enrichment region is the entire problem domain. For the ROVME method with different parts, the evolution of error in the equivalent stress over the enrichment region as a function of simulation time is compared in Fig. 3.8(a). The computational time per time step for each simulation is compared in Fig. 3.8(b). It is observed that the accuracy of the reduced order VME method improves using the model with more parts. But the rate of the accuracy improvement decreases when the number of parts is getting larger, indicating that low order models capture primary response features reasonably well. The computational time increases superlinearly (0.045 second per part from 2 parts to 4 parts and 0.08 second per part from 4 parts to 7 parts). We note that due to small problem size, a substantial time is spent for problem set-up (approximately 82% for the 2-part case).

To assess the accuracy of the reduced order VME method for phases with higher modulus contrasts in the enrichment domain, more numerical verifications are performed. The study is conducted under tensile loading (Fig. 3.3(a)) using the 2-part reduced order VME model (Fig. 3.4(a)). The elastic behavior of all constituents is assumed in the enrichment domain. Young's modulus contrasts for 9 cases considered are summarized in Table 3.3. The Poisson's ratio is 0.32 for all the materials. For each case, the error in equivalent stress over the entire enrichment region is computed using Eq. (3.52). These errors are plotted in Fig. 3.9(a) as a function of modulus con-

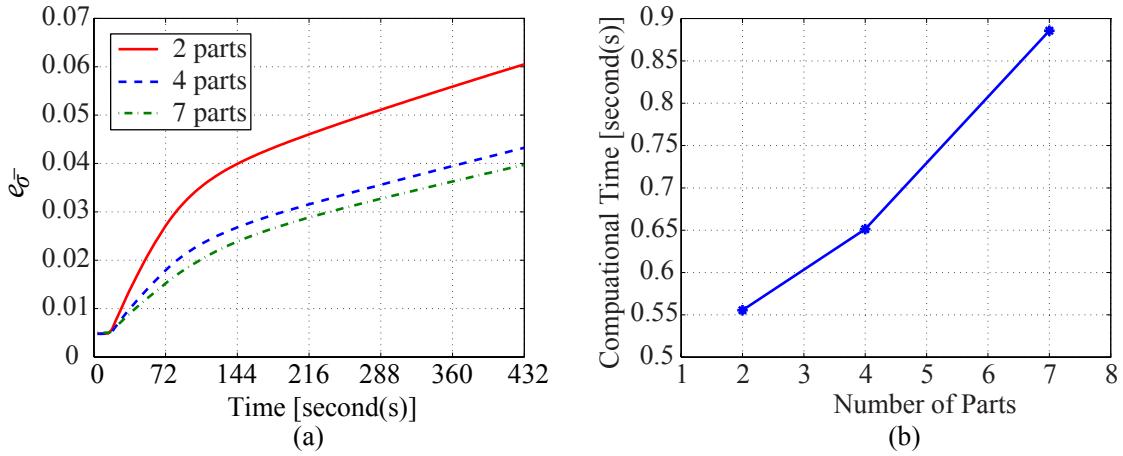

Figure 3.8: Results of reduced order VME method with different parts: (a) error in equivalent stress over the enrichment region as a function of simulation time; and (b) computational time per time step.

Table 3.3: Multiple Young's modulus contrasts of the two phases in the enrichment domain.

Case number	Young's modulus [GPa]		Young's modulus ratio
	Inclusion	Matrix	($E_{\text{inclusion}}/E_{\text{matrix}}$)
1	100	1	100
2	100	2	50
3	100	10	10
4	100	20	5
5	100	100	1
6	20	100	0.2
7	10	100	0.1
8	2	100	0.02
9	1	100	0.01

trast. The composite stiffness, $\bar{E}$, is obtained through the reaction force - displacement plot of each test ($\bar{E}$ = (reaction force / area) / (displacement/ structural length)). The errors in the composite stiffness are plotted in Fig. 3.9(b), with respect to the modulus contrast. When the modulus ratio is one, the reduced order VME method produces identical results as the direct VME method (error in both plots is zero), due to the fact that there is no material heterogeneity in the enrichment domain (material properties are the same everywhere). As the modulus contrast gets larger, the error in stress rises in a decreasing rate. The same pattern is observed for the error in the composite stiffness. For modulus ratio lower than unity, an increase in composite stiffness error followed by a

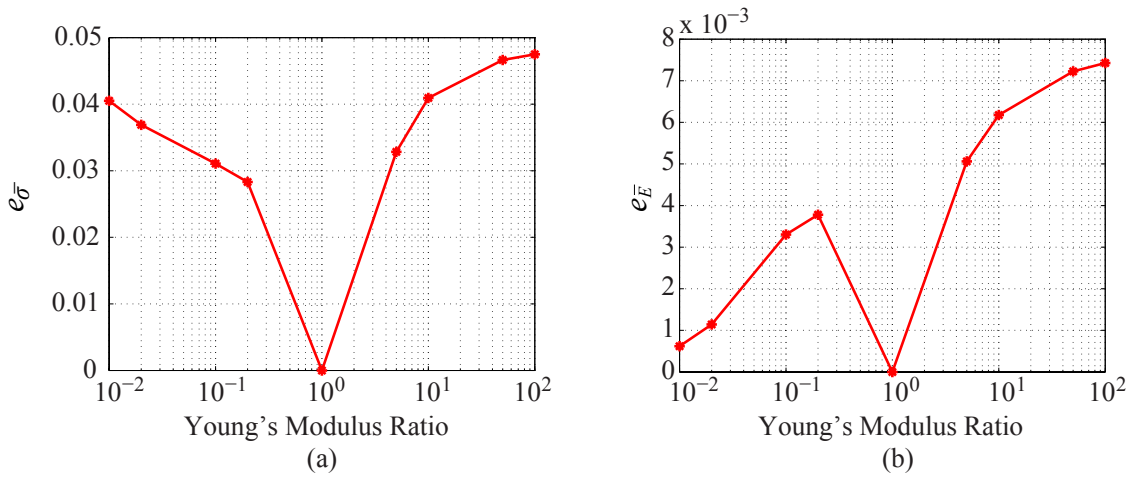

Figure 3.9: Modulus contrast analysis: (a) error in equivalent stress over enrichment region; and (b) error in the composite stiffness.

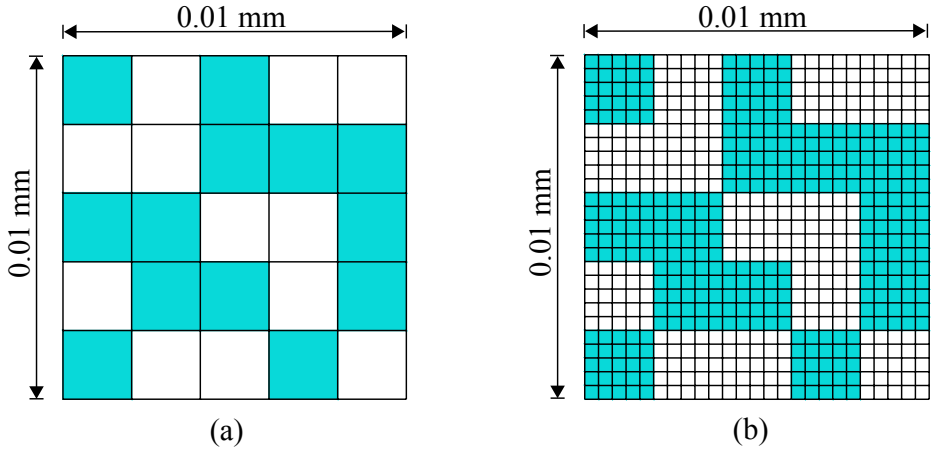

Figure 3.10: Microscale discretization of an enrichment domain with random grains: (a) reduced order VME method with 25 parts; and (b) direct VME method.

reduction as a function of modulus contrast is observed. When the inclusion modulus is small, the stiffness is dominated by the matrix properties only, which is well-captured by the reduced order VME approach.

3.4.2 Square specimen with random grains

A second set of numerical simulations is performed to study the accuracy of the proposed approach in capturing the local microstructural response characteristics. The microstructure contains 25 randomly placed square grains with two material phases, phase I (dark) and phase II (light), as

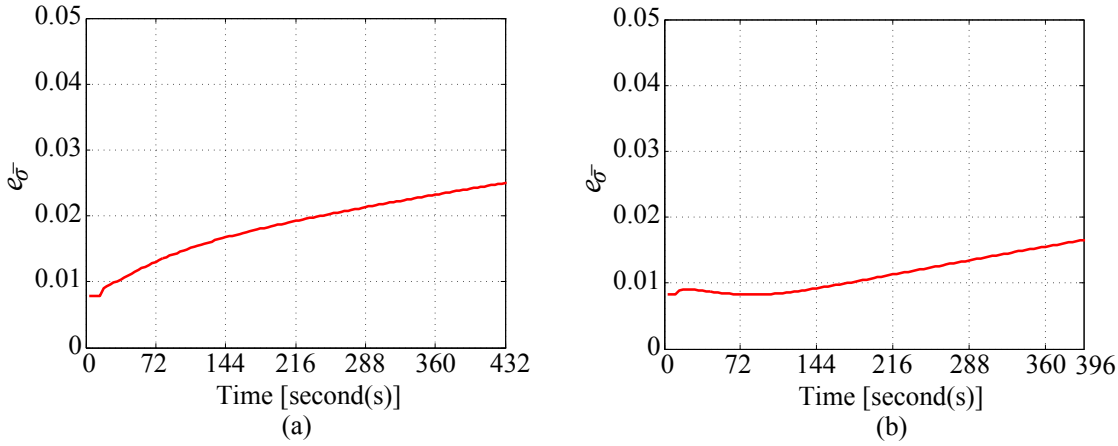

Figure 3.11: Error in equivalent stress over the enrichment region as a function of simulation time for the square specimen with random grains: (a) under tension; and (b) under shear.

illustrated in Fig. 3.10. In reduced order model partitioning, each grain is taken as a part. The direct VME method further discretizes each grain with 25 finite elements. The ROVME microscale partitioning has 25 parts and 75 DOFs whereas the direct VME microscale grid contains 625 quadrilateral finite elements with 676 nodes and 1352 DOFs. Identical macroscale discretization and loading conditions of the specimen as shown in Fig. 3.3 are used in the current example. The loading rate, time step size and observation periods for both loading cases are the same as those in Section 3.4.1.

Identical to the previous numerical examples, the enrichment region is the entire problem domain which includes all of the 9 macroscale elements. The evolution of error in the equivalent stress over the enrichment region as a function of simulation time is shown in Fig. 3.11 for both tensile and shear loading conditions. At an arbitrary time step, the error is evaluated using Eq. (3.52). It can be observed that the error in stress slightly accumulates along with the increase in plastic strain. The maximum error is at the end of the simulation where failure is set to initiate. The increase in error in time is consistent with the example in Section 3.4.1, due to the slightly larger hardening modulus predicted by the reduced order model. For the shear loading case, the error in stress slightly decreases shortly after entering the plastic regime due to the stress redistribution within the enrichment region which softens the rigid kinematics of the reduced order model. The

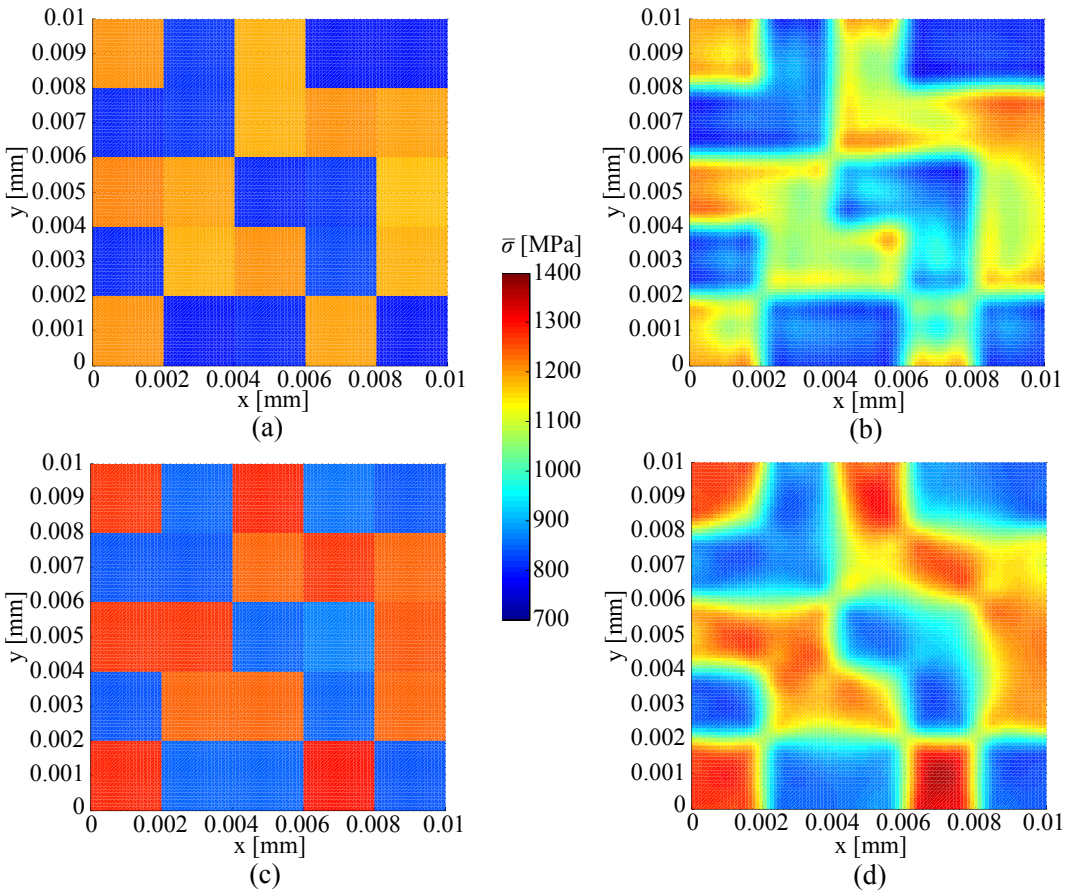

Figure 3.12: Equivalent stress contour of the central enrichment domain in the specimen with random grains: (a) reduced order VME under tension at 432 seconds; (b) direct VME under tension at 432 seconds; (c) reduced order VME under shear at 396 seconds; and (d) direct VME under shear at 396 seconds.

error starts to accumulate once the stress redistribution is completed. At the onset of failure initiation within the structure, the highest error in equivalent stress is 2.5% for the tensile loading and 1.7% for the shear loading, as shown in Fig. 3.11. The local equivalent stress contours for the central enrichment domain, corresponding to the prescribed peak load at the end of the simulations, are shown in Fig. 3.12. The stress contours demonstrate that the reduced order VME method captures the local stress variation within the microstructure reasonably well (0.8% - 2.5% error). The overall reaction force vs. prescribed displacement comparison is presented in Fig. 3.13. The figure shows that the global behavior of the reduced order VME method closely agrees with the direct VME method, in both elastic and plastic states. The comparisons of the global and local re-

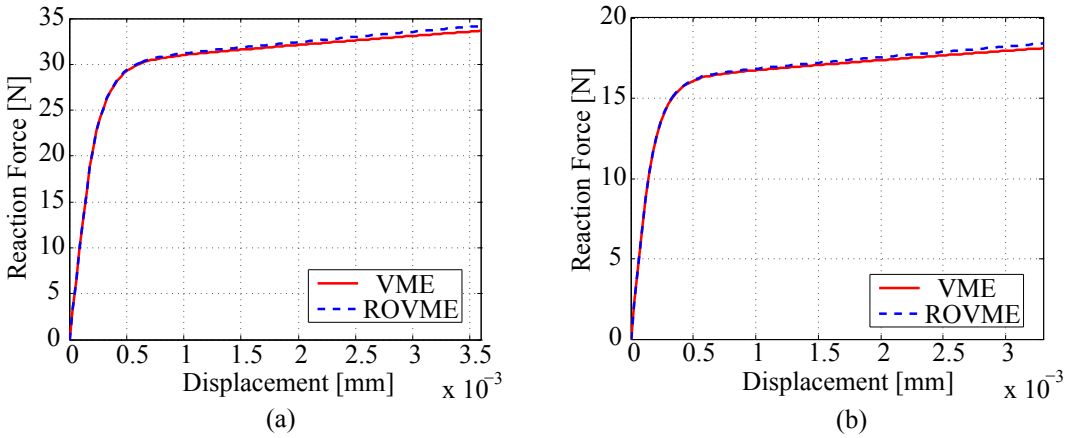

Figure 3.13: Overall reaction force-displacement comparison for the square specimen with particles between the direct VME simulation and the reduced order VME method: (a) under tension; and (b) under shear.

sponses verified the high accuracy of the reduced order VME method, even using relatively coarse microscale partitioning. The computational time of both simulations are listed and compared in Table 3.4. The reduced order VME reduces the computational effort of the direct VME method by at least the same reduction in DOFs, which points to very favorable computational cost of the proposed approach.

Table 3.4: Computational time comparison for square specimen with particles.

Loading case	Computational time		Computational time ratio	Microscopic DOFs ratio
	VME [hr]	ROVME [min]	VME/ROVME	VME/ROVME
Tensile	13.69	15.81	51.94	18.03
Shear	4.75	15.94	17.89	18.03

3.4.3 L-shaped specimen with random grains

The proposed ROVME method is further verified using the numerical analysis of an L-shaped specimen which contains both enrichment and substrate regions while subjected to more complex stress states. The geometry, loading condition and the macroscale discretization are illustrated in Fig. 3.14. The enrichment region (identified with dark shading) is placed within the area of

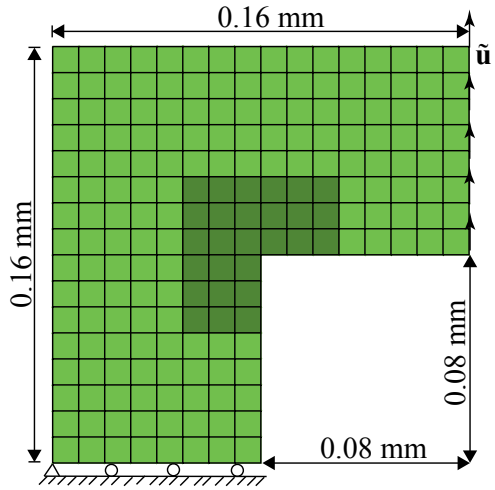

Figure 3.14: Macroscale discretization and sketch for L-shaped specimen.

stress concentration, around the inner corner of the specimen. The characteristic size scale ratio defined as the ratio between the size of the enrichment domain and the length scale associated with high stress gradients around the corner is approximately 1/6. The macroscale mesh consists of 192 quadrilateral elements, 27 of which are enriched. Within the enrichment domains of the enrichment region, the microstructural geometry for reduced order model partitioning and for the direct discretization are identical to those shown in Fig. 3.10. The material properties of the phases, as well as within the substrate region, are summarized in Table 3.1. The specimen is subjected to uniform displacement controlled loading in the vertical direction along the right edge of the specimen as shown in Fig. 3.14. The maximum amplitude of the loading is 0.0256 mm applied in 576 seconds, at a rate of 4.4×10^{-5} mm/sec, which corresponds to the onset of failure initiation within the specimen. Further loading would lead to failure within the structure. The simulation time step size is set to be 0.72 second and the convergence tolerance is taken to be 1×10^{-3} which is the same as employed in Sections 3.4.1 and 3.4.2 .

Figure 3.15 illustrates the evolution of error in equivalent stress within the enrichment region, which is plotted as a function of simulation time. The errors at each time step is computed using Eq. (3.52). The maximum error in the stress is less than 2.7% which further substantiates the accuracy characteristics of the proposed reduced order VME methodology. The error in stress

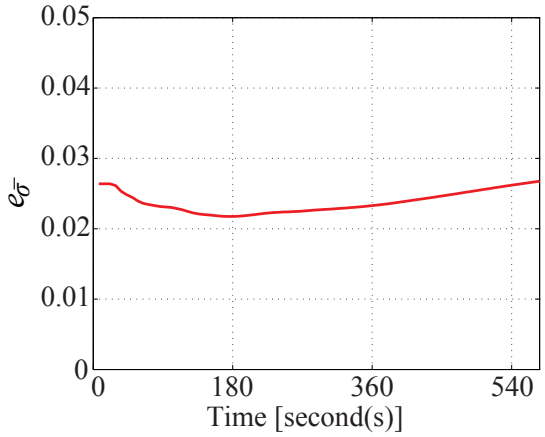

Figure 3.15: Error in equivalent stress as a function of time for the L-shaped specimen.

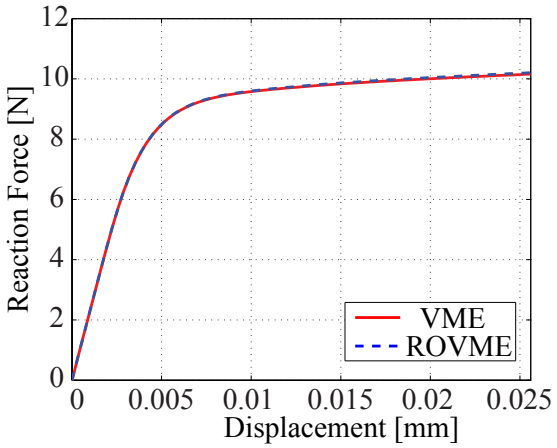

Figure 3.16: L-shaped specimen overall reaction force-displacement comparison between the direct VME simulation and the reduced order VME method.

slightly decreases after the onset of the plastic deformation, due to the stress redistribution over the enrichment region which softens the rigid kinematics of the reduced order model. The error increases thereafter and reaches the maximum value at the end of the simulation, similar to the previous example. Figure 3.16 presents the comparison of the overall force - displacement curves from the direct VME method and the reduced order VME simulation. The close agreement of the two model predictions demonstrates that the proposed reduced order approach accurately captures the global elasto-viscoplastic response of the structure. The equivalent stress contours at the end of the simulations are presented for both of the approaches in Fig. 3.17. For both approaches, the stress contours are obtained by combining the fine and coarse scale responses and reconstructing

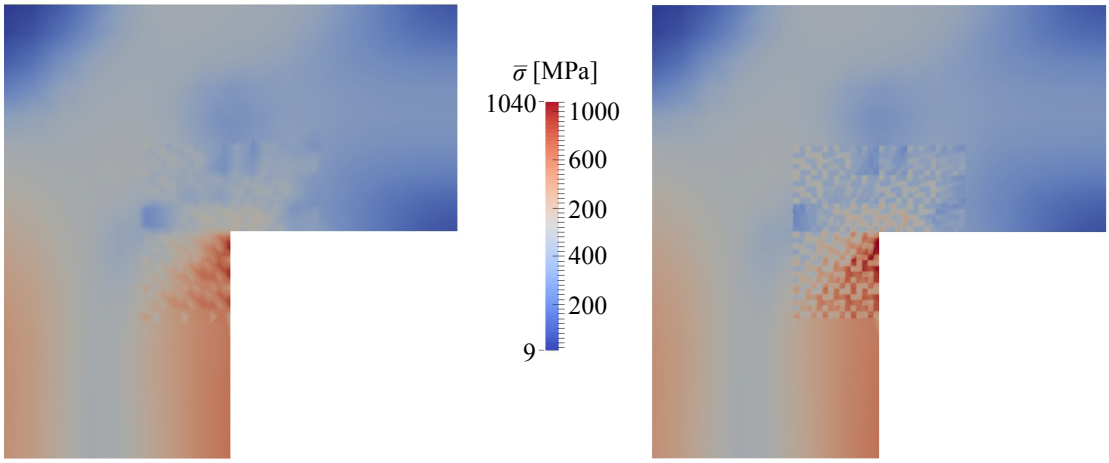

Figure 3.17: Equivalent stress contours of the L-shaped specimen with random grains at 576 seconds: (a) reduced order VME model; (b) direct VME model.

the total stress in the post-processing phase. Since the resolution of the reduced order VME method is much lower than the direct VME method, the stress contour of the reduced order VME method is slightly smoother than the direct VME method. The stress variation of the ROVME simulation within the domain closely approximates that predicted by the reference model. The computational cost of the simulations are presented in Table 3.5, which clearly shows the computational benefits of the reduced order VME methodology.

Table 3.5: Computational time comparison for L-shaped specimen.

Computational time		Computational time ratio	Microscopic DOFs ratio
VME [hr]	ROVME [min]	VME/ROVME	VME/ROVME
66.66	31.14	128.44	18.03

Chapter 4

REDUCED ORDER VARIATIONAL MULTISCALE ENRICHMENT METHOD FOR THERMO-MECHANICAL PROBLEMS

4.1 Introduction

High temperature environments induce thermal expansion and changes in material properties, which may be critical in the response prediction of structures subjected to extreme environments. The current chapter extends the ROVME method to address thermo-mechanical problems. The thermo-mechanical coupling effects due to the presence of thermal expansions, temperature-dependent mechanical inelastic properties, as well as the elastic properties are taken into account [71, 76, 77]. A key novel contribution of the present chapter is the efficient approximation of the temperature dependence of the reduced order model coefficients, which allows the thermo-mechanical ROVME to retain the computational efficiency. Numerical studies are performed to verify the proposed method against direct numerical simulations, and demonstrate its capability in capturing the thermo-mechanical behavior of heterogeneous structures.

The remainder of the chapter is organized as follows: Section 4.2 provides the problem statement and governing equations of the elasto-viscoplastic problem. Sections 4.3 and 4.4 describe the formulation of the VME and ROVME methods for thermo-mechanical problems, respectively. Sections 4.5 details the implementation strategy. Sections 4.6 and 4.7 present numerical simulations which demonstrate the accuracy and capability of the proposed methodology.

4.2 Governing Equations for Thermo-Mechanical Problems

Considering the temperature effect, the domain of the structure is denoted by $\Omega \subset \mathbb{R}^{n_{\text{sd}}}$ (n_{sd} is the number of spatial dimensions) as shown in Fig. 4.1, the equilibrium equation within the

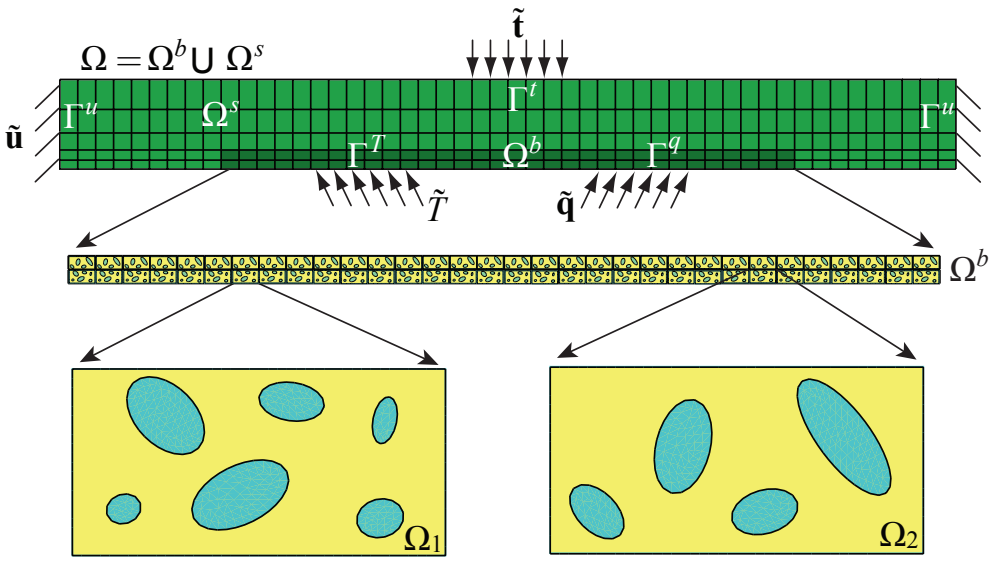

Figure 4.1: The schematic representation of the overall problem domain (Ω), enrichment region (Ω_b) and two representative enrichment domains (Ω_1 and Ω_2).

problem domain is expressed as:

$$\nabla \cdot \boldsymbol{\sigma}(\mathbf{x}, T, t) = 0; \quad \mathbf{x} \in \Omega,\ t \in [0,\ t_e] \tag{4.1}$$

where, $\mathbf{x}$ and t are the position and time coordinates, respectively; T the temperature; $\boldsymbol{\sigma}$ the stress tensor; $\nabla \cdot (\cdot)$ the divergence operator and t_e the end of the observation period. The body force is taken to be negligible compared with the external force. The constitutive behavior is expressed as:

$$\boldsymbol{\sigma}(\mathbf{x}, T, t) = \mathbf{L}(\mathbf{x}, T) : \left[\boldsymbol{\varepsilon}(\mathbf{x}, T, t) - \boldsymbol{\varepsilon}^{vp}(\mathbf{x}, T, t) - \boldsymbol{\varepsilon}^{T}(\mathbf{x}, T)\right] \tag{4.2}$$

in which, $\mathbf{L}$ is the temperature-dependent tensor of elastic moduli; $\boldsymbol{\varepsilon}^{vp}$ and $\boldsymbol{\varepsilon}^{T}$ denote the viscoplastic and thermal strains, respectively; and $(:)$ is the double inner product. The thermal strain is expressed as:

$$\boldsymbol{\varepsilon}^{T}(\mathbf{x}, T) = \boldsymbol{\alpha}^{T}(\mathbf{x})\left[T(\mathbf{x}) - T_0\right] \tag{4.3}$$

where, T_0 is the reference temperature; and $\boldsymbol{\alpha}^T$ the tensor of thermal expansion coefficients. The evolution of the inelastic strain is expressed in the functional form:

$$\dot{\boldsymbol{\varepsilon}}^{vp} = \Phi\left(\boldsymbol{\sigma}, \boldsymbol{\varepsilon}^{vp}, T, \mathbf{q}; \mathbf{k}\right) \tag{4.4}$$

in which, $\mathbf{q}$ denotes the vector of internal state variables that represent the internal deformation mechanisms characterizing the inelastic processes, and $\mathbf{k}$ is the set of material properties associated with the inelastic flow. The specific forms of the evaluation laws of the internal state variables are provided in Section 4.6 in the context of numerical examples. As further explained below, we are interested in the detailed response within a characteristic subdomain ($\Omega_b \subset \Omega$), where the material microstructure with multiple constituents is resolved. The overall constitutive model form (i.e., Eqs. (4.2)-(4.4)) is taken to be the same for all constituents, whereas the model parameters and evolution equations (i.e., $\mathbf{L}, \boldsymbol{\alpha}, \mathbf{k}, \mathbf{q}$ and Φ) could be different for each constituent. The boundary conditions of the mechanical problem are the same as stated in Chapter 2.

The thermal state of the structure is defined by the steady state conditions:

$$\nabla \cdot [\mathbf{K}(\mathbf{x}) \cdot \nabla T(\mathbf{x}, t)] = 0; \qquad \mathbf{x} \in \Omega \tag{4.5}$$

subjected to

$$T(\mathbf{x}, t) = \tilde{T}(\mathbf{x}, t); \qquad \mathbf{x} \in \Gamma^T \tag{4.6}$$

$$\mathbf{K} \cdot \nabla T = \tilde{\mathbf{q}}(\mathbf{x}, t); \qquad \mathbf{x} \in \Gamma^q \tag{4.7}$$

where, $\mathbf{K}$ is thermal conductivity tensor; $\tilde{T}$ and $\tilde{\mathbf{q}}$ denote boundary temperature and flux data along the respective boundaries. The time variation of temperature is due to time-dependent boundary conditions, which is taken to be independent of the mechanical response. The transients are taken to occur at time scales significantly shorter than the time scales at which mechanical loads are applied, and therefore neglected in this study.

4.3 VME for Thermo-Mechanical Problems

The VME formulation of the mechanical response of inelastically deforming solids are presented in the previous chapter. In what follows, the VME equations for the thermal problem are summarized.

Considering the additive decomposition of the displacement field and test function (Eqs. (2.15) and (2.17)), the governing equation in the weak form is decomposed into macroscale and microscale problems. The macroscale and microscale equilibrium weak forms are identical to Eqs. (3.1) and (3.2). Similar to the displacement decomposition of the mechanical problem (2.15), the temperature field is decomposed into macro- and microscale components:

$$T(\mathbf{x},t) = T^M(\mathbf{x},t) + \sum_{\alpha=1}^{n_{\text{en}}} \mathscr{H}(\Omega_\alpha)\; T^m_\alpha(\mathbf{x},t) \tag{4.8}$$

where, $T^M \in \mathscr{W}^M(\Omega)$ and $T^m_\alpha \in \mathscr{W}_\alpha(\Omega_\alpha)$ are the macroscale and microscale temperature fields, respectively. $\mathscr{W}^M$ and $\mathscr{W}_\alpha$ are the trial spaces for the macro- and microscale temperatures:

$$\mathscr{W}^M(\Omega) \equiv \left\{ T^M(\mathbf{x},t) \,\middle|\, T^M = \sum_{A=1}^{N_D} N_A(\mathbf{x})\; \hat{T}^M_A(T,t);\; \hat{T}^M_A = \tilde{T}(\mathbf{x}_A,t) \text{ if } \mathbf{x}_A \in \Gamma^T \right\} \tag{4.9}$$

$$\mathscr{W}_\alpha(\Omega_\alpha) \equiv \left\{ T^m_\alpha(\mathbf{x},t) \,\middle|\, T^m_\alpha = \sum_{a=1}^{n_{d\alpha}} n_{\alpha,a}(\mathbf{x})\; \hat{T}^m_{\alpha,a}(T,t);\; \hat{T}^m_{\alpha,a} = 0 \text{ if } \mathbf{x}_\alpha \in \Gamma^q_\alpha \right\} \tag{4.10}$$

Correspondingly, the steady state thermal problem (Eqs. (4.5)-(4.7)) yields a macroscale problem,

$$\int_\Omega \nabla v^M \cdot \mathbf{K} \cdot \nabla T^M \; d\Omega = \int_{\Gamma^q} v^M \cdot \tilde{\mathbf{q}} \; d\Gamma - \sum_{\alpha=1}^{n_{\text{en}}} \int_{\Omega_\alpha} \nabla v^M \cdot \mathbf{K} \cdot \nabla T^m_\alpha \; d\Omega \tag{4.11}$$

and a series of microscale problems,

$$\int_{\Omega_\alpha} \nabla v^m_\alpha \cdot \mathbf{K} \cdot \nabla T^m_\alpha \; d\Omega = -\int_{\Omega_\alpha} \nabla v^m_\alpha \cdot \mathbf{K} \cdot \nabla T^M \; d\Omega; \quad \alpha = 1,2,...n_{\text{en}}. \tag{4.12}$$

where, v^M and v^m_α are the macro- and microscale temperature test functions, respectively.

For both thermal and mechanical problems, the macroscale system and microscale problems are solved iteratively until convergence is achieved at a given time step. In the enrichment region, stress and strain fields are updated at each integration point of the microscale discretization. Therefore, the computational complexity of VME is proportional to the number of enrichment domains within the enrichment region as well as the complexity of the microstructural morphology within the enrichment domains.

4.4 ROVME for Thermo-Mechanical Problems

ROVME was recently introduced to improve the computational efficiency of the VME approach [39]. In this chapter, ROVME is generalized to address thermo-mechanical problems. Starting from the mechanical problem under temperature effect, we consider the following decomposition of the microscale displacement field:

$$\mathbf{u}_\alpha^m(\mathbf{x},T,t) = \sum_{A=1}^{N_D} \mathbf{H}_A^\alpha(\mathbf{x},T)\cdot\hat{\mathbf{u}}_A^{M\alpha}(T,t) + \int_{\Omega_\alpha} \mathbf{h}^\alpha(\mathbf{x},\hat{\mathbf{x}},T) : \boldsymbol{\varepsilon}^{vp}(\hat{\mathbf{x}},T,t)\, d\hat{\mathbf{x}} + \mathbf{G}^\alpha(\mathbf{x},T)\,(T-T_0) \tag{4.13}$$

where, $\hat{\mathbf{u}}_A^{M\alpha}$ denotes the macroscale nodal coefficient of the enrichment domain, Ω_α; $\mathbf{H}_A^\alpha$, a second order tensor, is the influence function associated with the linear elastic component of the response field in Ω_α; $\mathbf{h}^\alpha$, a third order tensor, is the influence function for the inelastic deformation within the microstructure; and $\mathbf{G}^\alpha$, a first order tensor, is the influence function associated with the thermal expansion in the enrichment domain. The governing equations for the influence functions $\mathbf{H}_A^\alpha$, $\mathbf{h}^\alpha$ and $\mathbf{G}^\alpha$ are obtained from the microscale problem, Eq. (3.2). Substituting the constitutive equation, Eq. (4.2), and the microscale displacement field discretization, Eq. (4.13), into Eq. (3.2) yields

$(\alpha = 1,2,...n_{\text{en}})$:

$$\sum_{A=1}^{N_D} \int_{\Omega_\alpha} \nabla \mathbf{w}_\alpha^m : \mathbf{L}(T) : \left[\nabla \mathbf{H}_A^\alpha(T) + \nabla N_A\right] \, d\Omega \cdot \hat{\mathbf{u}}_A^{M\alpha}(T,t) + \int_{\Omega_\alpha} \nabla \mathbf{w}_\alpha^m : \mathbf{L}(T) : \left[\int_{\Omega_\alpha} \nabla \mathbf{h}^\alpha(\mathbf{x},\hat{\mathbf{x}},T) : \boldsymbol{\varepsilon}^{vp}(\hat{\mathbf{x}},T,t) \, d\hat{\mathbf{x}} - \boldsymbol{\varepsilon}^{vp}(\mathbf{x},T,t)\right] \, d\Omega + \int_{\Omega_\alpha} \nabla \mathbf{w}_\alpha^m : \mathbf{L}(T) \cdot \left[\mathbf{G}^\alpha(T)\,(T - T_0) - \boldsymbol{\alpha}^T\,(T - T_0)\right] \, d\Omega = 0 \quad (4.14)$$

We assume that each enrichment domain is sufficiently small compared to the macroscale structure and that the thermal gradient across an enrichment domain is negligible. A first order approximation is that the thermal state within the enrichment domain is spatially uniform, with enrichment domain temperature approximated as:

$$T^\alpha(t) = \frac{1}{|\Omega_\alpha|} \int_{\Omega_\alpha} T(\mathbf{x},t) \, d\Omega \quad (4.15)$$

Considering the elastic state of the enrichment domain at uniform reference temperature, T^α, and in the absence of inelastic processes, Eq. (4.14) reduces to:

$$\int_{\Omega_\alpha} \nabla \mathbf{w}_\alpha^m : \mathbf{L}(T^\alpha) : \nabla \mathbf{H}_A^\alpha(T^\alpha) \, d\Omega = -\int_{\Omega_\alpha} \nabla \mathbf{w}_\alpha^m : \mathbf{L}(T^\alpha) \cdot \nabla N_A \, d\Omega; \quad A = 1,2,...,N_D \quad (4.16)$$

Equation (4.16) is the elastic influence function problem, which is evaluated for $\mathbf{H}_A^\alpha(T^\alpha)$. Homogeneous Dirichlet boundary conditions are imposed to ensure that the microscale displacements vanish along $\partial\Omega_\alpha$. In the presence of inelastic deformation but at uniform reference temperature within the enrichment domain, the inelastic influence function problem in weak form is obtained:

$$\int_{\Omega_\alpha} \nabla \mathbf{w}_\alpha^m : \mathbf{L}(T^\alpha) : \nabla \mathbf{h}^\alpha(\mathbf{x},\hat{\mathbf{x}},T^\alpha) \, d\Omega = \int_{\Omega_\alpha} \nabla \mathbf{w}_\alpha^m : \mathbf{L}(T^\alpha) \, \delta^d(\mathbf{x} - \hat{\mathbf{x}}) \, d\Omega; \quad \forall \hat{\mathbf{x}} \in \Omega_\alpha \quad (4.17)$$

where, δ^d denotes the Dirac delta distribution. In the presence of thermal deformation and in view

of Eqs. (4.16) and (4.17), Eq. (4.14) yields the thermal influence function problem:

$$\int_{\Omega_\alpha} \nabla \mathbf{w}_\alpha^m : \mathbf{L}(T^\alpha) \cdot \mathbf{G}^\alpha(T^\alpha)\, d\Omega = \int_{\Omega_\alpha} \nabla \mathbf{w}_\alpha^m : \mathbf{L}(T^\alpha) \cdot \boldsymbol{\alpha}^T\, d\Omega \tag{4.18}$$

The influence functions, $\mathbf{H}_A^\alpha$, $\mathbf{h}^\alpha$ and $\mathbf{G}^\alpha$, are temperature-dependent because the elastic properties of the constituents vary as a function of temperature (i.e., $\mathbf{L}(T^\alpha)$). For a fixed uniform temperature field, T^α, discrete approximations to the influence functions are evaluated numerically [21, 22, 37, 78].

4.4.1 Reduced basis for the microscale problem

Similar to Eq. (3.11), the reduced basis is achieved through the following approximation of the temperature dependent stress and inelastic strain fields within an enrichment domain:

$$\boldsymbol{\sigma}(\mathbf{x}, T^\alpha, t) = \sum_{\gamma=1}^{NP_\alpha} N_\gamma^\alpha(\mathbf{x})\, \boldsymbol{\sigma}_\gamma^\alpha(T^\alpha, t); \quad \boldsymbol{\varepsilon}^{vp}(\mathbf{x}, T^\alpha, t) = \sum_{\gamma=1}^{NP_\alpha} N_\gamma^\alpha(\mathbf{x})\, \boldsymbol{\mu}_\gamma^\alpha(T^\alpha, t); \quad \mathbf{x} \in \Omega_\alpha \tag{4.19}$$

where, $\boldsymbol{\sigma}_\gamma^\alpha$ and $\boldsymbol{\mu}_\gamma^\alpha$ are the stress and inelastic strain coefficients, respectively. N_γ^α denotes reduced basis shape functions; and NP_α the order of the reduced basis. The reduced basis shape functions are taken to be piecewise constant over parts of the enrichment domain as described in Eq. (3.12).

Substituting the reduced order microscale partitioning (Eqs. (4.19) and (4.13)) into Eq. (4.2), the stress coefficient for an arbitrary part Ω_η^α within the enrichment domain Ω_α is expressed as:

$$\begin{aligned} \boldsymbol{\sigma}_\eta^\alpha(T^\alpha, t) = \sum_{A=1}^{N_D} \left[\mathbf{S}_{\eta A}^\alpha(T^\alpha) \cdot \hat{\mathbf{u}}_A^{M\alpha}(T^\alpha, t) \right] + \sum_{\gamma=1}^{NP_\alpha} \left[\mathbf{P}_{\eta\gamma}^\alpha(T^\alpha) : \boldsymbol{\mu}_\gamma^\alpha(T^\alpha, t) \right] \\ + \mathbf{Z}_\eta^\alpha(T^\alpha)\,(T^\alpha - T_0) \end{aligned} \tag{4.20}$$

The homogenized coefficient tensors on each part Ω_η^α are:

$$\mathbf{S}_{\eta A}^\alpha(T^\alpha) = \frac{1}{|\Omega_\eta^\alpha|} \int_{\Omega_\eta^\alpha} \left[\mathbf{L}(\mathbf{x}, T^\alpha) \cdot \nabla N_A^\alpha(\mathbf{x}) + \mathbf{L}(\mathbf{x}, T^\alpha) : \nabla \mathbf{H}_A^\alpha(\mathbf{x}, T^\alpha) \right] d\Omega \tag{4.21}$$

$$\mathbf{P}^{\alpha}_{\eta\gamma}(T^{\alpha}) = \frac{1}{|\Omega^{\alpha}_{\eta}|}\int_{\Omega^{\alpha}_{\eta}}\left[\mathbf{L}(\mathbf{x},T^{\alpha}) : \int_{\Omega^{\alpha}_{\gamma}}\nabla\mathbf{h}^{\alpha}(\mathbf{x},\hat{\mathbf{x}},T^{\alpha})\,d\hat{\mathbf{x}} - \mathbf{L}(\mathbf{x},T^{\alpha})\,N^{\alpha}_{\gamma}(\mathbf{x})\right]\,d\Omega \tag{4.22}$$

$$\mathbf{Z}^{\alpha}_{\eta}(T^{\alpha}) = \frac{1}{|\Omega^{\alpha}_{\eta}|}\int_{\Omega^{\alpha}_{\eta}}\mathbf{L}(\mathbf{x},T^{\alpha}) : \left[\nabla\mathbf{G}^{\alpha}(\mathbf{x},T^{\alpha}) - \boldsymbol{\alpha}^{T}(\mathbf{x})\right]\,d\Omega \tag{4.23}$$

Since the homogenized coefficient tensors ($\mathbf{S}^{\alpha}_{\eta A}(T^{\alpha})$, $\mathbf{P}^{\alpha}_{\eta\gamma}(T^{\alpha})$ and $\mathbf{Z}^{\alpha}_{\eta}(T^{\alpha})$) are obtained from the influence functions which always satisfy the microscale weak form equation, the stress coefficients computed using the coefficient tensors ensures that the reduced order microscale equilibrium state is satisfied for arbitrary macroscale displacement, inelastic strain coefficient, and temperature field over the enrichment domain.

In view of the linearity of the thermal problem, the microscale temperature field is expressed as:

$$T^{m}_{\alpha}(\mathbf{x},t) = \sum_{A=1}^{N_D}\breve{H}^{\alpha}_{A}(\mathbf{x})\cdot\hat{T}^{M\alpha}_{A}(t) \tag{4.24}$$

in which, $\breve{H}^{\alpha}_{A}$ is the temperature influence function evaluated by satisfying the microscale weak form, Eq. (4.12). The resulting temperature field is:

$$T(\mathbf{x},t) = \sum_{A=1}^{N_D}\left[N_A(\mathbf{x}) + \breve{H}^{\alpha}_{A}(\mathbf{x})\right]\cdot\hat{T}^{M\alpha}_{A}(t) \tag{4.25}$$

The uniform temperature field within the enrichment domains (Eq. (4.15)) is evaluated using:

$$T^{\alpha}(t) = \sum_{A=1}^{N_D}\bar{H}^{\alpha}_{A}\;\hat{T}^{M\alpha}_{A}(t) \tag{4.26}$$

where,

$$\bar{H}^{\alpha}_{A} = \frac{1}{|\Omega_{\alpha}|}\int_{\Omega_{\alpha}}\nabla N^{\alpha}_{A}(\mathbf{x}) + \nabla\breve{H}^{\alpha}_{A}(\mathbf{x})\,d\Omega \tag{4.27}$$

4.4.2 Approximation of coefficient tensors over temperature

It is important to note that the influence functions and consequently the coefficient tensors ($\mathbf{S}^{\alpha}_{\eta A}$, $\mathbf{P}^{\alpha}_{\eta\gamma}$ and $\mathbf{Z}^{\alpha}_{\eta}$) are functions of temperature. Within a structural analysis subjected to thermo-mechanical loads where temperature field is spatially and temporally varying, the temperature-

dependent coefficient tensors need to be stored separately for each enrichment domain and updated at every increment. The update procedure requires the evaluation of the influence function problems (Eqs. (4.16)-(4.18)) and the numerical integrations (Eqs. (4.21)-(4.23)), both of which are computationally expensive. Instead, we consider the following approximation of the temperature dependence of the coefficient tensors:

$$\mathbf{S}^{\alpha}_{\eta A}(T^{\alpha}) \approx \bar{\mathbf{S}}^{\alpha}_{\eta A}(T^{\alpha};\mathbf{T}^{N_\alpha}) = \sum_{i=1}^{N_\alpha} \psi_i(T^{\alpha})\, \hat{\mathbf{S}}^{\alpha}_{\eta Ai} \tag{4.28}$$

$$\mathbf{P}^{\alpha}_{\eta \gamma}(T^{\alpha}) \approx \bar{\mathbf{P}}^{\alpha}_{\eta \gamma}(T^{\alpha};\mathbf{T}^{N_\alpha}) = \sum_{i=1}^{N_\alpha} \psi_i(T^{\alpha})\, \hat{\mathbf{P}}^{\alpha}_{\eta \gamma i} \tag{4.29}$$

$$\mathbf{Z}^{\alpha}_{\eta}(T^{\alpha}) \approx \bar{\mathbf{Z}}^{\alpha}_{\eta}(T^{\alpha};\mathbf{T}^{N_\alpha}) = \sum_{i=1}^{N_\alpha} \psi_i(T^{\alpha})\, \hat{\mathbf{Z}}^{\alpha}_{\eta i} \tag{4.30}$$

where, $\{\psi_i |\ i = 1,2,...,N_\alpha\}$ is a set of interpolation functions for the coefficient tensors. One dimensional piecewise linear Lagrangian shape functions are employed in the current study. N_α denotes the number of nodes in the temperature discretization ($\mathbf{T}^{N_\alpha}$) over a temperature range:

$$\mathbf{T}^{N_\alpha} = \{T_1, T_2, ..., T_{N_\alpha}\}^T; \quad T_1 = T_{\min} \text{ and } T_{N_\alpha} = T_{\max} \tag{4.31}$$

where, $T_{\min}$ and $T_{\max}$ denote the minimum and maximum temperature that the structure is subjected to, respectively. $\hat{\mathbf{S}}^{\alpha}_{\eta A}$, $\hat{\mathbf{P}}^{\alpha}_{\eta \gamma}$ and $\hat{\mathbf{Z}}^{\alpha}_{\eta}$ are the approximation bases for the corresponding coefficient tensors such that:

$$\begin{aligned} \hat{\mathbf{S}}^{\alpha}_{\eta A} := \left\{ \hat{\mathbf{S}}^{\alpha}_{\eta Ai} = \mathbf{S}^{\alpha}_{\eta A}(T_i) \mid T_i \in \mathbf{T}^{N_\alpha} \right\}^T; \;\; \hat{\mathbf{P}}^{\alpha}_{\eta \gamma} := \left\{ \hat{\mathbf{P}}^{\alpha}_{\eta \gamma i} = \mathbf{P}^{\alpha}_{\eta \gamma}(T_i) \mid T_i \in \mathbf{T}^{N_\alpha} \right\}^T; \\ \hat{\mathbf{Z}}^{\alpha}_{\eta} := \left\{ \hat{\mathbf{Z}}^{\alpha}_{\eta i} = \mathbf{Z}^{\alpha}_{\eta}(T_i) \mid T_i \in \mathbf{T}^{N_\alpha} \right\}^T \end{aligned} \tag{4.32}$$

For an arbitrary microstructure, the coefficient tensors for each temperature in $\mathbf{T}^{N_\alpha}$ are evaluated a-priori and stored for the approximation.

4.4.3 Identification of the temperature approximation basis

The accuracy of the approximation stated in Eqs. (4.28) - (4.30) directly depends on proper identification of $\mathbf{T}^{N_\alpha}$, which in turn depends on the variation of the elastic properties of each microstructural constituent as a function of temperature. The optimum $\mathbf{T}^{N_\alpha}$ should contain the smallest number of basis nodes that confine the error between the directly computed (Eqs. (4.21)-(4.23)) and the approximated (Eqs. (4.28)-(4.30)) coefficient tensors. Consequently, the identification of the approximation basis is posed as an optimization problem. We seek to find the optimal basis node set ($\mathbf{T}^{N_\alpha^*}_{\text{opt}}$) for fixed N_α^*, such that

$$\begin{aligned} E_r({N_\alpha}^*) = \min_{\mathbf{T}^{N_\alpha^*}} \Bigg\{ \max \Bigg[& \left\| \mathbf{S}_{\eta A}(T^\alpha) - \bar{\mathbf{S}}_{\eta A}(T^\alpha; \mathbf{T}^{N_\alpha^*}) \right\|_\infty, \\ & \left\| \mathbf{P}_{\eta\gamma}(T^\alpha) - \bar{\mathbf{P}}_{\eta\gamma}(T^\alpha; \mathbf{T}^{N_\alpha^*}) \right\|_\infty, \left\| \mathbf{Z}_{\eta}(T^\alpha) - \bar{\mathbf{Z}}_{\eta}(T^\alpha; \mathbf{T}^{N_\alpha^*}) \right\|_\infty \Bigg] \Bigg\}; \\ & \forall\ \eta, \gamma = 1, 2, ..., NP_\alpha \text{ and } A = 1, 2, ..., N_D;\ \ T^\alpha \in [T_{\min}, T_{\max}] \end{aligned} \tag{4.33}$$

It is trivial to observe that the error (E_r) is non-increasing with N_α^*, e.g., $E_r({N_\alpha}^*) \geq E_r({N_\alpha}^* + 1)$. The optimal basis order is then the smallest N_α^*, such that

$$E_r(N_\alpha) \leq TOL \tag{4.34}$$

and the corresponding basis set is $\mathbf{T}^{N_\alpha}$. TOL denotes the tolerance. It is possible to evaluate Eq. (4.33) using traditional optimization methods. In order to reduce the computational cost associated with solving influence function problems at each iteration of the optimization operation, an alternative of Eq. (4.33) is used:

$$E_r({N_\alpha}^*) = \min_{\mathbf{T}^{N_\alpha^*}} \left\{ \left\| \mathbf{L}_\eta(T^\alpha) - \bar{\mathbf{L}}_\eta \right\|_\infty \right\};\quad \forall\ \eta = 1, 2, ..., NP_\alpha \tag{4.35}$$

where, $\mathbf{L}_\eta$ is the temperature-dependent tensor of elastic moduli and $\bar{\mathbf{L}}_\eta$ is its discrete approximation. Equations (4.35) and (4.34) are numerically evaluated for the optimum $\mathbf{T}^{N_\alpha}$ using the

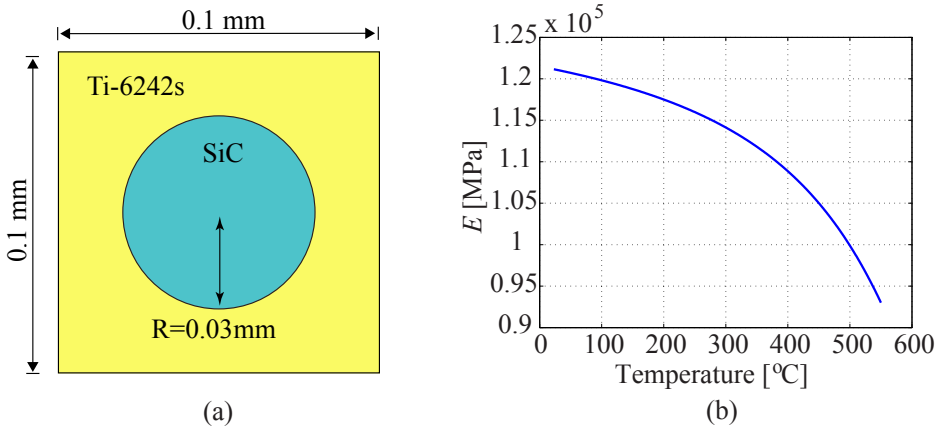

Figure 4.2: (a) Microstructure of the SiC/Ti-6242s composite; and (b) temperature dependence of Young's modulus for the Ti-6242s matrix.

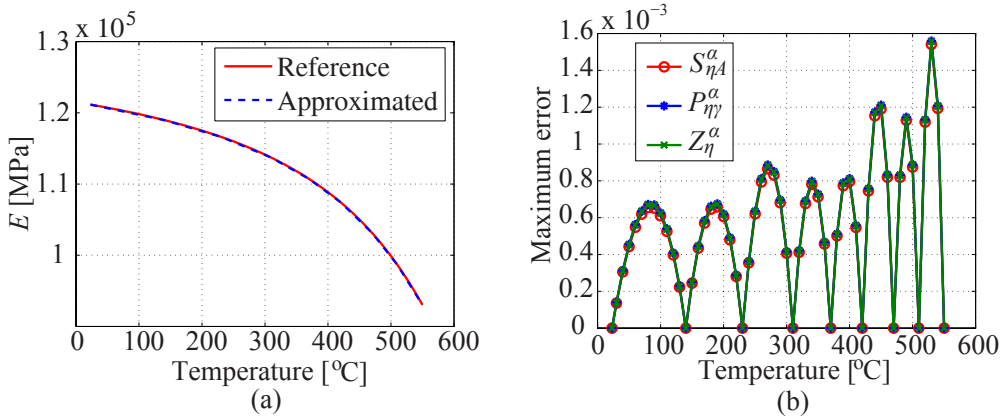

Figure 4.3: Performance of the determined temperature basis for : (a) approximated Young's modulus of Ti-6242s; and (b) maximum errors in the approximated coefficient tensors.

adaptive approximation method [79, 80].

To further illustrate the procedure stated above, we consider an example for a SiC/Ti-6242s composite material [81, 82, 83, 84]. The microstructure of the SiC/Ti-6242s composite is shown in Fig. 4.2(a). The silicon carbide fiber (SiC) is assumed to be temperature-independent and isotropic, with Young's modulus and Poison's ratio of 395 GPa and 0.25, respectively. The Young's modulus of the matrix material (Ti-6242s) is taken to be temperature-dependent, as shown in Fig. 4.2(b) [85]. The Poison's ratio of the matrix is taken as temperature-independent, ν=0.32. Through adaptive approximation with 10°C as the minimum partition interval, the optimum temperature

approximation basis is determined as $\mathbf{T}^{N_\alpha}$=$\{23, 140, 230, 310, 370, 420, 470, 510, 550\}$. It contains 9 temperature nodes and the approximated Young's modulus function is plotted in Fig. 4.3(a). The tolerance employed is 0.003 in the current example. Using the determined $\mathbf{T}^{N_\alpha}$, the maximum errors between the approximated and directly computed coefficient tensors are presented in Fig 4.3(b).

With the properly approximated coefficient tensors, the thermal and mechanical problems are evaluated incrementally in a staggered fashion, since the two problems include one-way coupling only (i.e., effect of temperature on mechanical response). The coupled temperature and mechanical response fields are solved separately, through separation of variables. The mechanical ROVME system under temperature effect is linearized and numerically assessed through a Newton-Raphson iterative scheme. The formulation and implementation for the numerical evaluation of the temperature dependent ROVME system for elasto-viscoplastic materials are detailed in Ref. [86]. They are skipped herein for the simplicity of presentation.

4.5 Computational Implementation

This section provides the numerical implementation of the reduced order variational multiscale enrichment method for thermo-mechanical problems, along with an implementation strategy. The implementation of the direct VME method for mechanical problems under temperature effect (employed in the verification of the ROVME method) is listed in Ref. [86]. The thermal and mechanical problems are evaluated incrementally in a staggered fashion, since the two problems include one-way coupling only (i.e., effect of temperature on mechanical response). The coupled temperature and mechanical response fields are solved separately, through separation of variables. With the assumption that the enrichment domains are sufficiently small, the uniform temperature field (T^α) of each enrichment domain (Ω_α) is obtained by homogenizing the temperature field of the enriched macroscale element.

Considering the discrete set of instances with the observation period ($\{0, {}_1t, {}_2t, ..., {}_nt, {}_{n+1}t, ..., t_e\}$) and taking the temperature field as a known variable at each time step, the elasto-viscoplastic me-

chanical problem under temperature effect is numerically assessed through a Newton-Raphson iterative scheme summarized below. For simplicity of the presentation, the superscript, α, has been omitted from the response variable in the implementation described below.

4.5.1 ROVME formulation in an arbitrary enrichment domain

The rate-form constitutive equation for an arbitrary part, Ω_η^α, is obtained by taking the time derivative of Eq. (4.20):

$$\begin{aligned}\dot{\boldsymbol{\sigma}}_\eta(t) = &\sum_{A=1}^{N_D}\left[\mathbf{S}_{\eta A}(T)\cdot\dot{\hat{\mathbf{u}}}_A^M(T,t)\right] + \sum_{\gamma=1}^{NP}\left[\mathbf{P}_{\eta\gamma}(T):\dot{\boldsymbol{\mu}}_\gamma(T,t)\right] + \mathbf{Z}_\eta(T)\,\dot{T} \\ &+ \sum_{A=1}^{N_D}\left[\frac{\partial \mathbf{S}_{\eta A}(T)}{\partial T}\dot{T}\cdot\hat{\mathbf{u}}_A^M(T,t)\right] + \sum_{\gamma=1}^{NP}\left[\frac{\partial \mathbf{P}_{\eta\gamma}(T)}{\partial T}\dot{T}:\boldsymbol{\mu}_\gamma(T,t)\right] + \frac{\partial \mathbf{Z}_\eta(T)}{\partial T}\,\dot{T}(T-T_0)\end{aligned} \tag{4.36}$$

Considering the viscoplastic slip evolution of the ROVME method for each part Ω_γ^α in the enrichment domain (Eq. (3.21)) and performing time discretization of Eq. (4.36), the residual of the constitutive equation for an arbitrary part Ω_η^α yields:

$$\begin{aligned}\mathbf{R}_\eta \equiv\ & {}_{n+1}\boldsymbol{\sigma}_\eta - {}_n\boldsymbol{\sigma}_\eta - \sum_{A=1}^{N_D} {}_{n+1}\mathbf{S}_{\eta A}\cdot\left({}_{n+1}\hat{\mathbf{u}}_A^M - {}_n\hat{\mathbf{u}}_A^M\right) - (1-\theta)\,\Delta t\sum_{\gamma=1}^{NP} {}_{n+1}\mathbf{P}_{\eta\gamma}:{}_n\dot{\boldsymbol{\mu}}_\gamma \\ & - \theta\,\Delta t\sum_{\gamma=1}^{NP} {}_{n+1}\mathbf{P}_{\eta\gamma}:{}_{n+1}\dot{\boldsymbol{\mu}}_\gamma - {}_n\mathbf{Z}_\eta\ \left({}_{n+1}T - {}_nT\right) \\ & - \sum_{A=1}^{N_D} {}_{n+1}\left(\frac{\partial \mathbf{S}_{\eta A}}{\partial T}\right)\cdot{}_{n+1}\hat{\mathbf{u}}_A^M\ \left({}_{n+1}T - {}_nT\right) - \sum_{\gamma=1}^{NP} {}_{n+1}\left(\frac{\partial \mathbf{P}_{\eta\gamma}}{\partial T}\right):\ {}_{n+1}\boldsymbol{\mu}_\gamma\ \left({}_{n+1}T - {}_nT\right) \\ & - {}_{n+1}\left(\frac{\partial \mathbf{Z}_\eta}{\partial T}\right)\ \left({}_{n+1}T - {}_nT\right)\left({}_{n+1}T - T_0\right) = 0\end{aligned} \tag{4.37}$$

in which, the left subscript n and $n+1$ denote the value of a field variable at ${}_nt$ and ${}_{n+1}t$, respectively. The equilibrium states and response fields of the nonlinear system at ${}_nt$ is the "known" configuration. The temperature field (${}_{n+1}T$) and the coefficient tensors (${}_{n+1}\mathbf{S}_{\eta A},\ {}_{n+1}\mathbf{P}_{\eta\gamma},\ {}_{n+1}\mathbf{Z}_\eta$) are known at ${}_{n+1}t$. The temperature derivatives of the coefficient tensors ${}_{n+1}(\partial\mathbf{S}_{\eta A}/\partial T)$, ${}_{n+1}(\partial\mathbf{P}_{\eta\gamma}/\partial T)$ and ${}_{n+1}(\partial\mathbf{Z}_\eta/\partial T)$ are assessed numerically. In the remainder of this section, the left subscript

$n+1$ of the fields at the current time step is omitted for simplicity of the presentation. Forming a Newton iteration through a first order Taylor series approximation of Eq. (4.37), the residual of the stress-strain equation yields:

$$\begin{aligned}\mathbf{R}_{\eta}^{k+1} \approx & \mathbf{R}_{\eta}^{k}+\sum_{\gamma=1}^{NP}\left[\left(\delta_{\eta\gamma}^{K}\,\mathbf{I}-\theta\;\Delta t\;\mathbf{P}_{\eta\gamma}:\mathbf{C}_{\gamma}^{k}\right):\delta\boldsymbol{\sigma}_{\gamma}\right]-\sum_{\gamma=1}^{NP}\left(\theta\;\Delta t\;\mathbf{P}_{\eta\gamma}:\mathbf{G}_{\gamma}^{k}+\mathbf{D}_{\eta\gamma}\right):\delta\boldsymbol{\mu}_{\gamma} \\ & -\sum_{A=1}^{N_D}\left(\tilde{\mathbf{S}}_{\eta A}\cdot\delta\hat{\mathbf{u}}_{A}^{M}\right)=0\end{aligned} \tag{4.38}$$

where,

$$\mathbf{D}_{\eta\gamma}=\left(\frac{\partial\mathbf{P}_{\eta\gamma}}{\partial T}\right)(T-{}_{n}T);\quad \tilde{\mathbf{S}}_{\eta A}=\mathbf{S}_{\eta A}+\left(\frac{\partial\mathbf{S}_{\eta A}}{\partial T}\right)(T-{}_{n}T) \tag{4.39}$$

Taylor series approximation does not include the derivative with respect to the temperature field, since it is taken as a known variable for the mechanical problem. Considering the first order Taylor series approximation of the residual of the kinematic equation (Eq. (3.27)), the inelastic coefficients are condensed out to yield:

$$\sum_{\gamma=1}^{NP}\left(\mathbf{Q}_{\eta\gamma}^{k}:\delta\boldsymbol{\sigma}_{\gamma}\right)=\sum_{A=1}^{N_D}\left(\tilde{\mathbf{S}}_{\eta A}:\delta\hat{\mathbf{u}}_{A}^{M}\right)-\mathbf{V}_{\eta}^{k} \tag{4.40}$$

where, $\mathbf{Q}_{\eta\gamma}^{k}$ and $\mathbf{V}_{\eta}^{k}$ are defined as:

$$\begin{aligned}\mathbf{Q}_{\eta\gamma}^{k}= & \delta_{\eta\gamma}^{K}\,\mathbf{I}-\theta\;\Delta t\;\mathbf{P}_{\eta\gamma}:\mathbf{C}_{\gamma}^{k} \\ & -\theta\;\Delta t\;\left(\theta\;\Delta t\;\mathbf{P}_{\eta\gamma}:\mathbf{G}_{\gamma}^{k}+\mathbf{D}_{\eta\gamma}\right):\left(\mathbf{I}-\theta\;\Delta t\;\mathbf{G}_{\gamma}^{k}\right)^{-1}:\mathbf{C}_{\gamma}^{k}\end{aligned} \tag{4.41}$$

$$\mathbf{V}_{\eta}^{k}=\mathbf{R}_{\eta}^{k}+\sum_{\gamma=1}^{NP}\left(\theta\;\Delta t\;\mathbf{P}_{\eta\gamma}:\mathbf{G}_{\gamma}^{k}+\mathbf{D}_{\eta\gamma}\right):\left(\mathbf{I}-\theta\;\Delta t\;\mathbf{G}_{\gamma}^{k}\right)^{-1}:\boldsymbol{\lambda}_{\gamma}^{k} \tag{4.42}$$

The stress increment vector for the enrichment domain is obtained in the form identical to Eq. (3.31), where

$$\mathbf{S}=\left[\tilde{\mathbf{S}}_{\eta A}\right]_{\eta\in[1,NP],A\in[1,N_D]} \tag{4.43}$$

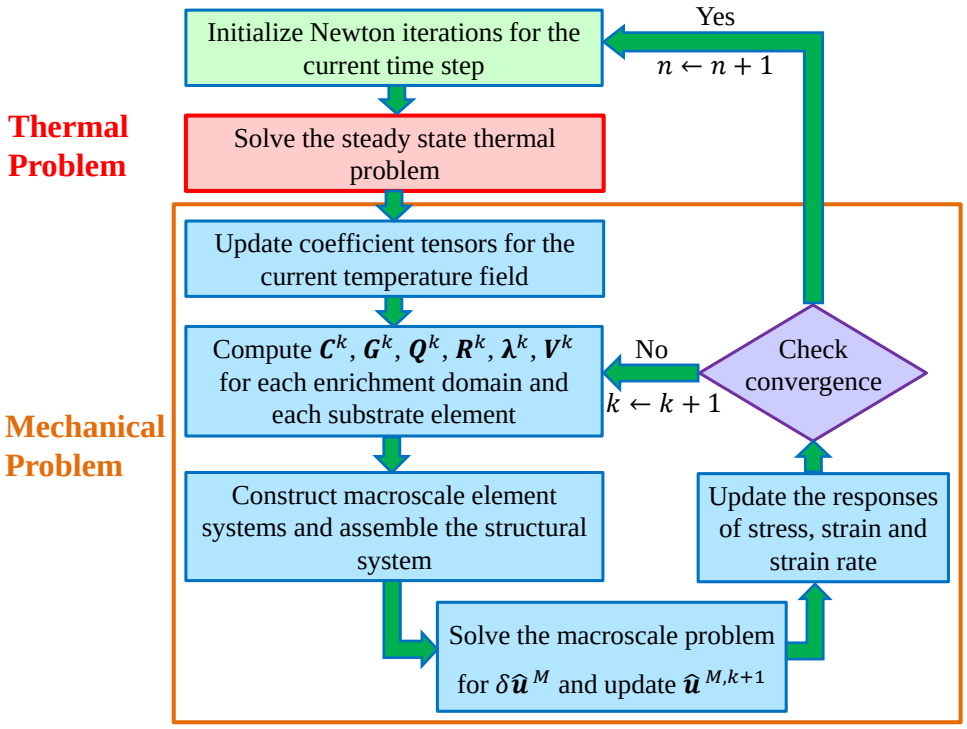

Figure 4.4: Reduced order variational multiscale enrichment implementation strategy (the subscripts , γ and η, indicating parts in enrichment domains are omitted for clarity).

In the presence of the stress increment vector for enrichment domains, the number evaluation of the macroscale problem can be achieved following the algorithm provided in Section 3.3.2.

4.5.2 ROVME implementation algorithm

The implementation of the formulation is performed using the commercial software package, Diffpack [68], in C++ computer language. The overall implementation strategy is summarized in Fig. 4.4, where the microscale superscript (α) and part subscript (γ) are omitted for clarity. In the preprocessing phase prior to the simulation, the coefficient tensors ($\mathbf{S}_{\eta A}(T)$, $\mathbf{P}_{\eta\gamma}(T)$ and $\mathbf{Z}_{\eta}(T)$) at each temperature in $\mathbf{T}^N$ are computed using Eqs. (4.21), (4.22), (4.23) and stored ($A = 1,2,...,N_D$; γ and $\eta = 1,2,...,NP$) for each enrichment domain. The temperature influence function ($\breve{H}_A^{\alpha}$) and the homogenization tensor ($\bar{H}_A^{\alpha}$) are also evaluated and stored for each enrichment domain ($A = 1,2,...,N_D$). At an arbitrary time ${}_nt$, the system is in equilibrium with the constitutive relations satisfied for the problem domain. The algorithm seeks to find the equilibrium state at ${}_{n+1}t$ as

follows:

Given: ${}_n\hat{\mathbf{u}}^M, {}_n\boldsymbol{\sigma}, {}_n\varepsilon^{vp}$ and ${}_n\dot{\varepsilon}^{vp}$ (${}_n\boldsymbol{\mu}_\gamma$ and ${}_n\dot{\boldsymbol{\mu}}_\gamma$ for enrichment domains) at time ${}_nt$.

Find: $\hat{\mathbf{u}}^M, \boldsymbol{\sigma}, \varepsilon^{vp}$ and $\dot{\varepsilon}^{vp}$ ($\boldsymbol{\mu}_\gamma$ and $\dot{\boldsymbol{\mu}}_\gamma$ for enrichment domains) at time ${}_{n+1}t$.

1. Initialize by setting: k=0, $\hat{\mathbf{u}}^{M,0} = {}_n\hat{\mathbf{u}}^M$, $\boldsymbol{\sigma}^0 = {}_n\boldsymbol{\sigma}$, $\varepsilon^{vp,0} = {}_n\varepsilon^{vp}$, and $\dot{\varepsilon}^{vp,0} = {}_n\dot{\varepsilon}^{vp}$ ($\boldsymbol{\mu}_\gamma^0 = {}_n\boldsymbol{\mu}_\gamma$, and $\dot{\boldsymbol{\mu}}_\gamma^0 = {}_n\dot{\boldsymbol{\mu}}_\gamma$ for enrichment domains).

2. Solve the steady state thermal problem for the current time, and for each enrichment domain (Ω_α, $\alpha = 1, 2, ..., n_{\text{en}}$):

   (1) Homogenize the temperature field over the enrichment domain (Eq. (4.26)).

   (2) Update the coefficient tensors ($\mathbf{S}_{\eta A}(T)$, $\mathbf{P}_{\eta\gamma}(T)$ and $\mathbf{Z}_\eta(T)$) using Eqs. (4.28)-(4.30).

   (3) Evaluate $\mathbf{D}_{\eta\gamma}$ and $\tilde{\mathbf{S}}_{\eta A}$ from Eq. (4.39) and assemble $\mathbf{S}$ using Eq. (4.43).

3. Loop over all enrichment domains:

   (1) Compute $\mathbf{C}_\gamma^k$, $\mathbf{G}_\gamma^k$, $\mathbf{Q}_{\eta\gamma}^k$, $\mathbf{R}_\eta^k$, $\boldsymbol{\lambda}_\eta^k$, $\mathbf{V}_\eta^k$, $\mathbf{Q}^k$ and $\mathbf{V}^k$ from Eqs. (3.25), (4.41), (4.37), (3.26), (4.42), (4.43) and (3.33c) .

   (2) Construct $\mathbf{K}$ and $\delta\mathbf{f}$ for the current enrichment domain using Eqs. (3.45) and (3.46).

4. Following the standard finite element procedure, construct the macroscale elementary stiffnesses for the substrate elements and assemble the macroscale system.

5. Solve the macroscale problem for $\delta\hat{\mathbf{u}}^M$ and update the macroscale displacement field ($\hat{\mathbf{u}}^{M,k+1} = \hat{\mathbf{u}}^{M,k} + \delta\hat{\mathbf{u}}^M$).

6. Loop over all enrichment domains:

   (1) Determine the stress coefficient increment $\delta\boldsymbol{\sigma}$ (Eq. (3.31)) and update the stress coefficient $\boldsymbol{\sigma}^{k+1} = \boldsymbol{\sigma}^k + \delta\boldsymbol{\sigma}$.

   (2) Evaluate the inelastic strain coefficient increment $\delta\boldsymbol{\mu}_\gamma$ (Eq. (3.27)) and update the inelastic strain coefficient $\boldsymbol{\mu}_\gamma^{k+1} = \boldsymbol{\mu}_\gamma^k + \delta\boldsymbol{\mu}_\gamma$.

Table 4.1: Materials parameters for phase II material in the microstructure.

Property	E_0 [GPa] [1]	ν	A [MPa]	B [MPa]	m	n
Value	120.8	0.32	895	125	0.85	0.2
Property	T_{room} [$^{\text{o}}$C]	T_{melt} [$^{\text{o}}$C]	γ [MPa/second]	q	α^T [1/$^{\text{o}}$C]	k [W/mK]
Value	23	1700	25	1.0	7.7×10^{-6}	20

(3) Compute the inelastic strain rate coefficient $\dot{\boldsymbol{\mu}}_\gamma$ using the evolution equation of the material.

7. Loop over all substrate elements to update stress ($\boldsymbol{\sigma}^{k+1}$), strain ($\boldsymbol{\varepsilon}^{vp,k+1}$) and strain rate ($\dot{\boldsymbol{\varepsilon}}^{vp,k+1}$) using classical response update procedures [24].

8. Check for convergence:

$$\mathrm{e}^M = \frac{\|\hat{\mathbf{u}}^{M,k+1} - \hat{\mathbf{u}}^{M,k}\|_2}{\|\hat{\mathbf{u}}^{M,k+1} - {}_n\hat{\mathbf{u}}^M\|_2} \leq \text{Convergence tolerance} \tag{4.44}$$

9. If convergence is not satisfied, set iteration counter $k \leftarrow k+1$ and proceed with the next iteration.

4.6 Numerical Verification

The verifications of the ROVME method particularly focus on the coupling effects in the thermo-mechanical behavior. The accuracy characteristics of the ROVME method is assessed by comparing the results with the direct VME approach, as well as with the single scale finite element method (FEM), in which the heterogeneous microstructure is resolved within the enrichment region. A two-phase particulate composite with circular inclusions is employed (Fig. 4.2(a)). Phase I is the silicon carbide constituent, taken to be elastic with Young's modulus (E) of 395 GPa, Poisson's ratio (ν) of 0.25, the thermal expansion coefficient (α) of $4.2\times10^{-6}/^{\text{o}}$C and the thermal conductivity (k) of 120 W/mK [87, 84]. Phase II is Ti-6242s, taken to be elasto-viscoplastic [88, 89].

[1] E_0 denotes the Young's modulus at the room temperature.

The flow stress is expressed using the modified Johnson-Cook model [77, 53]:

$$\sigma_y = [A + B(\bar{\varepsilon}^{vp})^n]\,[1 - (T^*)^m] \tag{4.45}$$

where, A, B, n and m are material parameters; $\bar{\varepsilon}^{vp}$ the effective viscoplastic strain and T^* is the non-dimensional temperature:

$$T^* = \frac{T - T_{\text{room}}}{T_{\text{melt}} - T_{\text{room}}} \tag{4.46}$$

where, T_{room} and T_{melt} are the room and melting temperatures, respectively. Instead of incorporating the strain rate term directly as in the standard Johnson-Cook model, the strain rate effect is modeled through the Perzyna formulation [24, 39] as described in Eq. (2.5). The values of the parameters for Ti-6242s are shown in Table 4.1, in which γ is the fluidity parameter and q is the viscoelastic hardening parameter. The Young's modulus of Ti-6242s is taken to vary as a function of temperature as shown in Fig. 4.2(b). Phase III denotes the homogenized composite used in the substrate region, the properties of which are computed using the rule of mixtures and taken to remain elastic [81, 83]. The Young's modulus of Phase III at the room temperature is 170 GPa and linearly drops to 140 GPa at 550°C. The Poisson's ratio is 0.3. The thermal expansion coefficient is $5.0\times10^{-6}/^{o}$C and the thermal conductivity is 48 W/mK.

A 2-D plane strain, 3 mm $\times$ 0.3mm, composite beam is considered. Due to symmetry, only half of the beam is discretized. The ratio between the size of the enrichment domain and the size of the critical subregion is 1/5. The macro- and microscale discretization for the ROVME and VME models are shown in Fig. 4.5, along with the reference finite element discretization. The macroscale discretization, Fig. 4.5(b), contains 64 nodes and 45 quadrilateral finite elements. The enrichment region contains 15 macroscale elements, and is positioned close to the center of the beam since the center of the beam has the largest deformation and stress state under the applied loads. Each of the enrichment domains contains a phase I inclusion at the center, and a phase II matrix. The particle volume fraction is 28.3% [81, 83, 84]. The ROVME model of the enrichment domain (Fig. 4.5(d)) consists of 2 parts that corresponds to the domains of the constituents, and

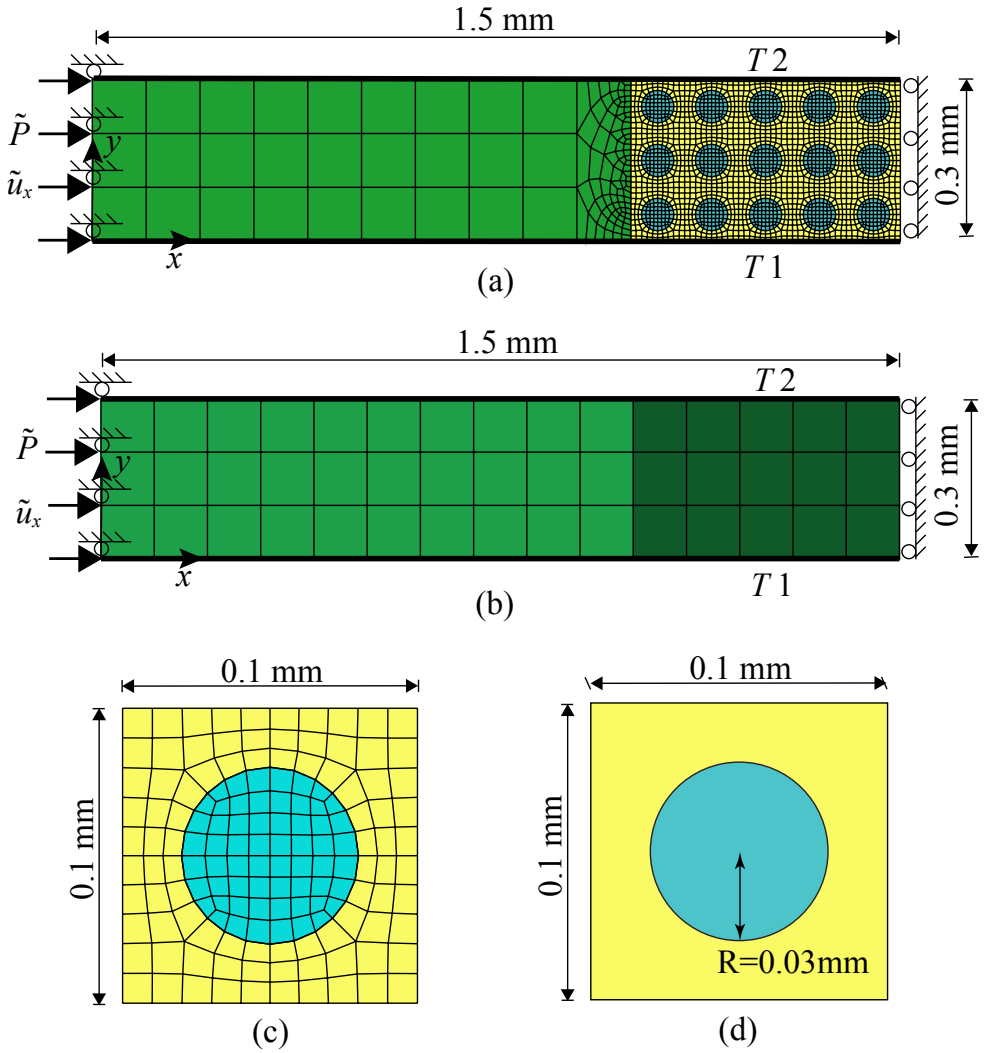

Figure 4.5: Model sketch and discretization of: (a) finite element method; (b) macroscale problem of the VME and ROVME methods; (c) microscale problem of the VME method; and (d) microscale problem of the ROVME method with 2 parts.

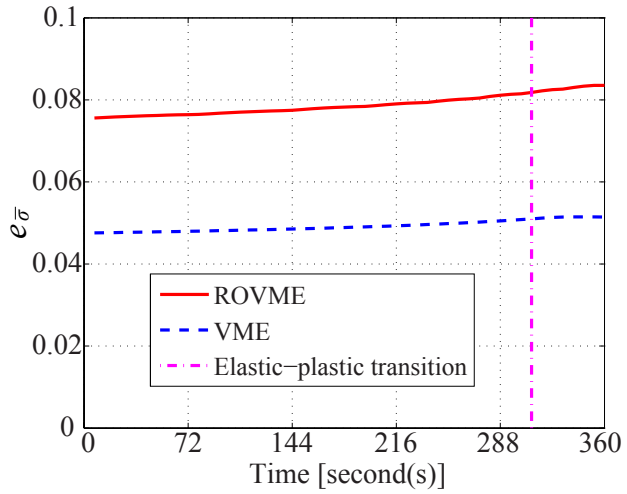

Figure 4.6: Errors in equivalent stress for specimen with uniform temperature field.

6 degrees of freedom (DOFs). Each VME microstructure (Fig. 4.5(c)) is discretized using 148 quadrilateral elements and 338 DOFs. The corresponding direct finite element mesh (Fig. 4.5(a)) contains 2,340 quadrilateral elements and 4,844 DOFs. The temperatures in $\mathbf{T}^{N\alpha}$ as determined in Section 4.4.3 is employed for the approximation of the ROVME coefficient tensors.

4.6.1 Specimen subjected to uniform temperature field

The first specimen is confined at both ends (i.e., $\tilde{u}_x = 0$ and $\tilde{P} = 0$ in Fig. 4.5(a) and (b)) subjected to uniform temperature field that monotonically increases from 23°C to 550°C in 6 minutes. The mechanical deformation of the specimen is therefore induced by the thermal expansions only. The time step size is set to 0.72 second. Further reduction in the time step size does not significantly improve the results. To investigate the performance of the ROVME and VME models compared with the reference model, the stress error over the enrichment region at an arbitrary time, t, is computed:

$$e_{\bar{\sigma}}(t) = \frac{\sum_{\alpha=1}^{n_{\text{en}}} \sum_{\gamma=1}^{NP_\alpha} \left\| \bar{\sigma}_\gamma^{\text{FEM}}(t) - \bar{\sigma}_\gamma(t) \right\|_{2,\Omega_\gamma^\alpha}}{\sum_{\alpha=1}^{n_{\text{en}}} \sum_{\gamma=1}^{NP_\alpha} \left\| \bar{\sigma}_\gamma^{\text{FEM}}(t) \right\|_{2,\Omega_\gamma^\alpha}} \tag{4.47}$$

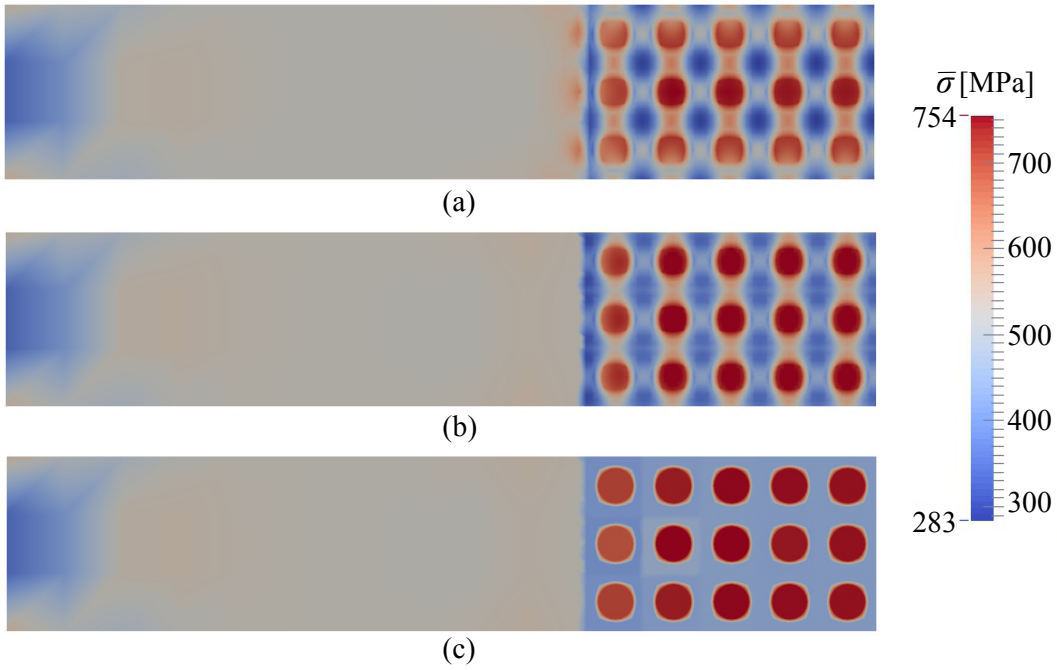

Figure 4.7: Equivalent stress contours of the specimen with uniform temperature field: (a) finite element model; (b) direct VME model; and (c) ROVME model.

where, $\bar{\sigma}_\gamma^{\text{FEM}}$ and $\bar{\sigma}_\gamma$ denote the homogenized equivalent stress over part, Ω_γ^α, obtained from the direct finite element method and the model being assessed (VME or ROVME), respectively. $\|\cdot\|_{2,\Omega_\gamma^\alpha}$ is the L_2 norm of the response field computed over Ω_γ^α. The equivalent stress errors for the ROVME and direct VME methods are shown in Fig. 4.6 as a function of time. Until temperature reaches 477°C ($t = 310$ seconds), the structure deforms elastically. Further heating causes plastic deformation as marked by the elastic-plastic transition line in Fig. 4.6. The maximum errors occur at the end of the simulation, and are less than 8.4% and 5.2% for the ROVME and VME models, respectively. The primary cause of the errors in the VME model is the microscale boundary condition, which leads to more rigid reactions than the reference model. The ROVME model displays slightly higher errors primarily due to the kinematic constraints imposed by Eq. (4.19). The slight increase in error as a function of time within the elastic loading stage is attributed to the increase in the stiffness contrast between the inclusion and the matrix as a function of temperature. Larger stiffness contrast leads to slightly higher errors as demonstrated in Ref. [39].

Figure 4.7 presents the equivalent stress contours of the structure at the end of the simula-

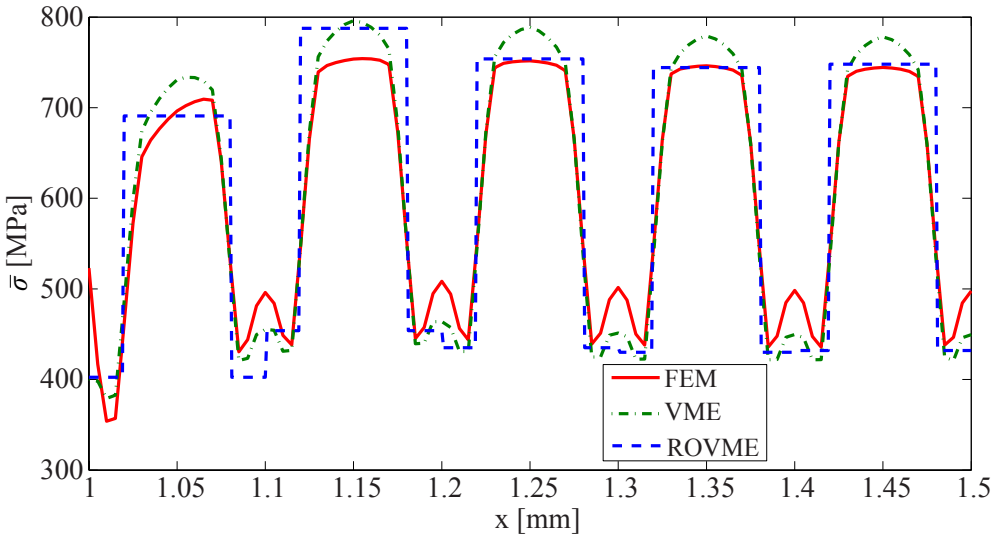

Figure 4.8: Equivalent stresses over a line (x=1.0-1.5 mm, y=0.15 mm) on the specimen with uniform temperature field.

tion predicted by the reference, VME and ROVME models. The stress contours of the VME and ROVME models are obtained by embedding the response of each enrichment domain into the coarse response field at post-processing. The stress contours computed by the VME and the ROVME approaches show slightly stiffer response compared with the reference solution due to constrained kinematics, but are able to capture the local and global stress distributions with reasonable accuracy. The equivalent stress over the line at the center of the enrichment region (x=1.0-1.5 mm, y=0.15 mm in Fig. 4.5 (a) and (b)) is plotted for all of the models, as shown in Fig. 4.8. Although the peak values of the ROVME model are closer to the results of the reference solution, the direct VME model generally follows the stress variation of the reference model more closely. Since the stress is taken to be constant over each part, the ROVME method does not resolve the stress variation around the inter-enrichment domain interfaces. The computational cost for the ROVME simulation is 5.58 minutes while for the finite element simulation is 63.8 minutes. The ROVME is 11.43 times faster than the reference model for the current example, which demonstrates the efficiency of the proposed method.

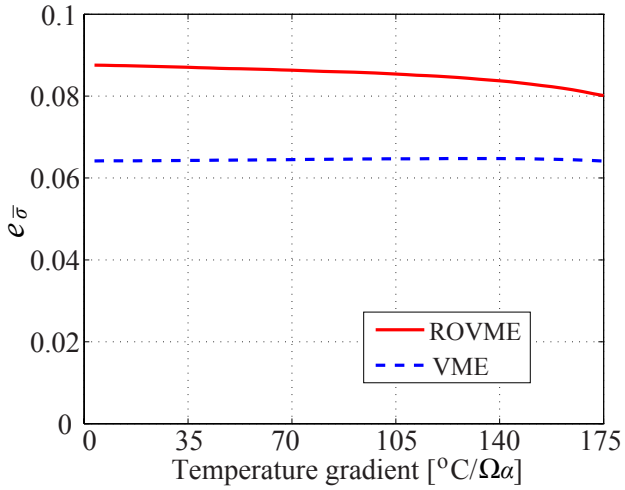

Figure 4.9: Errors in equivalent stress for the specimen with temperature gradient.

4.6.2 Specimen subjected to temperature gradient

To further verify the proposed approach, the accuracy is assessed in the context of a specimen subjected to temperature gradient. The mechanical boundary conditions of the specimen are identical to that discussed in Section 4.6.1. The temperature field $T1$ (in Fig. 4.5(a) and (b)) along the bottom edge of the specimen linearly increases from 23^{o}C (at $t = 0$) to 550^{o}C (at $t = 360$ seconds), while the temperature field $T2$ along the top edge remains constant at 23^{o}C. The time step size is set to 0.72 second. At the end of the simulation, the temperature variation across an enrichment domain is significant (approximately 175^{o}C per enrichment domain) which clearly violates the assumption that the temperature field is uniform over each enrichment domain. This example is performed to test the capability of the proposed method at or beyond the limits of the above stated assumptions.

The errors in equivalent stress for the VME and ROVME models are shown in Fig. 4.9, along with the temperature gradient. The structure remains in the elastic state during the simulation. Both VME and ROVME methods produce higher errors than the previous example (Fig. 4.6), partially because the uniform temperature field assumption is violated. The stress error of the VME method is stable, while the error of the ROVME method slightly reduces as the temperature gradient increases. The largest error in equivalent stress for the ROVME model is 8.8% and for

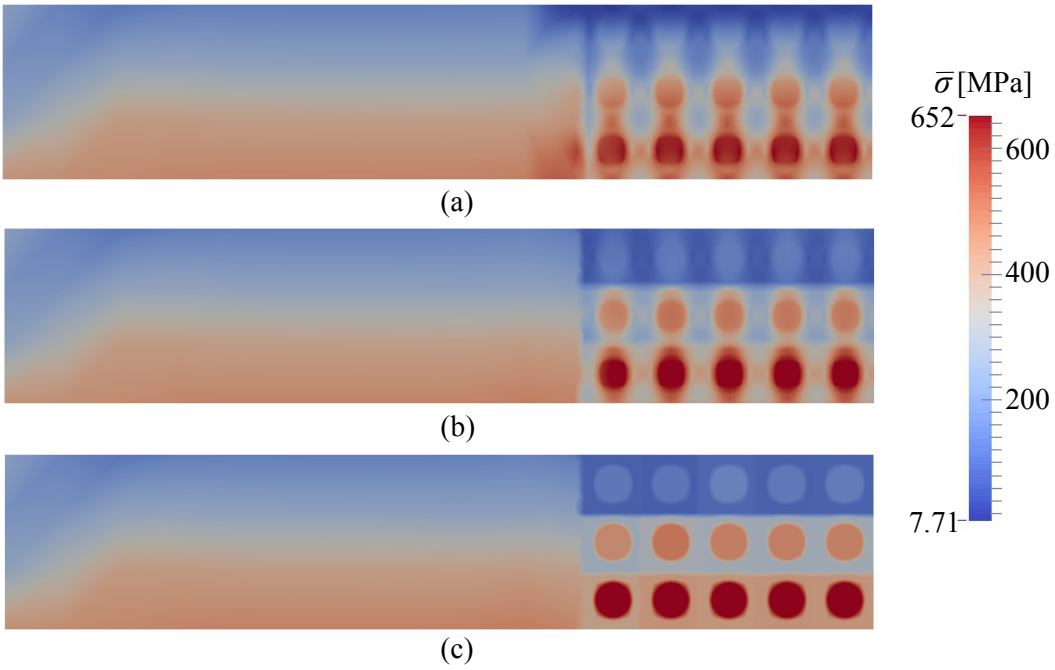

Figure 4.10: Equivalent stress contours of the specimen with temperature gradient: (a) finite element model; (b) direct VME model; and (c) ROVME model.

the direct VME method is 6.5%. The equivalent stress contours of the models at the end of the simulation are shown in Fig. 4.10, for all of the models. The contours of the direct VME and ROVME models are less smooth than the finite element method, while still closely follow the stress distribution of the reference model. The computational cost for the ROVME simulation is 5.8 minutes while for the finite element simulation is 63.3 minutes. The ROVME method is 10.91 times faster than FEM for this example.

4.6.3 Specimen subjected to combined thermo-mechanical loading

To further study the performance of the proposed methodology, a specimen subjected to combined thermal and mechanical loading is investigated. The time history of the applied boundary conditions $T1$, $T2$ and $\tilde{P}$ are shown in Fig. 4.11. The bottom and top edges of the specimen are heated at the same rate up to 200^{o}C and 150^{o}C, respectively. Then the temperatures are kept constant. Between t = 270 - 360 seconds, the specimen is exposed to a monotonically increasing

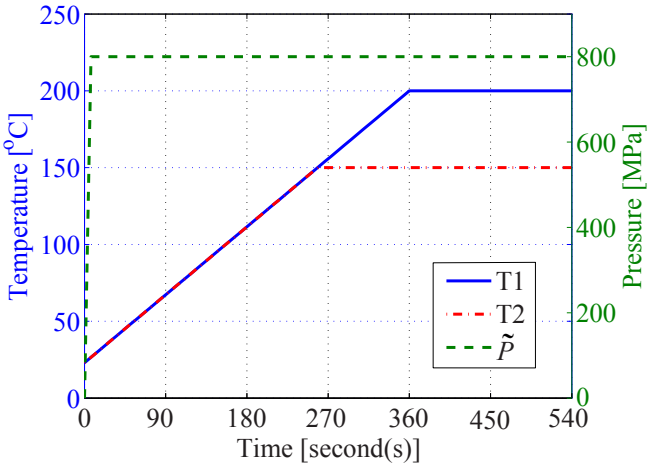

Figure 4.11: Loading conditions of the specimen with pressure.

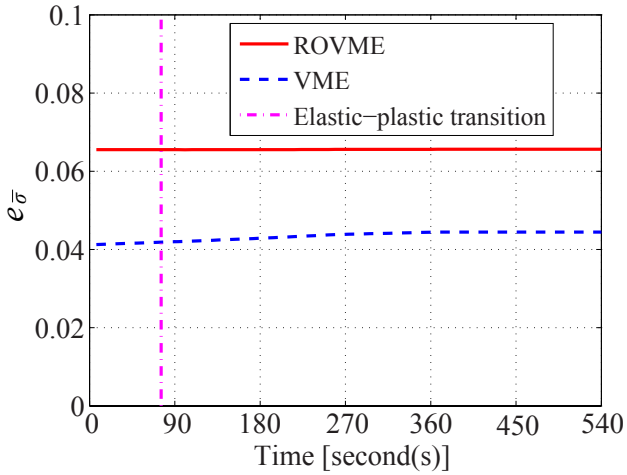

Figure 4.12: Errors in equivalent stress for the specimen with pressure.

temperature gradient. The specimen is also subjected to a constant boundary pressure of 800 MPa. The time step size of the current example is set to 0.36 second.

The time history of error in equivalent stress is presented in Fig. 4.12. Until $t = 76$ seconds, the specimen deforms elastically. The inelastic deformation initiates at $t = 76$ seconds, induced by the increasing thermal stress. After $t = 360$, the errors become steady for both VME and ROVME methods, since the loading conditions remain the same and the specimen deforms incrementally elastic at each time step. The maximum error in equivalent stress is 6.6 % for the ROVME method and 4.5% for the VME method.

The stress contours of the reference, VME and ROVME models are shown in Fig. 4.13. The

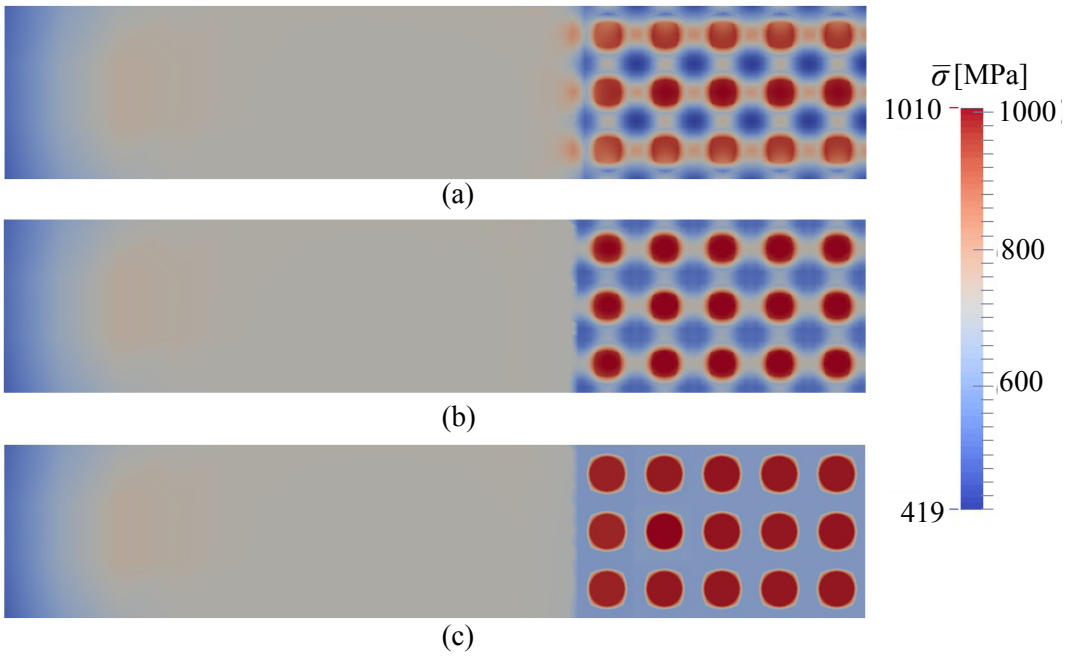

Figure 4.13: Equivalent stress contours of the specimen with pressure: (a) finite element model; (b) direct VME model; and (c) ROVME model.

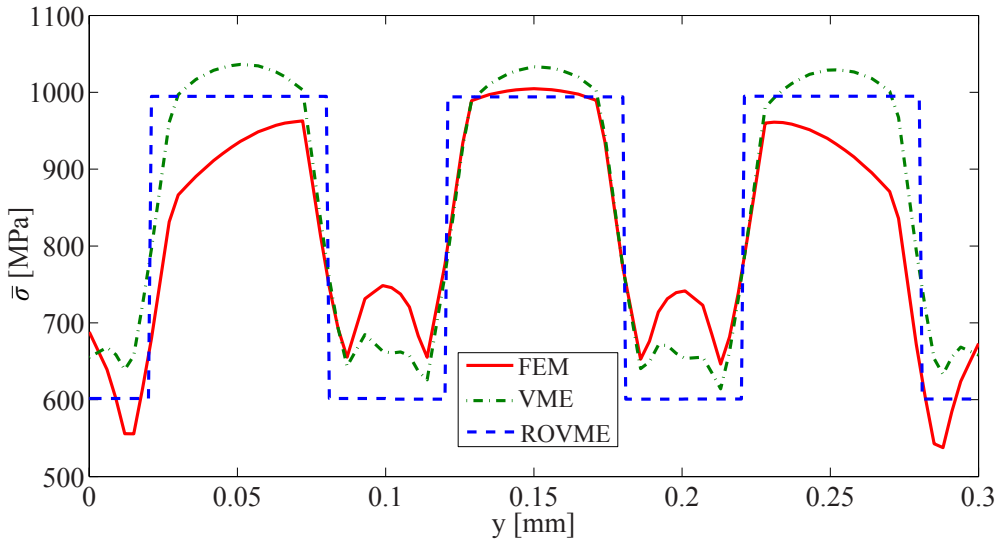

Figure 4.14: Equivalent stresses over a line (x=1.35 mm, y=0-0.3 mm) on the specimen with pressure.

stress contours of the VME and ROVME approaches are in close agreement with the stress distribution predicted by the reference model. The stress contours are relatively uniform since the pressure load dominates the deformation. The equivalent stress over a line in the enrichment region (x = 1.35 mm, y= 0 - 0.3 mm in Fig. 4.5(a) and (b)) is plotted for all of the models in Fig. 4.14.

The stress variation observed between two neighboring inclusions in the FEM approaches are not well captured with the ROVME model, as shown in Fig. 4.14. This is attributed to the fact that the ROVME model only includes weak interactions between neighboring enrichment domains through the macroscopic equilibrium. The homogeneous Dirichlet boundary conditions employed along the enrichment domain boundaries limit the strong interactions between the neighboring enrichment domains. The accuracy loss could be higher in the presence of stronger inter-enrichment domain interactions, such as in the case of composites with high inclusion volume fractions. Incorporation of more accurate boundary conditions (e.g., mixed boundary conditions proposed in Refs. [23, 24]) could improve the accuracy between two inclusions.

The accuracy of the proposed model is consistent with the previous example in Section 4.6.1, and demonstrates that both VME and ROVME methods have the capability of accurately capturing the response of structures subjected to combined thermo-mechanical loads. The computational cost for the ROVME simulation is 8.1 minutes while for the finite element simulation is 164.3 minutes. The ROVME model is 20.3 times faster than FEM for this specimen.

The accuracy and efficiency characteristic of the ROVME model is directly related to the model order, NP_α. For instance, Ref. [39] demonstrated that the accuracy could be improved with some loss of efficiency by increasing the model order. We also note that the computational efficiency of the ROVME model is expected to scale with the problem size (i.e., as the number of the enrichment domains within the problem domain increases), as the ratio of the degrees of freedom in the ROVME and direct FEM approaches (as well as the VME approach) increases with the problem size.

Table 4.2: Materials parameters for zirconia and aluminum of the composite beam

Zirconia	E [GPa]	ν	k [W/mK]	α^T [1×10^{-6}/^{o}C]
	151	0.3	2.09	10.0
Aluminum	E [GPa]	ν	k [W/mK]	α^T [1×10^{-6}/^{o}C]
	70	0.3	204	23
	A [MPa]	B [MPa]	m	n
	517	405	0.41	1.1

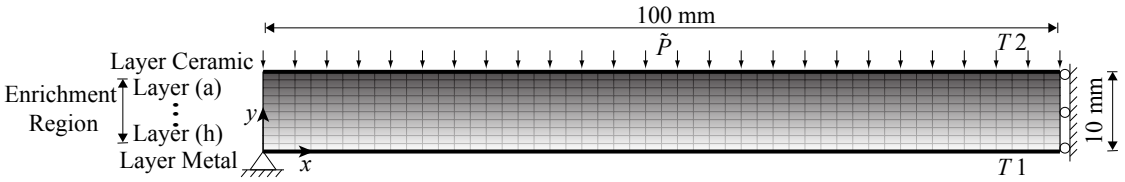

Figure 4.15: Model sketch and the ROVME macroscale discretization of a functionally graded composite beam under thermo-mechanical loads.

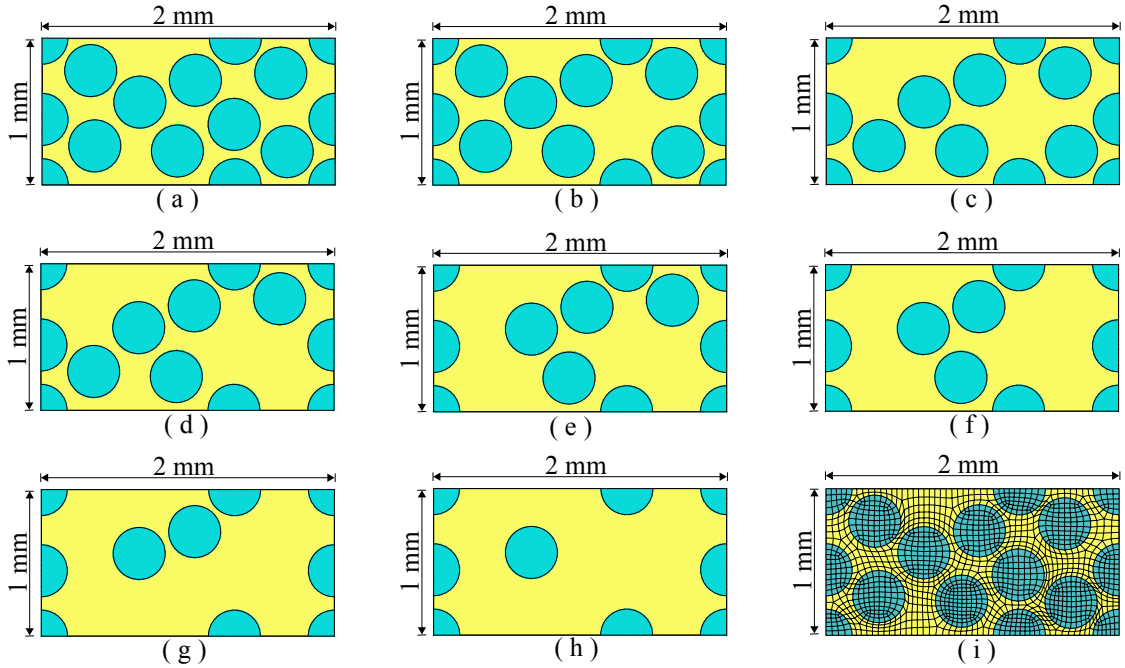

Figure 4.16: Microscale problems of the ROVME method for layer (a) to layer (h); and (i) microscale discretization for the coefficient tensors computation of layer (a).

4.7 Functionally Graded Beam

The capabilities of the ROVME approach is further demonstrated by the analysis of a functionally graded composite beam subjected to combined thermo-mechanical loading. The present study builds on the thermo-elastic analysis of functionally graded composites performed by Refs. [90, 91] and extends the analysis to investigate the behavior of the composite within the plastic regime.

A 2-D, simply supported plane-strain functionally graded beam with length, $a = 200$ mm, and thickness, $t = 10$ mm is considered. The zirconia-aluminum composite is idealized as metal matrix reinforced with randomly positioned ceramic inclusions of circular cross section. The geometry and the boundary conditions are shown in Fig. 4.15. Due to symmetry, only half of the beam is modeled. The temperatures at the bottom and top edges of the beam, $T1$ and $T2$, are set to 23$^{\text{o}}$C and 300$^{\text{o}}$C, respectively. A uniform pressure q_0 is applied on the top of the beam.

The beam is discretized into 500 macroscale quadrilateral finite elements and 561 nodes. The enrichment region is set as the entire domain. The enrichment domains employed are shown in Fig. 4.16. The top layer of the beam consists of pure zirconia ceramic material and the bottom layer is pure aluminum metal material. From the top to the bottom of the enrichment region (denoted as layer (a) to layer (h) in Fig. 4.15), the volume fraction of the ceramic in the composite decreases from 55% in layer (a) to 20% in layer (h). The radius of each inclusion is 178.4 μm. The ceramic inclusions remain elastic throughout loading, whereas the metal matrix exhibit inelastic deformations. The Young's moduli of both materials are taken as temperature independent. The material properties for zirconia and aluminum are summarized in Table 4.2. The room temperature, T_{room}, for both of the materials is set to 23$^{\text{o}}$C and the melting temperature, T_{melt}, for aluminum is set to 502$^{\text{o}}$C.

For each of the enrichment domains, a two-part reduced order model is considered. The domains of the parts correspond to the matrix and the inclusion phases. Figure 4.16(i) shows the microscale mesh employed in pre-processing to compute the coefficient tensors for enrichment domain in layer (a). Similar meshes were used for the other layers. For the purpose of comparison, the reference predictions of two specimens, made of pure aluminum and pure zirconia,

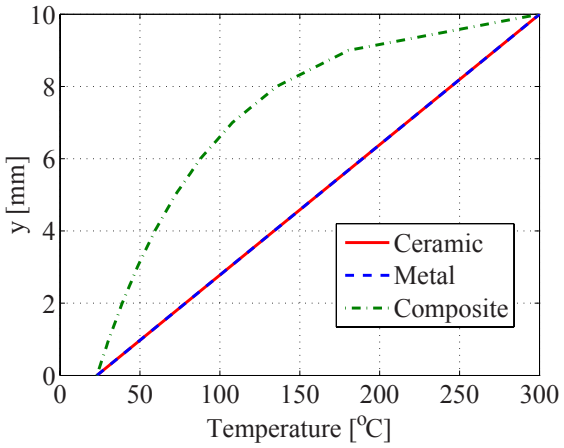

Figure 4.17: Temperature variations along the thickness of the beam.

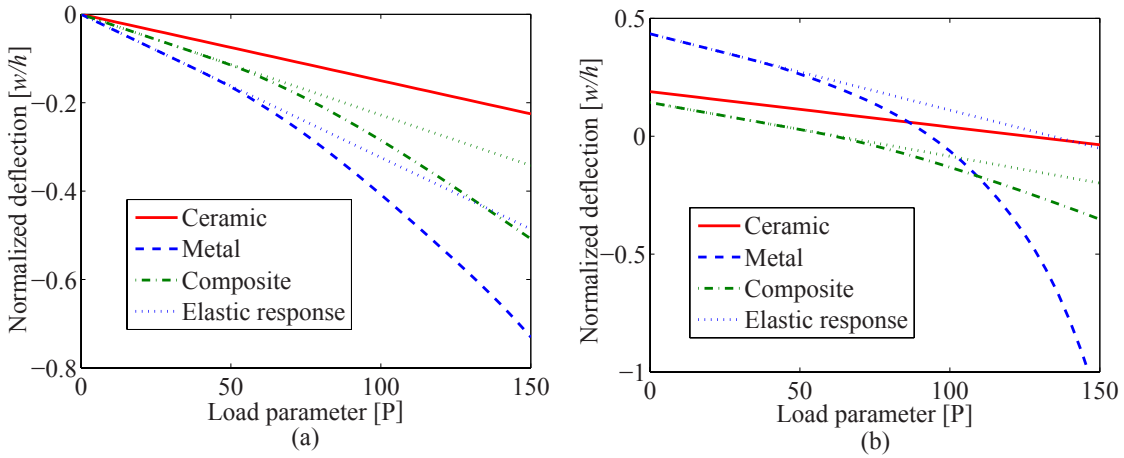

Figure 4.18: Non-dimensional center deflections along with load parameter for beam under: (a) mechanical loading; and (b) thermo-mechanical loading.

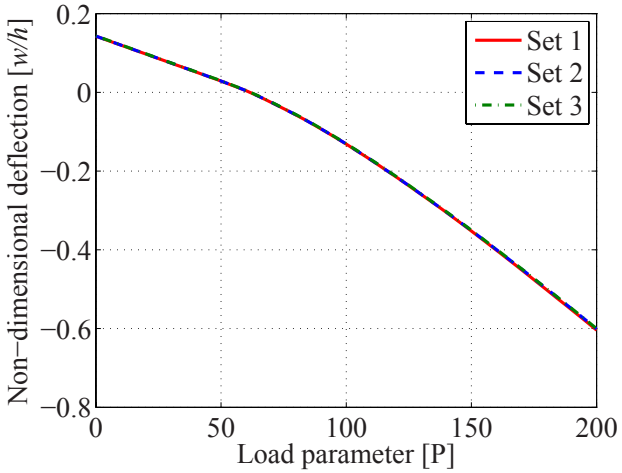

Figure 4.19: Non-dimensional center deflections along with load parameter for beams using different sets of microstructures.

are performed using the finite element method, respectively. Figure 4.17 shows the steady state distribution of temperature under the prescribed boundary conditions for the monolithic materials and the functionally graded composite. The spatially varying conductivity of the composite beam results in non-linear variation of the temperature field through the thickness. The steady state temperatures within the composite are lower than those in monolithic materials.

Figure 4.18 presents the normalized deflection, w/h, where w is the deflection of the center of the beam as a function of the normalized load parameter, $P = (q_0\, a^4)/(E_m\, h^4)$. E_m is the Young's modulus of the metal material and q_0 is taken as 0.01 MPa. Figure 4.18(a) corresponds to the pure mechanical loading at the room temperature, whereas Fig. 4.18(b) includes the effect of thermal gradients. In both figures, the dotted lines indicate the responses under the assumption of elastic behavior for both constituents. In the pure mechanical loading, the normalized deflection of the composite beam lies between those of the pure ceramic and pure metal specimens, under both elastic and inelastic material behavior assumptions. The results in Fig. 4.18(b) include the effect of thermal expansions induced by the temperature gradient over the specimen. In the presence of thermo-mechanical loading, the deflection of the composite beam is lower than both ceramic and metal beams when subjected to moderate mechanical load, under both elastic and inelastic material assumptions. This observation is consistent with those in Refs. [90, 91]. As the load increases, the deflection in the pure metal beam significantly increases due to rapid accumulation of plastic deformation. In contrast, the presence of the ceramic inclusion reduces the amount of plastic flow in the composite specimen, and the rate of deflection remains contained compared with the pure metal specimen.

In order to ensure that the results shown are independent of the microstructural morphology, the thermo-mechanical simulation discussed above is repeated by three separate sets of randomly generated microstructures for each layer of the composite. Figure 4.19 shows that the overall deflection of the composite is not significantly affected by the microstructural morphology, as long as the volume fraction distribution is maintained.

Chapter 5

HYBRID INTEGRATION FOR REDUCED ORDER VARIATIONAL MULTISCALE ENRICHMENT METHOD

5.1 Introduction

Using the reduced order variational multiscale enrichment (ROVME) method provided in the previous chapters to address surface degradation problems would require tremendous amounts of enrichment domains, since the sizes of the microstructures are at the level of microns while of the surface region are in inches. It could be computational prohibitive for the ROVME method to model such problems. The current chapter presents the formulation and implementation of a hybrid multiscale integration scheme for problems that exhibit different scale separation characteristics in various directions. The proposed approach employs the key ideas of the variational multiscale enrichment at directions that exhibit poor scale separation, and the computational homogenization at directions with good scale separability. The formulation is based on the variational multiscale principles and develops a novel integration scheme that takes advantage of homogenization-like integration along directions that exhibit scale separation. The proposed integration scheme is also integrated with the reduced order variational multiscale enrichment in order to achieve a computationally efficient multiscale solution strategy for surface degradation problems. A suite of numerical verifications is performed to verify the implementation of the proposed multiscale scheme. The results of the verification studies indicate that the approach further improves the efficiency of the ROVME simulations, without significant compromise on accuracy. A coupled transport-thermo-mechanical analysis is presented to demonstrate the capability of the proposed computational framework.

The remainder of the chapter is organized as follows: Section 5.2 provides the variational multiscale enrichment setting for directionally scale separable problems. The hybrid multiscale integration scheme is described in Section 5.3. Section 5.4 details the formulation and implemen-

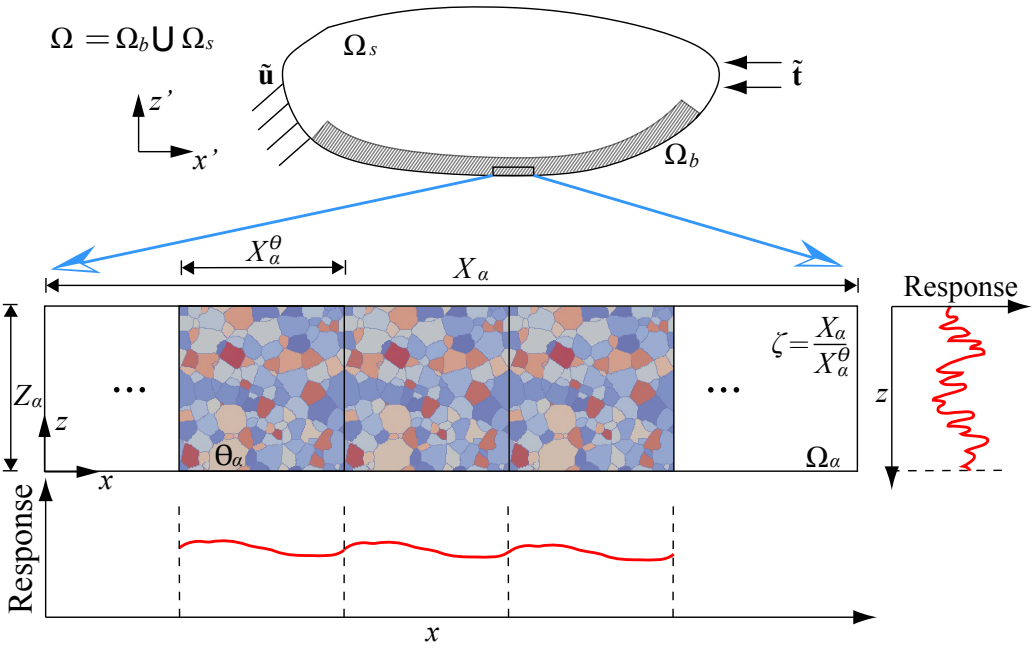

Figure 5.1: Domain decomposition for directionally scale separable problems

tation of the hybrid integration for ROVME method. Section 5.5 presents the application of the hybrid multiscale integration to the ROVME method. Numerical verifications are presented in Section 5.6. A coupled transport-thermo-mechanical problem with surface degradation is presented in Section 5.7 to demonstrate the capability of the proposed computational framework.

5.2 Variational multiscale enrichment setting for directionally scale separable problems

The proposed multiscale approach generalizes and builds on the variational multiscale enrichment idea introduced in Refs. [24, 39, 86]. Consider an open, bounded domain $\Omega \subset \mathbb{R}^2$ that constitutes the domain of the macroscopic structure and the domain decompositions defined in Eqs. (2.11) and (2.12). Rather than defining the coordinate system of the enrichment domains identical to the global coordinate system as the previous chapters, these two systems are defined separately in the current chapter. The global coordinate system is denoted by $\mathbf{x}' = (x', z')$, as shown in Fig. 5.1. Under the applied loading and environmental conditions, the structure undergoes significant localized deformation within a characteristic subdomain, $\Omega_b \in \Omega$, whereas within the re-

mainder of the domain, $\Omega_s \equiv \Omega \backslash \Omega_b$, the response does not localize. We are therefore concerned with accurately and efficiently capturing response fields within Ω_b (i.e., the enrichment region). In surface degradation problems, the enrichment region spans the boundaries of the structure exposed to aggressive environmental agents but extends to a very limited depth compared to the overall structural thickness as illustrated in Fig. 5.1. The enrichment region is further discretized into a series of non-overlapping enrichment domains as shown in Eq. (2.12). The enrichment domain, Ω_α is formed by the repetition of a heterogeneous microstructure, Θ_α along the local direction, $x(\mathbf{x}')$ and the size of the microstructure is taken to be small compared to the dimension of the macroscopic domain along the *homogenizable* direction, x. In contrast, the dimension of the enrichment domain in the transverse direction $z(\mathbf{x}')$ is identical to that of the microstructure. The ratio between the size of the microstructure domain and the enrichment domain is denoted by a small positive scaling constant, ζ defined as:

$$\zeta = \frac{X_\alpha^\theta}{X_\alpha} \to 0 \tag{5.1}$$

in which, X_α^θ and X_α are the sizes of Θ_α and Ω_α in the x-direction. The response within the enrichment domain along x rapidly oscillates in space due to the fluctuations in the material properties within the microstructure. The response fields are therefore considered to be functions of the macroscale coordinate system, x, as well as a microscale coordinate system, $\breve{x} = x/\zeta$, which is a stretched position vector.

The problem setting described above indicates *directional homogenization* of the response fields; i.e., the response fields are scale separable at prescribed directions, whereas they are taken to be scale inseparable at other directions. We therefore seek to employ the computational homogenization principles along the scale separable directions, whereas employ the variational multiscale setting along the scale inseparable direction. Within this problem setting, an arbitrary response field in an enrichment domain is expressed as:

$$f^\zeta(\mathbf{x}) = f(x, \breve{x}(x), z) \tag{5.2}$$

Where, f^{ζ} denotes the response field expressed in the original coordinate system, and superscript ζ indicates that the field is oscillatory in the scale separable direction.

We start by considering the following additive decomposition of the deformation field [1, 2, 24] within an arbitrary enrichment domain, Ω_α:

$$\mathbf{u}(x,\breve{x},z,t) = \mathbf{u}^M(x,z,t) + \mathbf{u}^m_\alpha(x,\breve{x},z,t) \tag{5.3}$$

where, $\mathbf{u}^M \in \mathscr{V}^M(\Omega)$ and $\mathbf{u}^m_\alpha \in \mathscr{V}_\alpha(\Omega_\alpha)$ are respectively the macroscale and microscale displacement fields; and $\mathscr{V}^M$ and $\mathscr{V}_\alpha$ denote the trial (discretized) spaces for the macro- and microscale fields, respectively:

$$\mathscr{V}^M(\Omega) \equiv \left\{ \mathbf{u}^M\left[x(\mathbf{x}'),z(\mathbf{x}'),t\right] \,\middle|\, \mathbf{u}^M = \sum_{A=1}^{N_D^\alpha} N_A(x',z')\,\hat{\mathbf{u}}^M_A(t); \right. \\ \left. \hat{\mathbf{u}}^M_A = \tilde{\mathbf{u}}(x'_A,z'_A,t) \text{ if } (x'_A,z'_A) \in \Gamma^u \right\} \tag{5.4}$$

$$\mathscr{V}_\alpha(\Omega_\alpha) \equiv \left\{ \mathbf{u}^m_\alpha(x,\breve{x},z,t) \,\middle|\, \mathbf{u}^m_\alpha = \sum_{a=1}^{n_{d\alpha}} n_{\alpha,a}(x,\breve{x},z)\,\hat{\mathbf{u}}^m_{\alpha,a}(t);\ \hat{\mathbf{u}}^m_{\alpha,a} = 0 \text{ if } (x_\alpha,z_\alpha) \in \Gamma^u_\alpha \right\} \tag{5.5}$$

In the verification studies described later, a viscoplastic constitutive relationship has been employed for the material constituents. The enrichment domains are taken to be geometrically simple such that it is represented by a single finite element in the macroscopic grid. Homogeneous Dirichlet boundary conditions are employed along the enrichment domain boundaries to ensure displacement continuity across the enrichment domains [64]. The function fields are directly provided as discrete approximations and the formalism regarding the specialization from the continuum to discretized fields are skipped for brevity. It is important to note that the additive decomposition provided in Eq. (5.3) is admissible due to the direct sum decomposition property of the corresponding fine and coarse scale approximation spaces [1].

Following a similar decomposition to Eq. (5.3), the test function field is additively decomposed into macroscale ($\mathbf{w}^M$) and microscale ($\mathbf{w}^m_\alpha$) counterparts. Substituting the test and trial function de-

compositions into the governing equilibrium equations, and splitting the governing equations based on the micro- and macroscopic counterparts result in a coupled system of macro- and microscale problems in the variational setting. The macroscale problem in the weak form yields:

$$\textbf{Macroscale Problem:} \quad \int_{\Omega_s} \nabla \mathbf{w}^M(x',z') : \boldsymbol{\sigma}(x',z',t)\, d\Omega + \sum_{\alpha=1}^{n_{\text{en}}} \int_{\Omega_\alpha} \nabla \mathbf{w}^M(x,z) : \boldsymbol{\sigma}(x,\breve{x},z,t)\, d\Omega - \int_{\Gamma^t} \mathbf{w}^M(x',z') \cdot \tilde{\mathbf{t}}(x',z')\, d\Gamma = 0 \quad (5.6)$$

where, $\tilde{\mathbf{t}}$ is the prescribed traction along the Neumann boundary (Γ^t). The prescribed tractions are assumed to vary with the macroscopic coordinates only. The stress field is taken to be a local, history-dependent, nonlinear function of the strain and other internal state variables. Within each enrichment domain, the integration in Eq. (5.6) is expressed in the corresponding local coordinate system. Within the substrate region, the response is assumed to be unaffected by the material heterogeneity and accurately approximated by the macroscale response fields alone. The weak form of the microscale problem at an arbitrary enrichment domain, Ω_α, is:

$$\textbf{Microscale Problem:} \quad \int_{\Omega_\alpha} \nabla \mathbf{w}^m_\alpha(x,\breve{x},z) : \boldsymbol{\sigma}(x,\breve{x},z,t)\, d\Omega = 0; \quad \alpha = 1,2,...n_{\text{en}} \quad (5.7)$$

The microscale problems defined over each enrichment domain within the structure is tightly coupled to the macroscale problem. The coupling is through the stress terms in the respective equations which are functions of the total strain field that depends on the fine and coarse scale components of the displacement field. In the context of VME, the micro- and macroscale problems are evaluated in a coupled and iterative manner.

The evaluation of the coupled multiscale problem defined above is computationally expensive due to the complexity of the integral terms of the coarse and fine scale problems defined over the enrichment domains. The complexity is two-fold: (1) the microstructure is highly heterogeneous and exhibit highly nonlinear response that requires the evaluation of a large number of nonlinear enrichment domain problems in an iterative setting; and (2) within each enrichment domain, a large

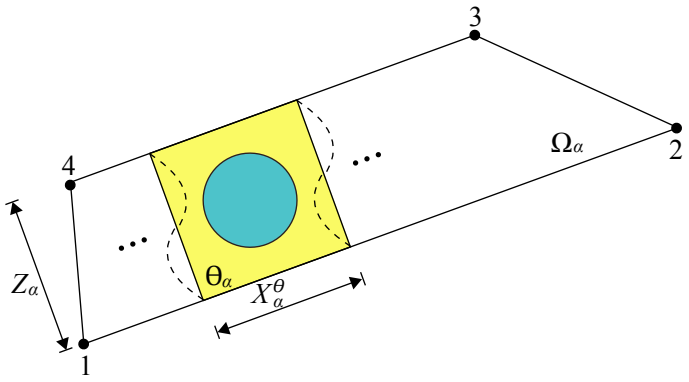

Figure 5.2: A macroscale enrichment domain for hybrid multiscale integration.

number of microstructures exist, over which the integrations must be performed. The latter difficulty was addressed through the development of the reduced order VME approach in Ref. [39]. In the current chapter, we focus on developing a hybrid integration scheme in order to take advantage of the scale separability in select directions, and combining the hybrid integration scheme with the reduced order microstructure representation.

5.3 Hybrid Multiscale Integrator

Let the enrichment domain, Ω_α coincide with an element of the macroscale discretization within the enrichment region. The shape of the enrichment domain is constrained due to the directional scale separation condition: (1) considering a microstructure with an aspect ratio of O(1), the aspect ratio of the enrichment domain is taken to be high; and (2) the element length in the scale inseparable direction is taken to be constant and equal to the edge length of the microstructure along the same direction. Define vectors $\mathbf{v}_{ij} = \mathbf{x}'_j - \mathbf{x}'_i = (x'_j, z'_j) - (x'_i, z'_i);\ i, j = 1,2,3,4;\ i \neq j$ within the enrichment domain. Denoting the size of the microstructure in the scale inseparable direction as X_α^θ and in the scale separable direction as Z_α^θ, the above-mentioned constraints are imposed as follows:

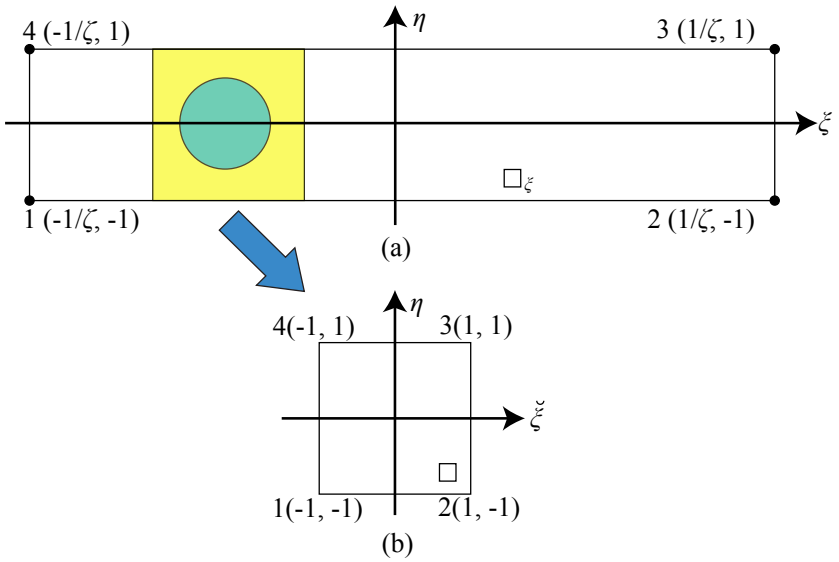

Figure 5.3: Canonical systems of the hybrid integration for: (a) the enrichment domain and (b) the microstructure of the enrichment domain.

(i) $\mathbf{v}_{12}//\mathbf{v}_{34}$ (i.e., $|(\mathbf{v}_{12}\cdot\mathbf{v}_{34})/(||\mathbf{v}_{12}||\ ||\mathbf{v}_{34}||)|=1$), and;

$$\zeta=\frac{2X_\alpha^\theta}{\parallel \mathbf{v}_{12}\parallel+\parallel \mathbf{v}_{34}\parallel}\rightarrow 0;\quad Z_\alpha^\theta=Z_\alpha\equiv\parallel \mathbf{v}_{23}\cdot\mathbf{v}_n\parallel \tag{5.8}$$

where $\mathbf{v}_n\perp\mathbf{v}_{12}$ and $\mathbf{v}_n$ is a unit vector, or;

(ii) $\mathbf{v}_{23}//\mathbf{v}_{41}$ (i.e., $|(\mathbf{v}_{23}\cdot\mathbf{v}_{41})/(||\mathbf{v}_{23}||\ ||\mathbf{v}_{41}||)|=1$), and;

$$\zeta=\frac{2X_\alpha^\theta}{\parallel \mathbf{v}_{23}\parallel+\parallel \mathbf{v}_{41}\parallel}\rightarrow 0;\quad Z_\alpha^\theta=Z_\alpha\equiv\parallel \mathbf{v}_{12}\cdot\mathbf{v}_n\parallel;\quad \mathbf{v}_n\perp\mathbf{v}_{23} \tag{5.9}$$

When (i) or (ii) is satisfied, such as in the example shown in Fig. 5.2, the enrichment domain is scale separable, and the hybrid multiscale integration scheme described below is applicable.

5.3.1 Canonical coordinate systems

In context of standard finite element coordinate system transformation, the macroscale problem for an enrichment domain is first transfered from the global coordinate system ($\mathbf{x}'$) to a standard

canonical system ($\boldsymbol{\xi}$). Then, the response discretization in Eq. (5.4) is performed using the standard shape functions in the canonical system. In the current setting, a new set of canonical systems, as illustrated in Fig. 5.3, and the associated shape functions are employed. The canonical system of the enrichment domain, Ω_α, is denoted as $\square_\xi$ with the associated limits as $\xi \in [-1/\zeta, 1/\zeta]$ and $\eta \in [-1,1]$. Embedded in the enrichment domain, $\square$ denotes the canonical system for the microstructure, Θ_α, which resolves the microstructural material heterogeneity, as shown in Fig. 5.3 for the example presented in Fig. 5.2. Its limits are $\breve{\xi} \in [-1,1]$ and $\eta \in [-1,1]$. The two systems have separate coordinates in the scale separable ξ-direction, but share the same coordinate in the η-direction. Other than containing the resolved microstructural topology, $\square$ is identical to the standard canonical system and the standard shape functions are employed. New shape functions are defined for $\square_\xi$ as:

$$\begin{aligned} N_1(\xi,\eta;\zeta) &= \frac{(1-\zeta\ \xi)(1-\eta)}{4}; \quad N_2(\xi,\eta;\zeta) = \frac{(1+\zeta\ \xi)(1-\eta)}{4} \\ N_3(\xi,\eta;\zeta) &= \frac{(1+\zeta\ \xi)(1+\eta)}{4}; \quad N_4(\xi,\eta;\zeta) = \frac{(1-\zeta\ \xi)(1+\eta)}{4} \end{aligned} \tag{5.10}$$

The hybrid integrations for the micro- and macroscale problems over the enrichment domains are performed by considering the canonical systems in Fig. 5.3 and their shape functions

5.3.2 Integration of Macroscale and microscale problems

We first demonstrate the proposed hybrid multiscale integration over a scalar function, ψ. The integration scheme is then applied to the enrichment domain integrals that appear in the microscale and macroscale problems. Let ψ be sufficiently smooth and integrable function over the enrichment domain. The function is assumed to be periodic along the homogenizable direction, x. Considering coordinate transformation and the homogenization concept in the ξ-direction as

$\zeta \to 0$ [26], the integration of ψ over Ω_α is expressed as follows:

$$\begin{aligned}\lim_{\zeta\to 0}\int_{\Omega_\alpha}\psi(x,\breve{x}=\frac{x}{\zeta},z)\,d\Omega &= \lim_{\zeta\to 0}\int_{-1}^{1}\int_{-\frac{1}{\zeta}}^{\frac{1}{\zeta}}\psi(\xi,\breve{\xi},\eta)\,\mathrm{det}J(\xi,\eta)\,d\xi\,d\eta \\ &= \int_{-1}^{1}\int_{-\frac{1}{\zeta}}^{\frac{1}{\zeta}}\bar{\psi}(\xi,\eta)\,\mathrm{det}J(\xi,\eta)\,d\xi\,d\eta\end{aligned} \tag{5.11}$$

where, $J(\xi,\eta)$ is the Jacobian matrix for the coordinate transformation, det$(\cdot)$ denote the determinant, and $\bar{\psi}$ is the microstructure-average (i.e., homogenized) function along the homogenizable direction which is defined as:

$$\bar{\psi}(\xi,\eta)=\frac{1}{2}\int_{-1}^{1}\psi(\xi,\breve{\xi},\eta)\,d\breve{\xi} \tag{5.12}$$

The integration shown in Eq. (5.11) at the homogenization limit exists and convergent (assuming the standard continuity and periodicity requirements for ψ), since it is identical to the weak convergence argument of the mathematical homogenization theory [92, 93] - but only applied to a single direction. Employing the one-dimensional Gaussian quadrature rule and approximating the integration of the homogenized response ($\bar{\psi}$) in the ξ-direction with *ng* integration points:

$$\int_{-\frac{1}{\zeta}}^{\frac{1}{\zeta}}\bar{\psi}(\xi,\eta)\,\mathrm{det}J(\xi,\eta)\,d\xi \approx \sum_{g=1}^{ng}\bar{\psi}(\xi_g,\eta)\,\mathrm{det}J(\xi_g,\eta)\,\mathscr{W}_g;\ \text{ and } g=1,2,...,ng \tag{5.13}$$

where, $\xi_g=\bar{\xi}_g/\zeta$ indicates the position of the Gaussian quadrature point in the ξ-direction and $\mathscr{W}_g=\bar{\mathscr{W}}_g/\zeta$ is the corresponding weight. $\bar{\xi}_g$ and $\bar{\mathscr{W}}_g$ are the positions and weights of the standard Gaussian quadrature points for $\xi\in[-1,1]$, respectively. Substituting Eq. (5.13) into Eq. (5.11), the integration over the enrichment domain is approximated as:

$$\lim_{\zeta\to 0}\int_{\Omega_\alpha}\psi(x,\breve{x}=\frac{x}{\zeta},z)\,d\Omega \approx \sum_{g=1}^{ng}\int_{-1}^{1}\bar{\psi}(\xi_g,\eta)\,\mathrm{det}J(\xi_g,\eta)\,d\eta\,\mathscr{W}_g \tag{5.14}$$

Considering Eq. (5.12) and defining $\int_{\square} f(\xi_g,\breve{\xi},\eta)\, d\breve{\Omega} \equiv \int_{-1}^{1}\int_{-1}^{1} f(\xi_g,\breve{\xi},\eta)\, d\breve{\xi} d\eta$, the hybrid integration over an enrichment domain yields:

$$\lim_{\zeta\to 0}\int_{\Omega_\alpha} \psi(x,\breve{x}=\frac{x}{\zeta},z)\, d\Omega \approx \sum_{g=1}^{ng} \frac{\mathscr{W}_g}{2}\int_{\square} \psi(\xi_g,\breve{\xi},\eta)\, \mathrm{det}J(\xi_g,\eta)\, d\breve{\Omega} \tag{5.15}$$

Equation (5.15) is the general hybrid integration rule which can be applied to any integrable function over an enrichment domain in directionally scale separable problems.

Applying the hybrid multiscale integration approach to the integration over an arbitrary enrichment domain of the macroscale problem yields the following expression:

$$\begin{aligned}\lim_{\zeta\to 0}\int_{\Omega_\alpha} &\nabla \mathbf{w}^M(x,z) : \boldsymbol{\sigma}(x,\breve{x},z,t)\, d\Omega \\ &\approx \sum_{g=1}^{ng} \frac{\mathscr{W}_{\alpha g}}{2}\int_{\square} \nabla \mathbf{w}^M(\xi_{\alpha g},\eta) : \boldsymbol{\sigma}(\xi_{\alpha g},\breve{\xi},\eta,t)\, \mathrm{det}J(\xi_{\alpha g},\eta)\, d\breve{\Omega}\end{aligned} \tag{5.16}$$

where, $\xi_{\alpha g}$ and $\mathscr{W}_{\alpha g}$ are the positions and associated weights for the enrichment domain, Ω_α. Similarly, the microscale weak form for the enrichment domain Ω_α (Eq. (5.7)) is obtained as:

$$\begin{aligned}\lim_{\zeta\to 0}\int_{\Omega_\alpha} &\nabla \mathbf{w}^m_\alpha(x,\breve{x},z) : \boldsymbol{\sigma}(x,\breve{x},z,t)\, d\Omega \\ &\approx \sum_{g=1}^{ng} \frac{\mathscr{W}_{\alpha g}}{2}\int_{\square} \nabla \mathbf{w}^m_\alpha(\xi_{\alpha g},\breve{\xi},\eta) : \boldsymbol{\sigma}(\xi_{\alpha g},\breve{\xi},\eta,t)\, \mathrm{det}J(\xi_{\alpha g},\eta)\, d\breve{\Omega} = 0\end{aligned} \tag{5.17}$$

Since $\mathscr{W}_{\alpha g}$ does not depend on $\breve{\xi}$ or η, a solution that ensures the equilibrium of the microscale state (Eq. (5.17)) is:

$$\int_{\square} \nabla \mathbf{w}^m_\alpha(\xi_{\alpha g},\breve{\xi},\eta) : \boldsymbol{\sigma}(\xi_{\alpha g},\breve{\xi},\eta,t)\, \mathrm{det}J(\xi_{\alpha g},\eta)\, d\breve{\Omega} = 0; \quad \forall g = 1,2,...,ng \tag{5.18}$$

Equation (5.18) implies that under the condition of directional scale-separability, enforcement of equilibrium at the scale of the microstructure associated with each quadrature point implies the microscale equilibrium within the enrichment domain. The application of the hybrid multiscale integration to the micro- and macroscale problems requires that the fine scale components of the

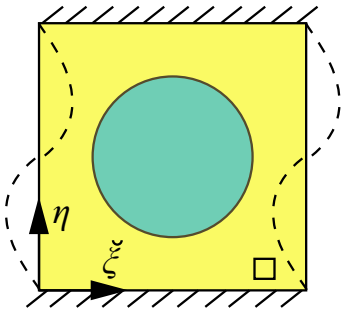

Figure 5.4: Boundary conditions for the microstructures.

response fields over the microstructure are periodic along the η-direction. In order to ensure continuity across neighboring enrichment domains or along the boundaries between the enrichment domains and the substrate [2, 24], homogeneous Dirichlet boundary conditions are prescribed for microstructure boundaries along the $\tilde{\xi}$-direction, as illustrated in Fig. 5.4.

5.4 Hybrid Integration for Reduced Order Variational Multiscale Enrichment (HROVME)

In this section, we describe the application of the proposed hybrid multiscale integration approach to the reduced order variational multiscale enrichment (ROVME) method for inelastic problems. The ROVME method, recently proposed by the authors [39, 86], approximates the nonlinear heterogeneous response within the enrichment domain using a reduced approximation basis to enhance the computational efficiency. ROVME is applicable when the microstructure domain and the enrichment domain coincides (i.e., when ζ=1). By applying the proposed hybrid multiscale integrator to ROVME (referred to as HROVME in what follows), we aim to address directionally scale separable problems (i.e., when $\zeta = 0$) in an efficient manner.

5.4.1 The microscale problem

The microscale problem as stated in Eq. (5.18) is numerically evaluated through ROVME. Considering Eq. (5.3) and the canonical systems of the hybrid multiscale integration, the constitutive

equation at a fixed $\xi_{\alpha g}$ is expressed as:

$$\boldsymbol{\sigma}(\xi_{\alpha g},\breve{\xi},\eta,t)=\mathbf{L}^{\alpha}(\breve{\xi},\eta):\Big[\nabla\mathbf{u}^{M}(\xi_{\alpha g},\eta,t)+\nabla\mathbf{u}^{m}_{\alpha}(\xi_{\alpha g},\breve{\xi},\eta,t)-\boldsymbol{\varepsilon}^{vp}(\xi_{\alpha g},\breve{\xi},\eta,t)\Big] \tag{5.19}$$

where, $\mathbf{L}^{\alpha}$ is the tensor of elastic moduli which varies spatially within the microstructure; $\boldsymbol{\varepsilon}^{vp}$ denote the viscoplastic strain. By this expression, the additive split of the total strain tensor to elastic and inelastic counterparts is assumed for the constitutive laws of the material constituents. Employing the ROVME idea [39, 86], the microscale displacement field is expressed as:

$$\mathbf{u}^{m}_{\alpha}(\xi_{\alpha g},\breve{\xi},\eta,t)=\sum_{A=1}^{N^{\alpha}_{D}}\mathbf{H}^{\alpha g}_{A}(\breve{\xi},\eta,\zeta)\cdot\hat{\mathbf{u}}^{M\alpha}_{A}(t)+\int_{\square}\mathbf{h}^{\alpha}(\breve{\xi},\eta,\hat{\xi},\hat{\eta}):\boldsymbol{\varepsilon}^{vp}(\xi_{\alpha g},\hat{\xi},\hat{\eta},t)\,d\hat{\Omega} \tag{5.20}$$

where, $\hat{\Omega}=(\hat{\xi},\hat{\eta})\in\square$; N^{α}_{D} is the number of nodes of the macroscale element associated with the enrichment domain; $\mathbf{H}^{\alpha g}_{A}$ is the elastic influence function associated with the g^{th} integration point of the enrichment domain; and $\mathbf{h}^{\alpha}$ is the inelastic influence function induced by the inelastic behavior within the microstructure. The influence functions are approximations to Green's function problems defined over the microstructure, and evaluated numerically. With a slight deviation from the ROVME approach, the influence functions are evaluated by considering the semi-periodic boundary conditions described above. Considering element level discretization of the macroscale displacement field through the ζ-dependent shape functions in Eq. (5.10):

$$\mathbf{u}^{M}(\xi_{\alpha g},\eta,t)=\sum_{A=1}^{N^{\alpha}_{D}}N_{A}(\xi_{\alpha g},\eta,\zeta,t)\;\hat{\mathbf{u}}^{M\alpha}_{A}(t) \tag{5.21}$$

and, substituting the constitutive equation (Eq. (5.19)), macro- and microscale displacement discretizations (Eqs. (5.20) and (5.21)) into Eq. (5.18), the microscale problem in weak form yields:

$$\sum_{A=1}^{N_D^\alpha}\Bigg[\int_{\square}\nabla\mathbf{w}^m_{\alpha g}(\breve{\xi},\eta):\mathbf{L}^\alpha(\breve{\xi},\eta)\cdot\nabla N_A(\xi_{\alpha g},\eta,\zeta)\,\det J(\xi_{\alpha g},\eta)\,d\breve{\Omega}$$
$$+\int_{\square}\nabla\mathbf{w}^m_{\alpha g}(\breve{\xi},\eta):\mathbf{L}^\alpha(\breve{\xi},\eta):\nabla\mathbf{H}^{\alpha g}_A(\breve{\xi},\eta,\zeta)\,\det J(\xi_{\alpha g},\eta)\,d\breve{\Omega}\Bigg]\cdot\hat{\mathbf{u}}^{M\alpha}_A(t)$$
$$+\int_{\square}\nabla\mathbf{w}^m_{\alpha g}(\breve{\xi},\eta):\mathbf{L}^\alpha(\breve{\xi},\eta):\Bigg[\int_{\square}\nabla\mathbf{h}^\alpha(\breve{\xi},\eta,\hat{\xi},\hat{\eta}):\varepsilon^{vp}(\xi_{\alpha g},\hat{\xi},\hat{\eta},t)\,d\hat{\Omega}$$
$$-\varepsilon^{vp}(\xi_{\alpha g},\breve{\xi},\eta,t)\Bigg]\det J(\xi_{\alpha g},\eta)\,d\breve{\Omega}=0 \quad (5.22)$$

where, $\nabla\mathbf{w}^m_{\alpha g}(\breve{\xi},\eta)\equiv\nabla\mathbf{w}^m_{\alpha}(\xi_{\alpha g},\breve{\xi},\eta)$. Considering the case when the microstructure deforms elastically ($\varepsilon^{vp}=0$), Eq. (5.22) yields the elastic influence function problem that can be solved for $\mathbf{H}^{\alpha g}_A$:

$$\int_{\square}\nabla\mathbf{w}^m_{\alpha g}(\breve{\xi},\eta):\mathbf{L}^\alpha(\breve{\xi},\eta):\nabla\mathbf{H}^{\alpha g}_A(\breve{\xi},\eta,\zeta)\,\det J(\xi_{\alpha g},\eta)\,d\breve{\Omega}=$$
$$-\int_{\square}\nabla\mathbf{w}^m_{\alpha g}(\breve{\xi},\eta):\mathbf{L}^\alpha(\breve{\xi},\eta)\cdot\nabla N_A(\xi_{\alpha g},\eta,\zeta)\,\det J(\xi_{\alpha g},\eta)\,d\breve{\Omega};$$
$$\forall A=1,2,...,N_D^\alpha \text{ and } g=1,2,...,ng \quad (5.23)$$

Substituting Eq. (5.23) into the microscale weak form (Eq. (5.22)), results in the inelastic influence function problem for $\mathbf{h}^\alpha$:

$$\int_{\square}\nabla\mathbf{w}^m_{\alpha g}(\breve{\xi},\eta):\mathbf{L}^\alpha(\breve{\xi},\eta):\nabla\mathbf{h}^\alpha(\breve{\xi},\eta,\hat{\xi},\hat{\eta})\,\det J(\xi_{\alpha g},\eta)\,d\breve{\Omega}=$$
$$\int_{\square}\nabla\mathbf{w}^m_{\alpha g}(\breve{\xi},\eta):\mathbf{L}^\alpha(\breve{\xi},\eta)\,\delta^d(\breve{\xi}-\hat{\xi},\eta-\hat{\eta})\,\det J(\xi_{\alpha g},\eta)\,d\breve{\Omega};\ \forall(\hat{\xi},\hat{\eta})\in\square \quad (5.24)$$

in which, δ^d denotes the Dirac delta distribution. The elastic and inelastic microscale influence function problems are linear elastic problems defined over the microstructure. Therefore, the influence functions are computed off-line, prior to a macroscale analysis.

Next, a microstructure partitioning is considered to obtain a reduced order approximation to the

microscale problems [37, 39, 86]. The microstructure defined in the canonical form is decomposed into NP non-overlapping subdomains (i.e., parts):

$$\square = \bigcup_{\gamma=1}^{NP} \square_\gamma; \;\; \square_\gamma \cap \square_\lambda \equiv \emptyset \;\; \text{when} \;\; \gamma \neq \lambda \tag{5.25}$$

where $\square_\gamma$ denotes a part of the microstructure. Stress and inelastic strain fields within the microstructure are then expressed as:

$$\boldsymbol{\sigma}(\xi_{\alpha g}, \breve{\xi}, \eta, t) = \sum_{\gamma=1}^{NP} \hat{N}_\gamma(\breve{\xi}, \eta)\, \boldsymbol{\sigma}_\gamma^{\alpha g}(t); \quad \boldsymbol{\varepsilon}^{vp}(\xi_{\alpha g}, \breve{\xi}, \eta, t) = \sum_{\gamma=1}^{NP} \hat{N}_\gamma(\breve{\xi}, \eta)\, \boldsymbol{\mu}_\gamma^{\alpha g}(t) \tag{5.26}$$

where, $\hat{N}_\gamma(\breve{\xi}, \eta)$ denotes a reduced model shape function:

$$\hat{N}_\gamma(\breve{\xi}, \eta) = \begin{cases} 1, & \text{if } (\breve{\xi}, \eta) \in \square_\gamma \\ 0, & \text{elsewhere} \end{cases} \tag{5.27}$$

The stress and inelastic strain fields are therefore approximated as spatially piecewise constant fields with unknown coefficients , $\boldsymbol{\sigma}_\gamma^{\alpha g}$ and $\boldsymbol{\mu}_\gamma^{\alpha g}$, respectively. Substituting Eq. (5.26) into Eq. (5.19) and using Eq. (5.27), the constitutive equation is expressed in terms of the unknown stress and inelastic coefficients as:

$$\boldsymbol{\sigma}_\lambda^{\alpha g}(t) = \sum_{A=1}^{N_D^\alpha} \mathbf{S}_{\lambda A}^{\alpha g}(\zeta) \cdot \hat{\mathbf{u}}_A^{M\alpha}(t) + \sum_{\gamma=1}^{NP} \mathbf{P}_{\lambda\gamma}^{\alpha} : \boldsymbol{\mu}_\gamma^{\alpha g}(t) \tag{5.28}$$

where,

$$\mathbf{S}_{\lambda A}^{\alpha g}(\zeta) = \frac{1}{|\Theta_\lambda^\alpha|} \int_{\Theta_\lambda^{\alpha g}} \left[\mathbf{L}^\alpha(\breve{\xi}, \eta) \cdot \nabla N_A(\xi_{\alpha g}, \eta, \zeta) + \mathbf{L}^\alpha(\breve{\xi}, \eta) : \nabla \mathbf{H}_A^{\alpha g}(\breve{\xi}, \eta, \zeta) \right] d\Omega \tag{5.29}$$

$$\mathbf{P}_{\lambda\gamma}^{\alpha} = \frac{1}{|\Theta_\lambda^\alpha|} \int_{\Theta_\lambda^{\alpha g}} \left[\mathbf{L}^\alpha(\breve{\xi}, \eta) : \int_{\Theta_\gamma^{\alpha g}} \nabla \mathbf{h}^\alpha(\breve{\xi}, \eta, \hat{\xi}, \hat{\eta})\, d\hat{\Omega} - \mathbf{L}^\alpha(\breve{\xi}, \eta)\, \hat{N}_\gamma(\breve{\xi}, \eta) \right] d\Omega \tag{5.30}$$

Equation (5.28) along with the evolution equations for viscoplastic slip defined for inelastic strain

coefficients ($\boldsymbol{\mu}_{\gamma}^{\alpha g}$) constitute a nonlinear, history dependent system of equations that are evaluated for the inelastic strain and stress coefficients for a prescribed macroscopic deformation state ($\mathbf{u}^{M\alpha}$) within the enrichment domain.

The reduced basis approximation of the microscale problem has the following characteristics: (1) The order of the reduced basis is of NP. The number of parts is taken to be much smaller compared to the number of degrees of freedom in a typical finite element discretization of the microstructure domain. (2) The coefficient tensors ($\mathbf{S}$ and $\mathbf{P}$) are functions of the elastic properties of the microstructure constituents, the influence functions ($\mathbf{H}$ and $\mathbf{h}$), and the scaling parameter, ζ, as shown in Eqs. (5.29) and (5.30). For a fixed scaling constant, the coefficient tensors are therefore computable a-priori, similar to the influence functions. In contrast, macroscopic discretization could include enrichment domains with varying element lengths (i.e., varying scaling constants). An relationship for computing the coefficient tensors for an arbitrary scaling constant from those pre-computed for a reference scaling constant can be obtained analytically following the coefficient tensors computing procedure. Using this relationship, a single set of coefficient tensors are stored for all enrichment domains regardless of shape.

5.4.2 The macroscale problem

Consider the component of the macroscale problem defined in Eq. (5.6) for the enrichment domain, Ω_{α}:

$$\tilde{\Phi}_{\alpha}^{M} \equiv \int_{\Omega_{\alpha}} \nabla \mathbf{w}^{M}(x,z) : \boldsymbol{\sigma}(x,\breve{x},z,t)\, d\Omega \tag{5.31}$$

Using the standard Bubnov-Galerkin approach, the macroscale test function is discretized in the local coordinate system of the enrichment domain:

$$\mathbf{w}^{M}(x,z) = \sum_{A=1}^{N_D^{\alpha}} N_A(x,z)\, \hat{\mathbf{w}}_A^{M\alpha} \tag{5.32}$$

Employing the Voigt notation (vector-matrix form), Eq. (5.31) is rewritten as:

$$\tilde{\Phi}_{\alpha}^{M} = \left(\hat{\mathbf{w}}^{M\alpha}\right)^{T} \tilde{\boldsymbol{\Psi}}_{\alpha}^{M} \tag{5.33}$$

where,

$$\hat{\mathbf{w}}^{M\alpha} = \left[\hat{\mathbf{w}}_{A}^{M\alpha}\right]_{A\in[1,N_{D}^{\alpha}]} \tag{5.34}$$

and

$$\tilde{\boldsymbol{\Psi}}_{\alpha}^{M} = \int_{\Omega_{\alpha}} \mathbf{B}^{T}(x,z)\ \boldsymbol{\sigma}\left(x,\breve{x},z,t\right)\ d\Omega \tag{5.35}$$

in which, $\mathbf{B}$ is in the form of the standard gradient of shape functions tensor. Considering the hybrid integration (Eq. (5.15)) and the reduced order approximation of the stress tensor (Eq. (5.26)), the matrix form of the macroscale weak form yields:

$$\tilde{\boldsymbol{\Psi}}_{\alpha}^{M} \approx \sum_{g=1}^{ng} \frac{\mathscr{W}_{\alpha g}}{2} \int_{\square} \mathbf{B}^{T}(\xi_{\alpha g},\eta,\zeta)\ \boldsymbol{\sigma}(\xi_{\alpha g},\breve{\xi},\eta,t)\ \mathrm{det}J(\xi_{\alpha g},\eta)\ d\breve{\Omega} = \sum_{g=1}^{ng}\ [\mathbf{B}^{\alpha g}(\zeta)]^{T}\ \boldsymbol{\sigma}^{\alpha g} \tag{5.36}$$

where,

$$\mathbf{B}^{\alpha g}(\zeta) = \left[\mathbf{B}_{\gamma}^{\alpha g}(\zeta)\right]_{\gamma\in[1,NP]}; \quad \mathbf{B}_{\gamma}^{\alpha g}(\zeta) = \frac{\mathscr{W}_{\alpha g}}{2} \int_{\square_{\gamma}} \mathbf{B}(\xi_{\alpha g},\eta,\zeta)\ \mathrm{det}J(\xi_{\alpha g},\eta)\ d\breve{\Omega} \tag{5.37}$$

and

$$\boldsymbol{\sigma}^{\alpha g} = \left[\boldsymbol{\sigma}_{\gamma}^{\alpha g}(t)\right]_{\gamma\in[1,NP]} \tag{5.38}$$

Similar to the coefficient tensors $\mathbf{S}$ and $\mathbf{P}$, $\mathbf{B}$ is a function of the scaling constant, ζ. A relationship can be obtained following the evaluation of B, such that $\mathbf{B}$ for an arbitrary scaling constant is evaluated directly from a $\mathbf{B}$ matrix pre-computed for a reference scaling constant.

Considering the discretization of the macroscale weak form over the entire macroscopic domain (Eq. (5.6)), the macrocale system of equations in the global coordinate system is defined as:

$$\boldsymbol{\Psi}^{\prime M} \equiv \mathop{\mathbf{A}}_{e}\ \boldsymbol{\Psi}^{\prime M}_{e} = 0; \quad \forall\ \Omega_{e} \in \Omega \tag{5.39}$$

where, $\mathbf{A}$ is the standard finite element assembly operator. For each enrichment domain, $\Omega_e \in \{\Omega_\alpha | \alpha = 1,2,...,n_{\text{en}}\}$, the residual in the global coordinate system is obtained from that defined in the local coordinate system of the enrichment domain:

$$\Psi'^{M}_{e} = \Psi'^{M}_{\alpha} = \mathbf{R}\ \Psi^{M}_{\alpha}; \quad \Omega_e \in \Omega_\alpha (\alpha = 1,2,...,n_{\text{en}}) \tag{5.40}$$

in which, $\mathbf{R}$ is the coordinate rotation tensor between the enrichment domain ($\mathbf{x}$) and the global coordinate system ($\mathbf{x}'$). The residual of the macroscale weak form in the local coordinate system is expressed as:

$$\Psi^{M}_{\alpha} \equiv \tilde{\Psi}^{M}_{\alpha} - \tilde{\Psi}^{MT}_{\alpha} \tag{5.41}$$

where, $\tilde{\Psi}^{M}_{\alpha}$ is described in Eq. (5.36) and:

$$\tilde{\Psi}^{MT}_{\alpha} = \int_{\Gamma^t_\alpha} \mathbf{N}^M(x,z) \cdot \tilde{\mathbf{t}}\, d\Gamma \tag{5.42}$$

where, $\mathbf{N}^M$ denotes the standard shape function matrix in Voigt notation. Γ^t_α is the part of the enrichment domain boundary that intersects with the Neumann boundary of the problem domain ($\Gamma^t_\alpha \equiv \Gamma_\alpha \cap \Gamma^t$), in the absence of the microscale displacement field contribution. For macroscale elements that discretize the substrate region ($\Omega_e \in \Omega_s$), the residual of the macroscale weak form is expressed as:

$$\Psi'^{M}_{e} = \Psi'^{M}_{s} \equiv \tilde{\Psi}'^{M}_{s} - \tilde{\Psi}'^{MT}_{s}; \quad \Omega_e \in \Omega_s \tag{5.43}$$

where,

$$\tilde{\Psi}'^{M}_{s} = \int_{\Omega_s} \mathbf{B}^T(x',z')\ \boldsymbol{\sigma}\left(x',z',t\right)\ d\Omega; \quad \tilde{\Psi}'^{MT}_{s} = \int_{\Gamma^t_s} \mathbf{N}^M(x',z') \cdot \tilde{\mathbf{t}}\, d\Gamma \tag{5.44}$$

Γ^t_s is the part of the substrate region boundary that intersects with the Neumann boundary of the problem domain ($\Gamma^t_s \equiv \Gamma_s \cap \Gamma^t$). The microstructural displacement remains unresolved in the substrate region, Ω_s, and the stress response is a function of the macroscale displacement field only. Equation (5.39) constitutes the nonlinear system of equations for the evaluation of the macroscale

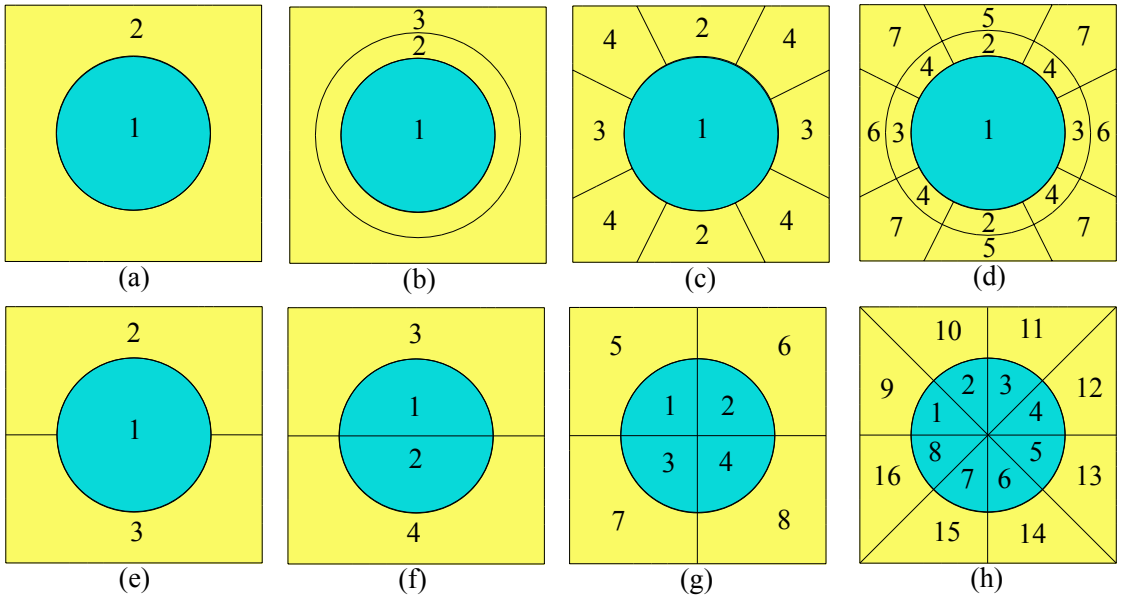

Figure 5.5: Partition patterns of a heterogeneous microstructure.

problem. The consistent linearization and numerical evaluation algorithm for the resulting system is performed using the Newton-Raphson scheme. The linearization and numerical evaluation for HROVME is similar to the ROVME method provided in Chapter 3 and skipped herein for brevity.

5.5 Hourglassing Control

Numerical investigations indicate that the ROVME approach exhibit hourglassing behavior. In this section, we demonstrate that the observed hourglassing is linked to the reduced order partitioning strategy as well as the morphology of the heterogeneous microstructure. We also indicate that this phenomenon is generally not possible for properly integrated HROVME approach.

Hourglassing is a well-known phenomenon in underintegrated finite elements, which makes possible deformation modes associated with no energy [94, 95, 96, 97]. Hourglassing is possible in the presence of rank deficiency in element stiffness matrices. In the context of 2D bilinear quadrilaterals underintegrated by a single quadrature point, the rank of the element stiffness matrix is 3, whereas a fully integrated element has a stiffness matrix of rank 5.

In the absence of inelastic effects, the element stiffness matrix for an enrichment domain using

Table 5.1: Rank of the element stiffness matrix for the heterogeneous microstructure.

Partition	(a)	(b)	(c)	(d)	(e)	(f)	(g)	(h)
Rank of the element stiffness matrix	3	3	3	3	5	5	5	5

ROVME is expressed as [39]:

$$\mathbf{K}_\alpha = \sum_{\gamma=1}^{NP_\alpha} (\mathbf{B}_\gamma)^T \mathbf{S}_\gamma \tag{5.45}$$

where,

$$\mathbf{B}_\gamma = \left[\int_{\Omega_\gamma^\alpha} \nabla N_A \, d\Omega \right]_{A\in[1,N_D]} \tag{5.46}$$

$$\mathbf{S}_\gamma = \left[\frac{1}{|\Omega_\gamma^\alpha|} \int_{\Omega_\gamma^\alpha} \mathbf{L}\cdot\nabla N_A + \mathbf{L} : \nabla \mathbf{H}_A^{\alpha g} \, d\Omega \right]_{A\in[1,N_D]} \tag{5.47}$$

In order to demonstrate the occurrence of hourglassing in the ROVME approach, we consider a square unit cell reinforced with a single circular inclusion. The macrostructure is discretized using a single finite element that constitutes the enrichment domain. Employing eight partition patterns, the element stiffness matrix for each of them is computed by Eq. (5.45) and the corresponding rank is listed in Table 5.1. The rank deficiency occurs when the centroids of all the reduced model parts coincide with the centroid of the macroscale element (e.g, partition pattern (a)-(d)). Sufficient ranks are obtained when at least the centroid of one of the parts is not located at the center of the element (e.g, partition pattern (e)-(h)).

The hybrid integration for reduced order variational multiscale enrichment method avoids the hourglassing instabilities using Eq. (5.36) with $ng > 1$. Since the partition pattern of each of the microstructure, $\Theta_{\alpha g}$ $(g = 1,2,...,ng)$, is independent of the other microstructures (as shown in Fig. 5.6 for $ng \geq 2$), it is impossible for the centroid of all parts in the enrichment domain to coincide with the center of the enrichment domain. None of the macroscale elements in Fig. 5.6 demonstrated the hourglassing instability issue when employed through the HROVME method.

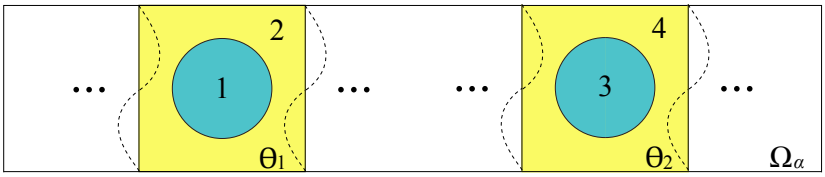

(a)

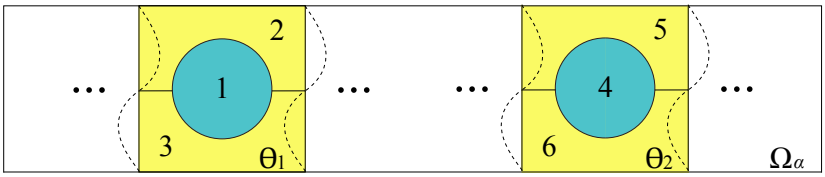

(b)

Figure 5.6: Partition patterns of an HROVME heterogeneous enrichment domain with $ng = 2$.

Table 5.2: Materials parameters for phase II material in the microstructure.

E [GPa]	ν	A [MPa]	B [MPa]
120.8	0.32	895	125
m	n	γ [MPa/second]	q
0.85	0.2	20	1.0

5.6 Numerical Verification

The implementation of the proposed approach is verified through numerical simulations under the 2-D plane strain condition. The performance and accuracy characteristics of the hybrid integration for the ROVME method are assessed by comparing the results with the direct ROVME method [39, 86]. The verification simulations are conducted without thermal effects. The microstructure is taken to be a two-phase particulate composite with circular inclusions as shown in Fig. 5.7(b). Phase I (particle) is taken to be elastic with Young's modulus (E) of 395 GPa and Poisson's ratio (ν) of 0.25, where phase II matrix behaves elasto-viscoplastically. The viscoplasticity model employed to describe the matrix behavior is standard and described in detail in Chapter 2. The model relies on the Perzyna formulation to describe the viscoplastic slip evolution, whereas a Johnson-Cook type model is used to describe hardening evolution. Table 5.2 provides the summary of the material parameter values used in this section. Phase III denotes the homogenized composite

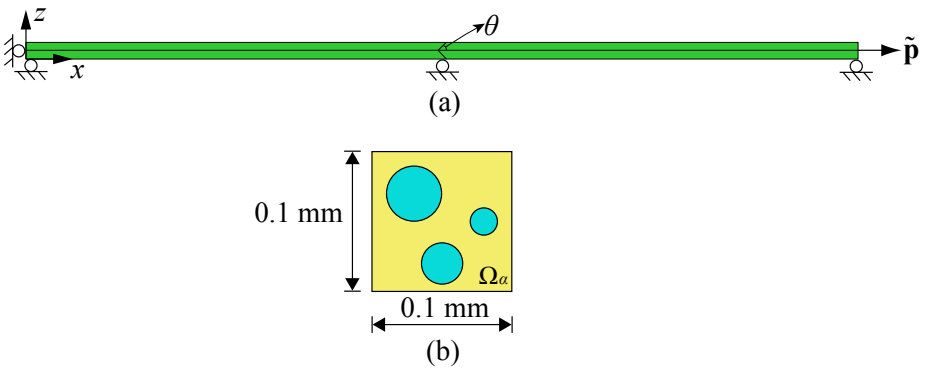

Figure 5.7: Model sketch and discretization of the uniaxially loaded specimens: (a) the HROVME macroscale model; and (b) the microstructure model.

used in the substrate region, the properties of which are obtained through the rule of mixtures and taken to remain elastic [81, 83]. The Young's modulus and Poisson's ratio of the homogenized substrate are 170 GPa and 0.3, respectively.

5.6.1 Uniaxially loaded specimens

We start by the verification of the proposed approach in the context of uniaxial loading. The macroscale problem domain and its discretization is shown in Fig. 5.7(a). The domain is discretized into 4 quadrilateral elements of high aspect ratio. Element distortion angle, θ, is used to characterize the shape of the elements. The discretization of the reference ROVME model considers a structured mesh, where each element coincides with a microstructure. The size of the microstructures is 0.1 mm$\times$0.1 mm. The reduced order models in both the proposed and the reference ROVME methods employ a 2-part partitioning of the microstructure according to the phases. A uniform pressure load is applied on the right edge of the numerical specimens, which linearly increases from 0 to 2500 MPa in 360 seconds, at the rate of 6.94 MPa/second. The time step size employed in the simulations is 18 seconds. Further refinement of the time step size does not change the results significantly. Considering two integration points in the scale separable direction (ng=2), three HROVME specimens are tested with $\theta = 90^{\text{o}}$ and size scale constants of ζ=0.1, 0.05 and 0.02.

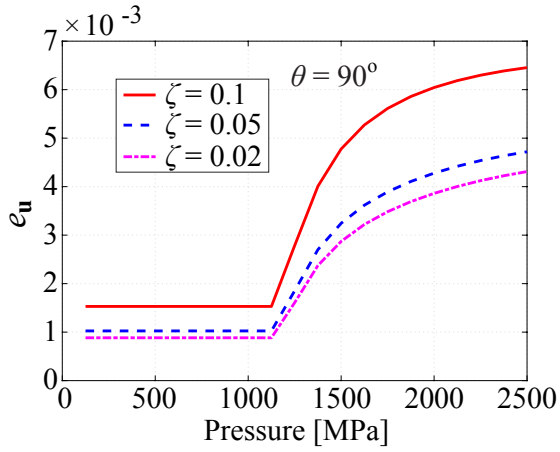

Figure 5.8: Errors in displacement field for the uniaxially loaded specimens with different ζ values.

To investigate the accuracy of the HROVME approach compared with the ROVME method, the error over the enrichment region at an arbitrary time, t, is evaluated by:

$$e_{\phi}(t) = \frac{\sum_{\alpha=1}^{n_{\text{en}}} \sum_{\gamma=1}^{NP} \left\| \phi^{\text{ROVME}}(t) - \phi^{\text{HROVME}}(t) \right\|_{2,\Omega_{\gamma}^{\alpha}}}{\sum_{\alpha=1}^{n_{\text{en}}} \sum_{\gamma=1}^{NP} \left\| \phi^{\text{ROVME}}(t) \right\|_{2,\Omega_{\gamma}^{\alpha}}} \tag{5.48}$$

where, ϕ^{ROVME} and ϕ^{HROVME} denote a response field obtained from the reference and the proposed models, respectively. $\|\cdot\|_{2,\Omega_{\gamma}^{\alpha}}$ is the discrete L_2 norm of the response field computed over Ω_{γ}^{α}. The error in displacement field is presented in Fig. 5.8 as a function of the applied pressure amplitude and ζ. The accuracy of the proposed approach increases with decreasing ζ. This result agrees with the fundamental property that the hybrid integration scheme is weakly convergent to the reference approach at the limit $\zeta \to 0$. High accuracy is achieved for the simulations with less than 1% maximum error. For each of the specimen, the error remains constant in the elastic state (before pressure reaches 1250 MPa) and starts to accumulate at the onset of the inelastic deformation. Compared with the reference simulations, the computational time improvement of the proposed method is 6.43 times for $\zeta = 0.1$, 9.54 times for $\zeta = 0.05$ and 23.28 times for $\zeta = 0.02$.

HROVME simulations with various distortion angles, θ, are also performed. When θ=90^{o},

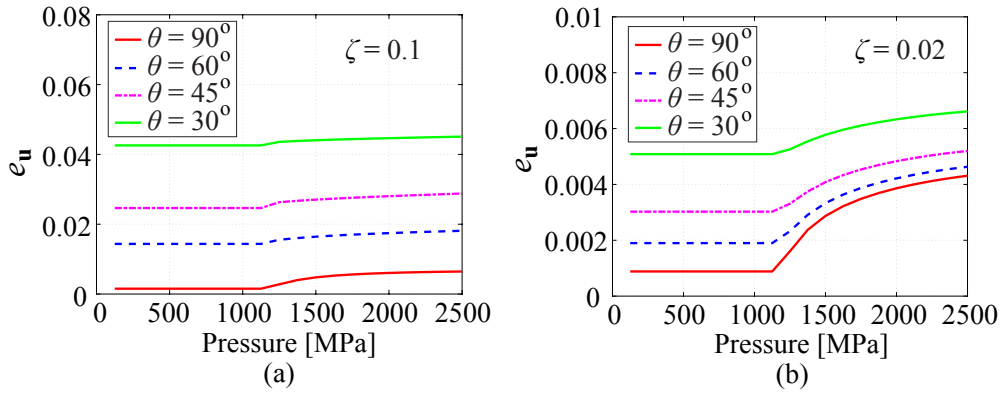

Figure 5.9: Errors in displacement field for the uniaxially loaded specimens with different θ and: (a) ζ=0.1; and (b) ζ=0.02.

the specimen is discretized into four rectangular, undistorted, enrichment domains, while $\theta \neq 90^o$ implies distortion, with lower values indicating more significant distortion of the enrichment domains. Figure 5.9 presents the displacement errors as functions of the applied pressure amplitude, distortion and ζ. The plots indicate accuracy degradation as the angle, θ, decreases. The discretization with lower ζ is less sensitive to distortion induced accuracy degradation. The distortion effect is relatively small when $\zeta/\tan\theta \leq 0.03$.

5.6.2 A ring specimen

To further verify the proposed approach, the accuracy is assessed through a ring specimen under displacement controlled loading condition as shown in Fig. 5.10. The inner and outer diameters of the ring are 24.46 mm and 26.46 mm, respectively. Only a quarter of the ring is modeled due to symmetry. Along the radius direction, both of the models are discretized into 10 enrichment domains. In the hoop direction, the HROVME and ROVME specimens are discretized into 20 and 200 enrichment domains, respectively. The ζ value of the HROVME enrichment domains is therefore 0.1. Along the scale separable direction, 2 integration points are employed for the hybrid integration (ng=2). All of the macroscale elements are taken as enrichment domains and their distortion is not significant ($\zeta/\tan\theta < 0.03$). The maximum amplitude of the displacement controlled load is 1 mm, at the rate of 2.8×10^{-3} mm/second. The time step size is set to 9 seconds.

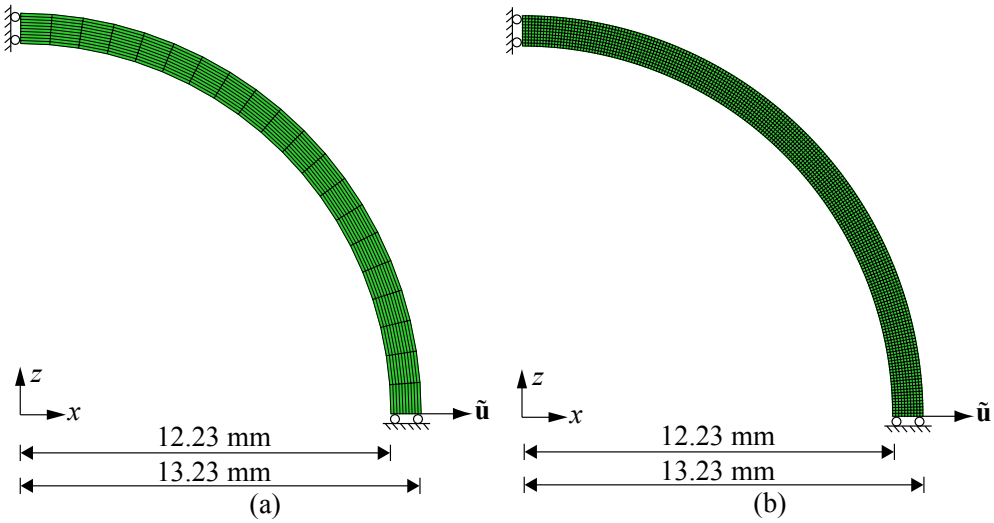

Figure 5.10: Model sketch and discretization of the ring specimen: (a) the HROVME macroscale model; and (b) the ROVME macroscale model.

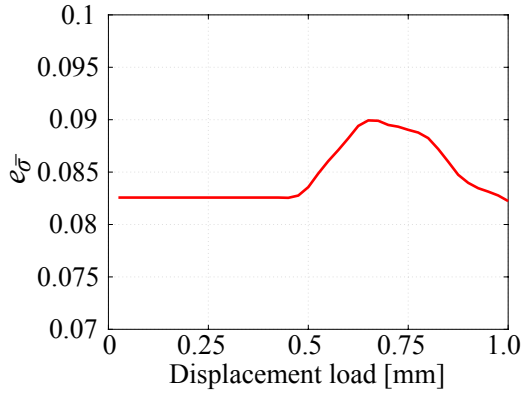

Figure 5.11: Error in equivalent stress for the ring specimen.

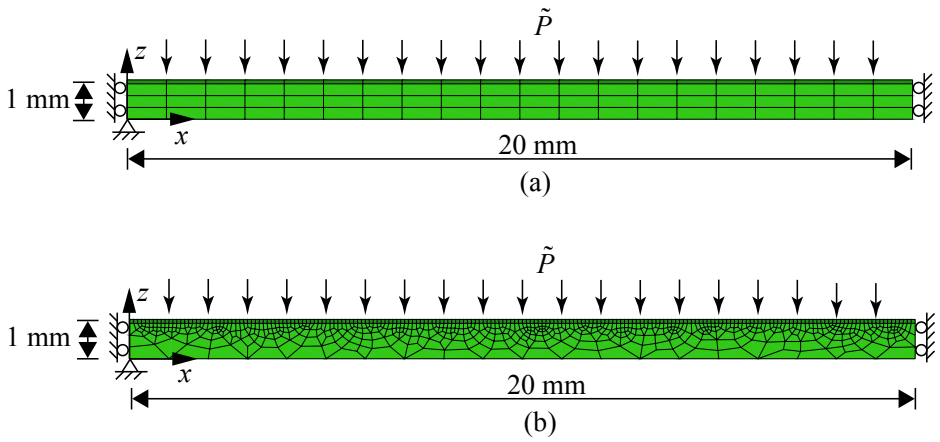

Figure 5.12: Model sketch and discretization of the beam specimen: (a) the HROVME macroscale model; and (b) the ROVME macroscale model.

The error in equivalent stress for the HROVME method compared to the reference model is plotted in Fig. 5.11 as a function of the magnitude of the prescribed displacement load. The specimen deforms elastically until the load reaches 0.4 mm. At the beginning of the inelastic state, the error slightly increases and then drops back as the size of the inelastic region grows in the structure. The maximum error over the simulation in terms of equivalent stress is less than 9%. The HROVME simulation is 6.07 times faster than the ROVME model which demonstrates the computational efficiency of the proposed approach.

5.6.3 A beam specimen

The proposed HROVME method is further verified using the numerical analysis of a beam. In this case, a substrate region is also included. A set of HROVME simulations with different number of integration points ($ng = 2,3,4,5$) in the scale separable direction (x-direction in the current example) are performed to assess the accuracy characteristics of HROVME. The dimension of the specimen is 40 mm$\times$1 mm and only half of the beam is modeled due to symmetry. The sketch and discretization of the HROVME and ROVME macroscale problems are presented in Fig. 5.12(a) and (b), respectively. The HROVME macroscale model contains 80 elements of which the 20 dark elements in the top layer are taken as enrichment domains with $\zeta = 0.1$. The reference model is

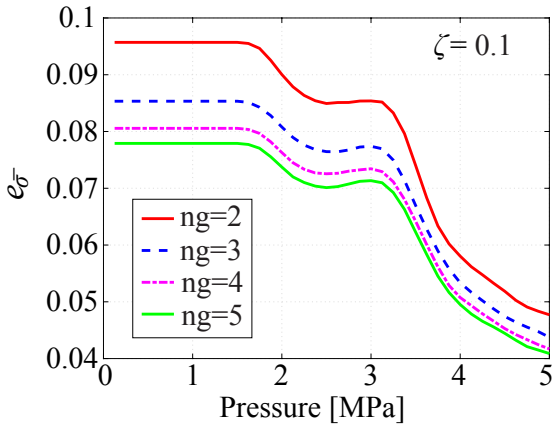

Figure 5.13: Errors in equivalent stress for the beam specimen with different number of integration points in the scale separable direction.

discretized into 755 quadrilateral macroscale elements of which the top layer of elements (200 dark shaded) are enriched. The remainder of the elements remains unenriched and modeled with the substrate material properties. A uniform pressure load is applied on the top edges of the specimens which linearly increases to 5 MPa at the rate of 1.39×10^{-2} MPa/second. The employed time step size is identical to the previous example.

Figure 5.13 shows the equivalent stress error as a function of load amplitude and number of integration points employed in the scale separable direction. Similar to the previous examples, the errors are stable within the elastic state. Inelastic deformation occurs when the pressure is approximately 1.6 MPa. The results demonstrate that the accuracy of the HROVME model is enhanced by employing higher number of integration points in the scale separable direction, at the expense of higher computational cost. The computational efficiency of the proposed approach compared to the reference model are 6.95, 4.82, 3.91 and 3.5 times for ng=2, 3, 4 and 5, respectively.

5.7 A Coupled Transport-Thermo-Mechanical Problem

The capabilities of the proposed computational framework is demonstrated by performing a coupled transport-thermo-mechanical analysis of a stiffened skin structure. Figure 5.14 illustrates the geometry and loading conditions of the structure. where $\tilde{P}$ is the applied pressure amplitude, $\tilde{T}_1$

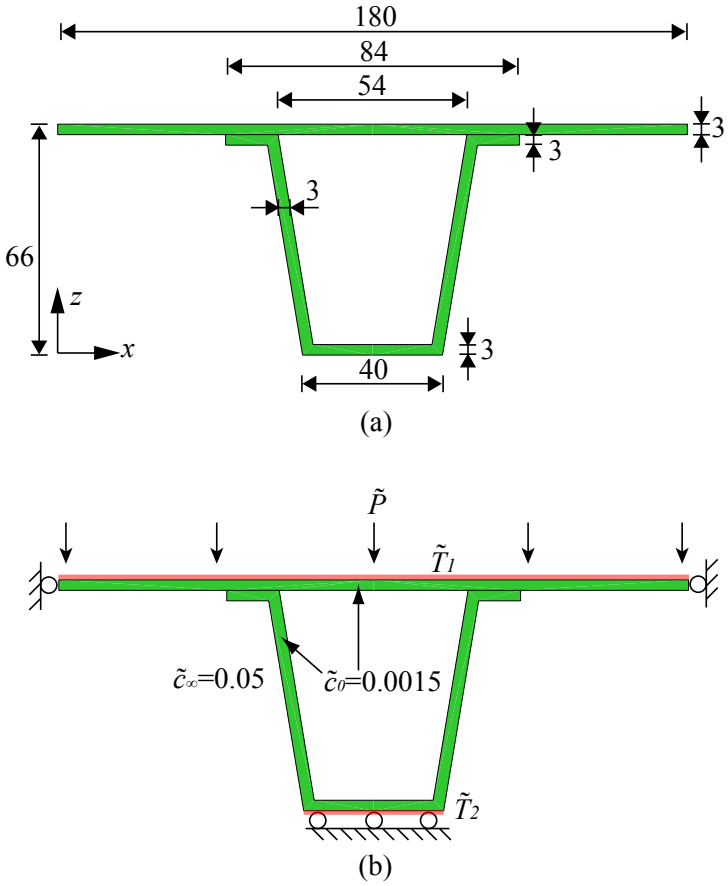

Figure 5.14: Model sketch of the stiffened panel specimen: (a) geometry in mm; and (b) loading conditions.

Table 5.3: Materials parameters for the transport-thermo-mechanical problem.

Material type	E_0 [GPa] [1]	ν	A [MPa]	B [MPa]	m
Phase I	130	0.32	600	1000	0.85
Phase II	107	0.32	350	250	0.85
Substrate	120.8	0.32	500	700	0.85
Material type	n	F [MPa]	γ[MPa/second]	q	$\alpha^T [1/^oC]$
Phase I	0.900	110	20	1.0	7.3×10^{-6}
Phase II	0.975	110	20	1.0	8.3×10^{-6}
Substrate	0.930	110	20	1.0	7.7×10^{-6}

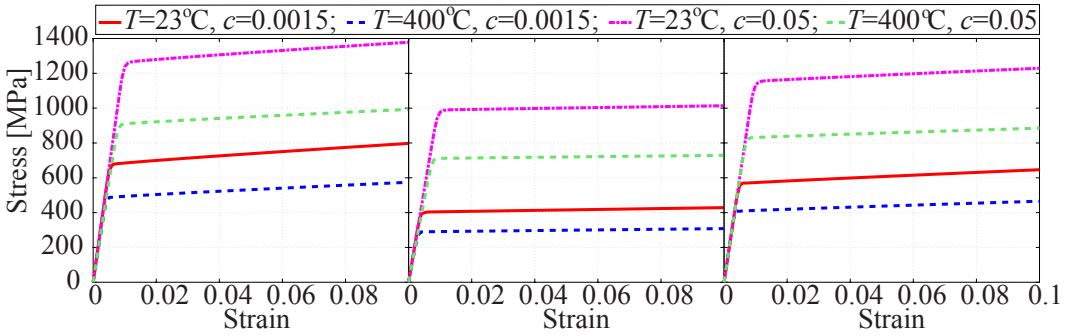

Figure 5.15: Constitutive response of the constituent materials at various temperature and aggressive agent concentration: (a) phase I; (b) phase II; and (c) substrate material.

and $\tilde{T}_2$ are prescribed boundary temperatures, $\tilde{c}_0$ denotes the initial aggressive agent concentration and $\tilde{c}_\infty$ is the prescribed boundary concentration. In this example, we are interested in modeling the effect of the ingress of an aggressive environmental agent, e.g. oxygen in the current example. At high temperature, the aggressive agent ingress is modeled as Fick's diffusion. The diffusion coefficient is taken to be temperature dependent [53]:

$$D(T) = D_0 \exp\left(-\frac{Q}{RT}\right) \tag{5.49}$$

where, D_0=62 mm^2/second is the diffusivity at the room temperature, Q=126 kJ/mole the activation energy, R the universal gas constant and T the temperature.

The temperature effect on the mechanical behavior of the constituent materials is through temperature dependent elastic moduli, yielding and the thermal expansion which are considered fol-

[1] E_0 denotes the Young's modulus at the room temperature.

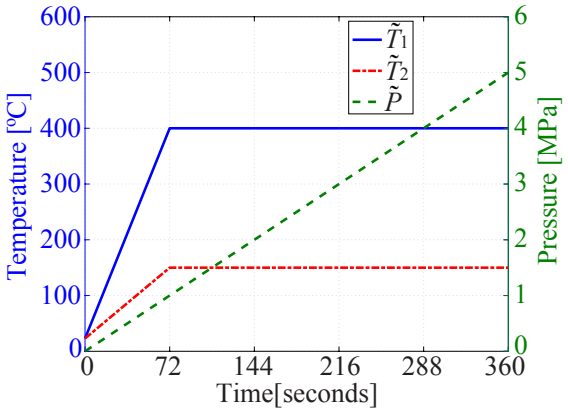

Figure 5.16: Time history of loading conditions for the stiffened panel specimen.

lowing the algorithms in Ref. [86]. The viscoplastic hardening of the constituent materials are taken to be a function of the aggressive agent concentration and temperature through the modified Johnson-Cook model as [53]:

$$\sigma_y = [A + B(\bar{\varepsilon}^{vp})^n + Fc]\,[1 - (T^*)^m] \tag{5.50}$$

where, A, B, F, m and n are material parameters; c the aggressive agent concentrate and T^* the non-dimensional temperature as defined in Eq. (4.46). A two-phase microstructure is considered for the material. The material properties of the constituent materials are listed in Table 5.3. The Young's moduli of the materials linearly vary as a function of temperature with 0.0381 GPa/^{o}C, 0.0314 GPa/^{o}C and 0.0354 GPa/^{o}C for phase I, II and substrate materials. Phase I and II behave similarly to high and low yield stress titanium material, respectively. The properties of the substrate material are obtained through mixture theory. At 0.056/second of strain loading rate, the constitutive responses of the constituent materials under various temperature and concentration conditions are plotted in Fig. 5.15.

The top and bottom surfaces of the structure are exposed to 400^{o}C and 150^{o}C, which results in a non-uniform temperature distribution as shown in Fig. 5.17. Under this steady state temperature condition, aggressive agents ingress into the structure resulting in a non-uniform distribution of concentrations as shown in Fig. 5.18 after an exposure duration of 50 hours. Along the surfaces of

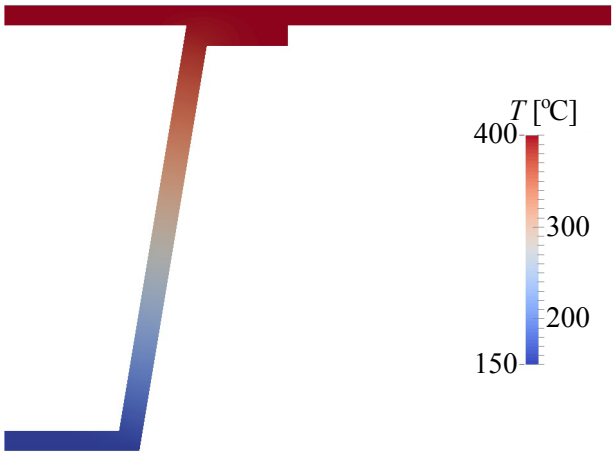

Figure 5.17: Temperature contour of the stiffened panel specimen

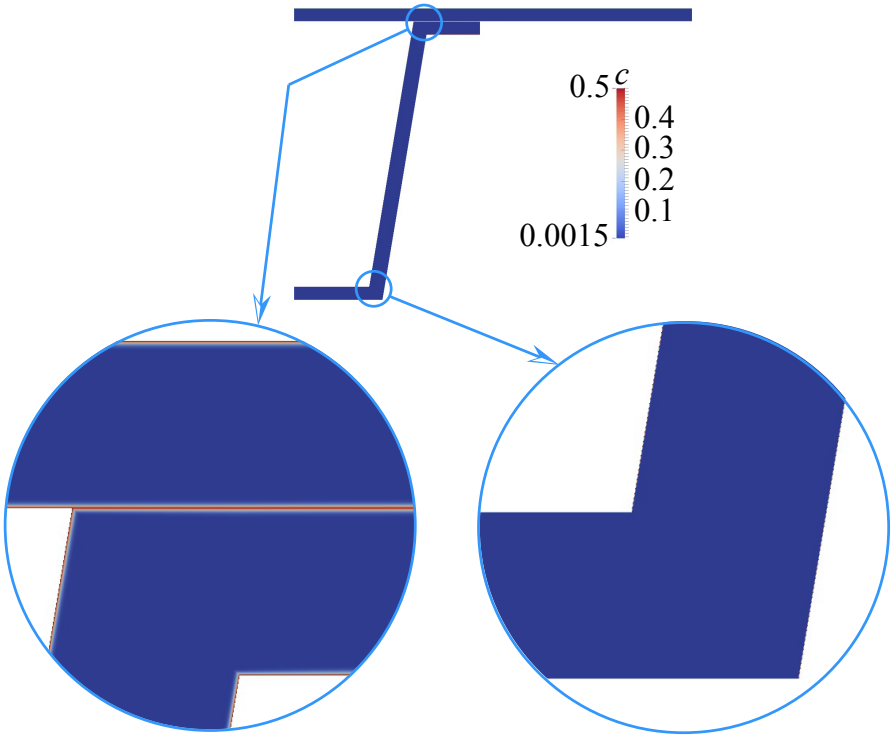

Figure 5.18: Aggressive agent concentration contour of the stiffened panel specimen.

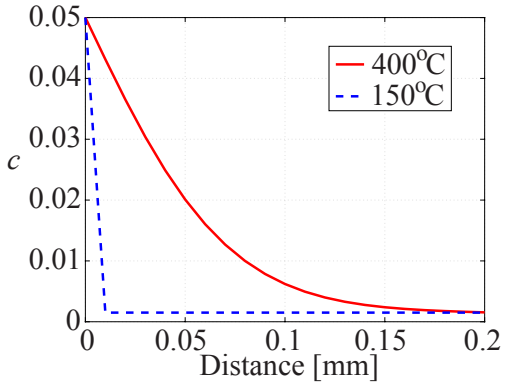

Figure 5.19: Aggressive agent concentration distributions along with the distance to the ambient surface.

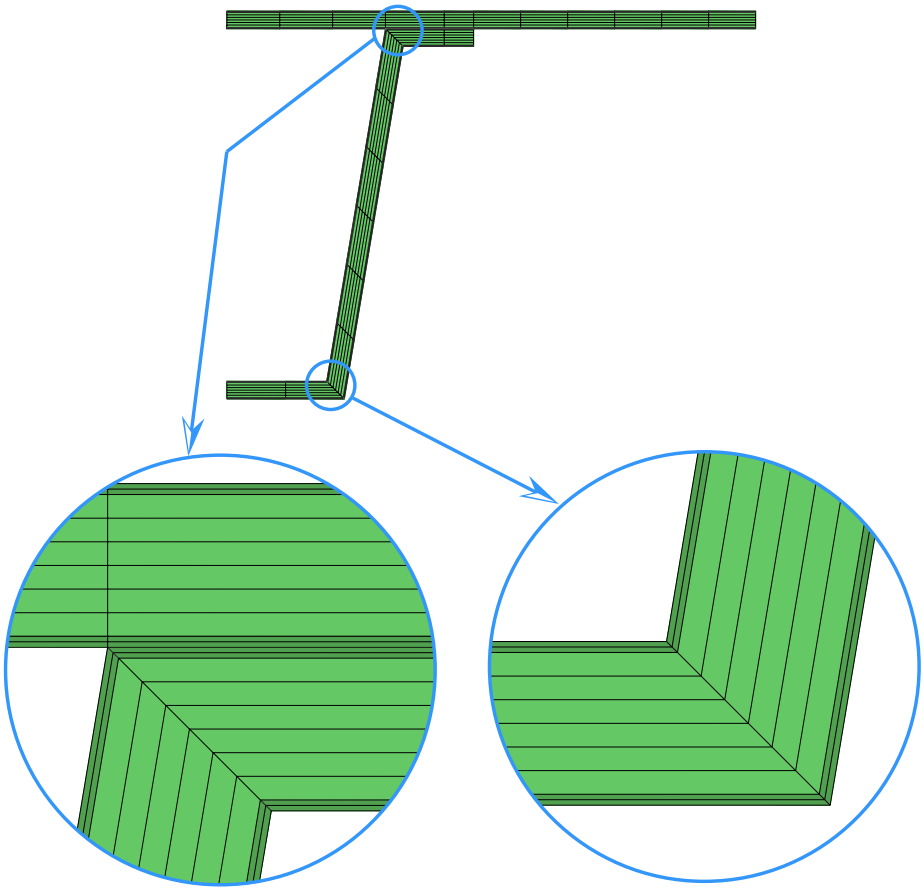

Figure 5.20: Macroscale discretization of the HROVME model.

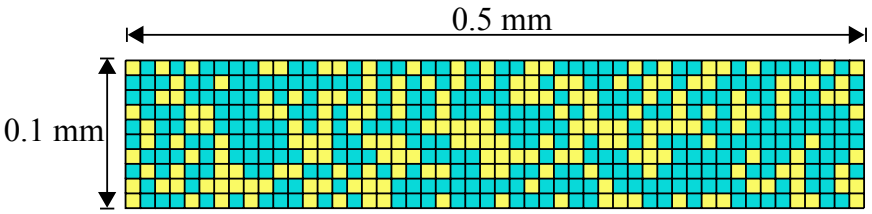

Figure 5.21: Resolved microstructure of the HROVME model.

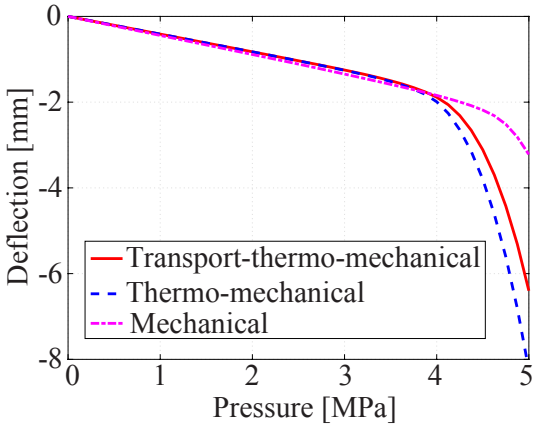

Figure 5.22: Center deflections along with pressure load.

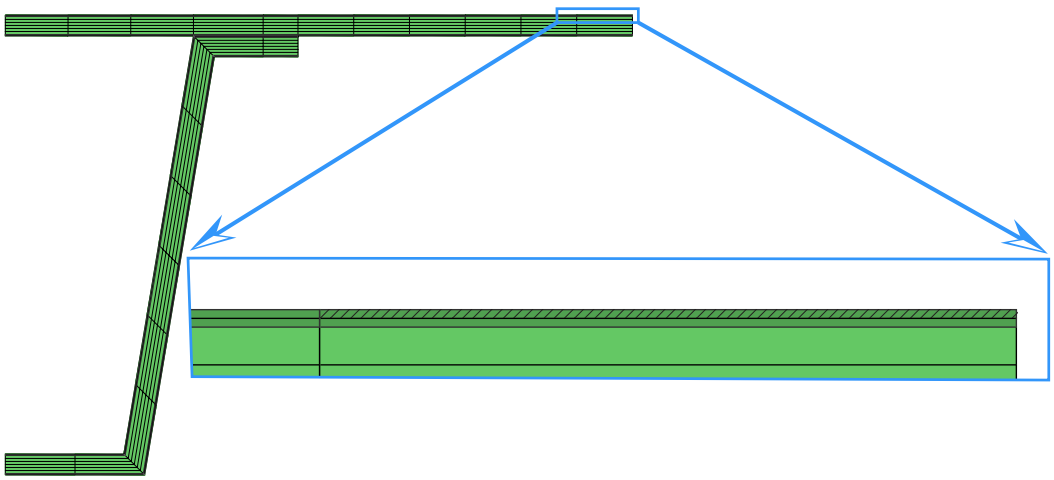

Figure 5.23: Position of the critical enrichment domain (dashed).

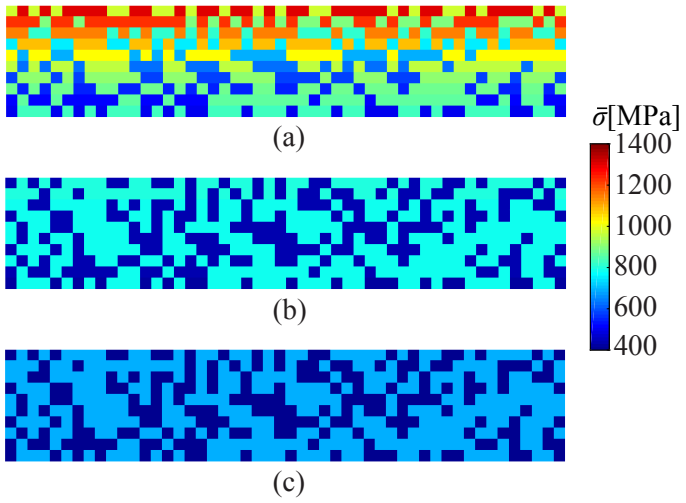

Figure 5.24: Stress countours of the critical microstructure for specimen subjected to: (a) transport-thermo-mechanical loads; (b) thermo-mechanical loads; and (c) only mechanical load.

the panel and the hat stiffener, the aggressive agent diffuses into the structure due to the induced concentration gradients. The region near the hot boundary has significant diffusion whereas, the region near the cool surface does not exhibit significant diffusion. The detailed concentration distribution as a function of the distance to the ambient surface is plotted in Fig. 5.19 for near hot and cold surfaces. The structure is then subjected to a pressure load which linearly increases to 5 MPa.

In order to capture the effect of the aggressive agent on the structural behavior, two layers of enrichment domains are embedded along the surfaces of the specimen as illustrated in Fig. 5.20. The thickness of each layer is 0.5 mm. A two-phase microstructure, as shown in Fig. 5.21, is used within the enrichment domains. The microstructure is discretized into 20 parts, 2 parts associated with the phases in each of the 10 layers. The number of integration points in the scale separable direction of the the hybrid integration is 2 (ng=2). In view of the size of the structure, direct resolution of each microstructure along the surface region is computationally prohibitive and the reference approach is not employed in this study. Three cases of loading conditions are investigated to assess the effect of field coupling on the mechanical response including (a) a transport-thermo-mechanical case, (b) a thermo-mechanical case without considering aggressive agent ingress and

(c) a pure mechanical case at room temperature.

Figure 5.22 shows the deflection of the center of the stiffened panel for the three cases as a function of applied load. When contrasting cases (b) and (c), the presence of high temperature clearly reduces the overall stiffness of the structure and induces inelastic deformations with notably larger magnitudes. In the presence of aggressive agent ingress, case (a), the specimen exhibits a clearly stiffer response than case (b). We note that although diffusion affects the structure along a narrow surface region, the deflection change in the inelastic stage is significant. Maximum stress is contained by the critical enrichment domain right next to the top center point of the panel, as shown in Fig. 5.23. The local equivalent stress distribution within the microstructure of the critical enrichment domain is presented in Fig. 5.24 for all three simulations. The transport-thermo-mechanical specimen, case (a), demonstrates significantly higher equivalent stress due to the ingress effect and high temperature induced expansion. More importantly, the HROVME method has the capability of capturing the stress gradient induced by the aggressive agent concentration variation across the thickness of the enrichment domain, as shown in Fig. 5.23(a). In the absence of aggressive agent, the local responses of the thermo-mechanical and mechanical simulations (Figs. 5.23(b) and (c)) exhibit much uniform stress distributions within the microstructure.

Chapter 6

CONCLUSIONS AND FUTURE WORK

6.1 Conclusions

This dissertation provided a computational framework developed for the scale inseparable multiscale modeling of structures subjected to extreme environments. It contains the formulation and implementation of the variational multiscale enrichment (VME) method, including direct VME method, reduced order variational multiscale enrichment (ROVME) method for mechanical and thermo-mechanical problems, and hybrid integration for reduced order variational multiscale enrichment (HROVME) method for the analysis of surface degradation problems subjected to transport-thermo-mechanical loading conditions. Numerical verifications were performed which demonstrate the high accuracy and computational efficiency of the proposed framework. The principle achievements of this dissertation are summarized below.

Chapter 2 presented the formulation and implementation of the variational multiscale enrichment method for the analysis of elasto-viscoplastic problems. The scale inseparable feature was represented by the relatively insignificant scale size difference and strongly coupling effect between the scales. A one-parameter family of mixed boundary conditions that range from Dirichlet to Neumann was employed to study the effect of the fine scale boundary conditions on accuracy. The inelastic material behavior was modeled using Perzyna type viscoplasticity coupled with flow stress evolution idealized by the Johnson-Cook model. Numerical verifications were performed to assess the performance of the proposed approach against the direct finite element simulations. The results of verification studies demonstrated that VME with proper boundary conditions can accurately model the inelastic response accounting for material heterogeneity.

Chapter 3 provided the formulation and implementation of a novel reduced order variational multiscale enrichment method for elasto-viscoplastic problems. This method provided a hierarchical model order reduction technique based on the eigenstrain concept to approximate the fine scale

response resolved at subdomains of interest. By eliminating the requirement of direct fine scale discretization, the computational effort associated with the variational multiscale enrichment method was significantly reduced. The model order reduction was achieved in the scale inseparable inelastic problem by automatically satisfying the microscale equilibrium state through the eigenstrain concept and coarse discretization of inelastic strain fields within the microscale domain. Numerical verifications were performed to assess the capabilities of the proposed methodology, against the direct VME method with detailed fine scale resolutions. The verification results revealed high accuracy and computational efficiency of the reduced order VME framework for elasto-viscoplastic problems with material heterogeneity.

Chapter 4 introduced the formulation and implementation of the ROVME method for thermo-mechanical problems. The ROVME approach was extended to model the inelastic behavior of heterogeneous structures, in which the constituent properties were temperature sensitive. The temperature-dependent coefficient tensors of the reduced order method were approximated in an efficient manner, retaining the computational efficiency of the reduced order model in the presence of spatial/temporal temperature variations. Numerical verifications were performed to assess the efficiency and accuracy of the proposed computational framework. The results of the verifications demonstrated that ROVME retains reasonable accuracy and achieves high efficiency in the presence of thermo-mechanical loads.

Chapter 5 presented the formulation and implementation of a hybrid multiscale integration scheme for multiscale problems that exhibit different scale separation characteristics in different directions. The proposed approach employed the key ideas of the variational multiscale enrichment at directions that exhibit poor scale separation, and computational homogenization at directions with good scale separability. The proposed approach is particularly attractive for surface degradation problems in structures operating in the presence of aggressive environmental agents. Formulated in the context of variational multiscale principles, the integration scheme took advantage of homogenization-like integration along directions that exhibit scale separation. The proposed integration scheme was applied to the reduced order variational multiscale enrichment (ROVME)

method in order to arrive at a computationally efficient multiscale solution strategy for surface degradation problems. Numerical verifications were performed to verify the implementation of the hybrid multiscale integrator. The results of the verifications revealed high accuracy and computational efficiency, compared with the direct ROVME simulations. A coupled transport-thermo-mechanical analysis was presented to demonstrate the capability of the proposed computational framework.

The computational framework proposed by the current dissertation has the capabilities of accurately and efficiently modeling structural components subjected to extreme environments. It is especially beneficial for the analysis of structural components with high dimensional aspect ratio, such as thin and long panels, in the presence of surface degradation phenomenon. Considering the coupling effects of transport-thermo-mechanical problems, the proposed VME framework accurately predicts the structural responses by resolving the material heterogeneity in the critical directions of the surface degradation.

6.2 Future Work

To expand the applicability of the proposed computational framework, particularly to model structures operating in severe environments, several issues remain to be resolved. First, damage models, such as Johnson-Cook damage model [77], should be considered to predict the initiation and propagation of surface cracks. In its current state, the proposed framework has the capability of accurately tracking the response evolution in the structures. Appropriate failure initiation criteria should be employed based on the associated material responses. Another challenge for the prediction of surface crack propagation is the choice of microscale boundary conditions. The microscale boundary conditions considered in the current dissertation, homogeneous Dirichlet boundary conditions and mixed boundary conditions, do not permit communication of discontinuous displacement field among the enrichment domains. Additional investigations should be performed to select or develop appropriate boundary conditions for the microscale problems, in order to capture the cross-domain crack propagation. When the crack initiation and propagation are successfully mod-

eled, the effect of the mechanical response on the aggressive agents ingress problems would be considered accurately. As aggressive agents transport freely along the crack paths, material failure permits faster ingress procedure of the aggressive agents. Second, material models considering fatigue loading conditions, such as acoustic loads, should be incorporated into the current framework for the fatigue life prediction of the structures. Currently, the computational framework only allows monotonic mechanical loads. Fatigue loading conditions and the associated material models need to be implemented in the context of the VME framework. Third, high fidelity microstructure models, such as crystal plasticity finite element method, should be employed for the miscroscale problems. In the presence of high fidelity microscale problems, the environmental exposure induced material property changes and microstructural topology evolutions would be characterized in more accurate ways, especially for metal materials. The localized damage initiation at the scale of the material microstructure near stress risers would be captured accurately, such as persistent slip bands, high-angle grain boundaries, triple junctions, microtextured regions and others. To achieve high computational efficiency, the high fidelity models should be implemented in the context of hybrid integration and reduced order variational multiscale enrichment method. New formulation and implementation strategies should be devised based on the available model order reduction techniques in the high fidelity modeling area. Fourth, higher order enrichment domains is desirable in view of modeling structures with high gradient responses. As C^0 continuous elements is employed in the current framework, higher order macroscale elements (e.g., C^1 continuous elements) should be implemented to enhance the capability of the variational multiscale enrichment framework. Last but not the least, an adaptive enrichment region selection scheme should be developed from the perspective of further improving the computational efficiency of the proposed framework. In the current state, the enrichment domains are pre-selected at the beginning of the simulations, according to the characters of the problems or results of trial simulations. The adaptive enrichment region selection scheme would allow the evolution of the enrichment region, therefore avoid unnecessarily enriched subdomains or overlooked critical subdomains. The major challenge exists in the development of the adaptive selection scheme is the accurate transformation between an

unenriched element with phenomenologically represented materials and a enriched domain with resolved material heterogeneities, maintaining the balance of energy and response continuity along the microscale boundaries.

BIBLIOGRAPHY

[1] T. J. R. Hughes, G. R. Feijoo, and J. B. Quincy. The variational multiscale method - a paradigm for computational mechanics. *Comput. Methods Appl. Mech. Engrg.*, 166:3–24, 1998.

[2] C. Oskay. Variational multiscale enrichment for modeling coupled mechano-diffusion problems. *Int. J. Numer. Meth. Engng.*, 89:686–705, 2012.

[3] C. D. Mote. Global-local finite element. *Int. J. Numer. Meth. Engng.*, 3:565–574, 1971.

[4] A. K. Noor. Global-local methodologies and their application to nonlinear analysis. *Finite Elements Anal. Des.*, 2:333–346, 1986.

[5] K. M. Mao and C. T. Sun. A refined global-local finite element analysis method. *Int. J. Numer. Meth. Engng.*, 32:29–43, 1991.

[6] J. Fish and S. Markolefas. Adaptive global-local refinement strategy based on the interior error estimates of the h-method. *Int. J. Numer. Meth. Engng.*, 37:827–838, 1994.

[7] L. Gendre, O. Allix, P. Gosselet, and F. Comte. Non-intrusive and exact global/local techniques for structural problems with local plasticity. *Comput. Mech.*, 44:233–245, 2009.

[8] J. Fish. The s-version of the finite element method. *Computers & Structures*, 43:539–547, 1992.

[9] O. Lloberas-Valls, D. J. Rixen, A. Simone, and L. J. Sluys. Domain decomposition techniques for the efficient modeling of brittle heterogeneous materials. *Comput. Methods Appl. Mech. Engrg.*, 200:1577–1590, 2011.

[10] C. A. Duarte and D. J. Kim. Analysis and applications of a generalized finite element method with global–local enrichment functions. *Comput. Methods Appl. Mech. Engrg.*, 197:487–504, 2008.

[11] L. Berger-Vergiat, H. Waisman, B. Hiriyur, R. Tuminaro, and D. Keyes. Inexact schwarz-algebraic multigrid preconditioners for crack problems modeled by extended finite element methods. *Int. J. Numer. Meth. Engng*, 90:311–328, 2012.

[12] B. Hiriyur, R.S. Tuminaro, H. Waisman, E.G. Boman, and D.E. Keyes. A quasi-algebraic multigrid approach to fracture problems based on extended finite elements. *SIAM J. Sci. Comput.*, 34:A603–A626, 2012.

[13] H. Waisman and L. Berger-Vergiat. An adaptive domain decomposition preconditioner for crack propagation problems modeled by xfem. *Int. J. Mult. Comp. Eng.*, 2013:633–654, 2013.

[14] D. Markovic and A. Ibrahimbegovic. On micro-macro interface conditions for micro scale based FEM for inelastic behavior of heterogeneous materials. *Comput. Methods Appl. Mech. Engrg.*, 193:5503–5523, 2004.

[15] V. Guptaa, C.A. Duartea, I. Babuska, and U. Banerjee. Stable GFEM(SGFEM): Improved conditioning and accuracy of GFEM/XFEM for three-dimensional fracture mechanics. *Comput. Methods Appl. Mech. Engrg.*, 289:355–386, 2015.

[16] K. Matous, H.M. Inglis, X. Gu, D. Rypl, T.L. Jackson, and P.H. Geubelle. Multiscale modeling of solid propellants: From particle packing to failure. *Compos. Sci. Technol.*, 67:1694–1708, 2007.

[17] T. Y. Hou and X. Wu. A multiscale finite element method for elliptic problems in composite materials and porous media. *J. Comput. Phys.*, 134:169–189, 1997.

[18] Y. Efendiev and T. Y. Hou. *Multiscale Finite Element Methods-Theory and Applications*. Springer-Verlag, New York, 2009.

[19] T. Belytschko, S. Loehnert, and J. Song. Multiscale aggregating discontinuities: A method for circumventing loss of material stability. *Int. J. Numer. Meth. Engng.*, 73:869–894, 2008.

[20] J. Song and T. Belytschko. Multiscale aggregating discontinuities method for micro-macro failure of composites. *Composites: Part B*, 40:417–426, 2009.

[21] T. Arbogast. Implementation of a locally conservative numerical subgrid upscaling scheme for two-phase Darcy flow. *Comput. GeoSci.*, 6:453–481, 2002.

[22] T. Arbogast. Analysis of a two-scale, locally conservative subgrid upscaling for elliptic problems. *SIAM J. on Numer. Anal.*, 42:576–598, 2004.

[23] C. Oskay. Variational multiscale enrichment method with mixed boundary conditions for modeling diffusion and deformation problems. *Comput. Methods Appl. Mech. Engrg.*, 264: 178–190, 2013.

[24] S. Zhang and C. Oskay. Variational multiscale enrichment method with mixed boundary conditions for elasto-viscoplastic problems. *Comput. Mech.*, 55:771–787, 2015.

[25] I. Babuska. *Homogenization and application: mathematical and computational problems, in: B. Hubbard (Ed.), Numerical Solution of Partial Differential Equations - III*. SYNSPADE, New York, 1975.

[26] J. M. Guedes and N. Kikuchi. Preprocessing and postprocessing for materials based on the homogenization method with adaptive finite element methods. *Comput. Methods Appl. Mech. Engrg.*, 83:143–198, 1990.

[27] M. G. D Geers, V. Kouznetsova, and W. A. M. Brekelmans. Gradient-enhanced computational homogenization for the micro-macroscale transition. *J. Phys. IV*, 11:145–152, 2001.

[28] K. Terada and M. Kurumatani. Two-scale diffusion-deformation coupling model for material deterioration involving micro-crack propagation. *Int. J. Numer. Meth. Engng*, 83:426–451, 2010.

[29] M. Mosby and K. Matous. Computational homogenization at extreme scales. *Extreme Mechanics Letters*, 6:68–74, 2016.

[30] J. Aboudi. A continuum theory for fiber-reinforced elastic-viscoplastic composites. *Int. Eng. Sci.*, 20:605–621, 1982.

[31] G. J. Dvorak. Transformation field analysis of inelastic composite materials. *Proc. R. Soc. Lond. A*, 437:311–327, 1992.

[32] J. C. Michel and P. Suquet. Nonuniform transformation field analysis. *Int. J. Solids Struct.*, 40:6937–6955, 2003.

[33] F. Fritzen and M. Leuschner. Reduced basis hybrid computational homogenization based on a mixed incremental formulation. *Comput. Methods Appl. Mech. Engrg.*, 260:143–154, 2013.

[34] H. Moulinec and P. Suquet. A numerical method for computing the overall response of nonlinear composites with complex microstructure. *Comput. Methods Appl. Mech. Engrg.*, 157:69–94, 1998.

[35] J. Yvonnet and Q.-C. He. The reduced model multiscale method (R3M) for the non-linear homogenization of hyperelastic media at finite strains. *J. Comput. Phys.*, 223:341–368, 2007.

[36] J. Oliver, M. Caicedo, A. E. Huespe, J. A. Hernandez, and E. Roubin. Reduced order modeling strategies for computational multiscale fracture. *Comput. Methods Appl. Mech. Engrg.*, 313:560–595, 2017.

[37] C. Oskay and J. Fish. Eigendeformation-based reduced order homogenization for failure analysis of heterogeneous materials. *Comput. Methods Appl. Mech. Engrg.*, 196:1216–1243, 2007.

[38] X. Zhang and C. Oskay. Eigenstrain based reduced order homogenization for polycrystalline materials. *Comput. Methods Appl. Mech. Engrg.*, 297:408–436, 2015.

[39] S. Zhang and C. Oskay. Reduced order variational multiscale enrichment method for elasto-viscoplastic problems. *Comput. Methods Appl. Mech. Engrg.*, 300:199–224, 2016.

[40] W. Leclerc, N. Ferguen, C. Plegris, H. Haddad, E. Bellenger, and M. Guessasma. Anumerical investigation of effective thermoelastic properties of interconnected alumina/Al composites using FFT and FE approaches. *Mech. Mater.*, 92:42–57, 2016.

[41] B. S. Anglin, R. A. Lebensohn, and A. D. Rollett. Validation of a numerical method based on Fast Fourier Transforms for heterogeneous thermoelastic materials by comparison with analytical solutions. *Comp. Mat. Sci.*, 87:209–217, 2014.

[42] T. J. R. Hughes. Multiscale phenomena: Green's functions, the Dirichlet-to-Neumann formulation, subgrid scale models, bubbles and the origins of stabilized methods. *Comput. Methods Appl. Mech. Engrg.*, 127:387–401, 1995.

[43] A. Hund and E. Ramm. Locality constraints within multiscale model for non-linear material behaviour. *Int. J. Numer. Meth. Engng.*, 70:1613–1632, 2007.

[44] K. Garikipati and T. J. R. Hughes. A study of strain localization in a multiple scale framework: The one-dimensional problem. *Comput. Methods Appl. Mech. Engrg.*, 159:193–222, 1998.

[45] K. Garikipati and T. J. R. Hughes. A variational multiscale approach to strain localization formulation for multidimensional problems. *Comput. Methods Appl. Mech. Engrg.*, 188:39–60, 2000.

[46] K. Garikipati. Variational multiscale methods to embed the macromechanical continuum formulation with fine-scale strain gradient theories. *Int. J. Numer. Meth. Engng*, 57:1283–1298, 2003.

[47] T. J. R. Hughes and G. Sangalli. Variational multiscale analysis: the fine-scale Green's function, projection, optimization, localization, and stabilized methods. *SIAM J. Numer. Anal.*, 45:539–557, 2007. ISSN 00361429.

[48] A. Masud and K. Xia. A variational multiscale method for inelasticity: Application to superelasticity in shape memory alloys. *Comput. Methods Appl. Mech. Engrg.*, 195:4512–4531, 2006.

[49] A. Masud, T. J. Truster, and L. A. Bergman. A variational multiscale a posteriori error estimation method for mixed form of nearly incompressible elasticity. *Comput. Methods Appl. Mech. Engrg.*, 200:3453–3481, 2011.

[50] J. Yeon and S. Youn. Variational multiscale analysis of elastoplastic deformation using meshfree approximation. *Int.J.Solids Struct.*, 45:4709–4724, 2008.

[51] R. Juanes and F.-X. Dub. A locally conservative variational multiscale method for the simulation of porous media flow with multiscale source terms. *Comput. Geosci.*, 12:273–295, 2008.

[52] S. P. Walker and B. J. Sullivan. Sharp refractory composite leading edges on hypersonic vehicles. *AIAA 20036915, Proceedings of the 12th AIAA International Space Planes and Hypersonic Systems and Technologies, 1519 December 2003, Norfolk, VA.*, 2003.

[53] C. Oskay and M. Haney. Computational modeling of titanium structures subjected to thermo-chemo-mechanical environment. *Int. J. Solids Struct.*, 47:3341–3351, 2010.

[54] P. O' Hara, C. A. Duarte, T. Eason, and J. Garzon. Efficient analysis of transient heat transfer problems exhibiting sharp thermal gradients. *Comput. Mech.*, 51:743–764, 2013.

[55] D. Golanski, K. Terada, and N. Kikuchi. Macro and micro scale modeling of thermal residual stresses in metal matrix composite surface layers by the homogenization method. *Comput. Mech.*, 19:188–202, 1997.

[56] S. Ghosh and Y. Liu. Voronoi cell finite element model based on micropolar theory of thermoelasticity for heterogeneous materials. *Int. J. Numer. Methods Engrg.*, 38:1361–1398, 1995.

[57] S. Moorthy, S. Ghosh, and Y.S. Liu. Voronoi cell finite element model for thermoelastoplastic deformation in random heterogeneous media. *Appl. Mech. Rev.*, 47:207–221, 2001.

[58] Q. Yu and J. Fish. Multiscale asymptotic homogenization for multiphysics problems with multiple spatial and temporal scales: a coupled thermo-viscoelastic example problem. *Int. J. Solids Struct.*, 39:6429–6452, 2002.

[59] H. W. Zhang, S. Zhang, J. Y. Bi, and B. A. Schrefler. Thermo-mechanical analysis of periodic multiphase materials by a multiscale asymptotic homogenization approach. *Int. J. Numer. Meth. Engng*, 69:87–113, 2007.

[60] L. Ozdemir, W.A.M. Brekelmans, and M.G.D. Geers. FE^2 computational homogenization for the thermo-mechanical analysis of heterogeneous solids. *Comput. Methods Appl. Mech. Engrg.*, 198:602–613, 2008.

[61] A. H. Muliana. Multi-scale framework for the thermo-viscoelastic analyses of polymer composites. *Mech. Res. Commun.*, 35:89–95, 2008.

[62] A. H. Muliana and R. Haj-Ali. A multi-scale framework for layered composites with thermo-rheologically complex behaviors. *Int. J. Solids Struct.*, 45:2937–2963, 2008.

[63] C. Baiocchi, F. Brezzi, and L. P. Franca. Virtual bubbles and the galerkin-least-squares method. *Comput. Methods Appl. Mech. Engrg.*, 105:125–142, 1993.

[64] F. Brezzi, L. P. Franca, T. J. R. Hughes, and A. Russo. $b = \int g$. *Comput. Methods Appl. Mech. Engrg.*, 145:329–339, 1997.

[65] J. Mergheim. A variational multiscale method to model crack propagation at finite strains. *Int. J. Numer. Meth.Engng.*, 80:269–289, 2009.

[66] E. W. C. Coenen, V. G. Kouznetsova, and M. G. D Geers. Novel boundary conditions for strain localization analyses in microstructural volume elements. *Int. J. Numer. Meth. Engng.*, 90:1–21, 2012.

[67] S. Ghosh and D. Paquet. Adaptive concurrent multi-level model for multi-scale analysis of ductile fracture in heterogeneous aluminum alloys. *Mech. Mater.*, 65:12–34, 2013.

[68] H. P. Langtangen. *Computational partial differential equations: Numerical methods and diffpack programming*. Springer, 2003.

[69] R. Crouch and C. Oskay. Symmetric meso-mechanical model for failure analysis of heterogeneous materials. *Int. J. Solids Struct.*, 8:447–461, 2010.

[70] R. Courant and D. Hilbert. *Methods of Mathematical Physics, Volume 1*. Wily-VCH, 1991.

[71] *Department of Defense Handbook - Metallic material and elements for aerospace vehicle structures, MIL-HDBK-5J, 31 January 2003*.

[72] J. Fish, K. Shek, M. Pandheeradi, and M. Shephard. Computational plasticity for composite structures based on mathematical homogenization: Theory and practice. *Comput. Methods Appl. Mech. Engrg.*, 148:53–73, 1997.

[73] V.G. Kouznetsova, M.G.D. Geers, and W.A.M. Brekelmans. Multi-scale second-order computational homogenization of multi-phase materials: a nested finite element solution strategy. *Comput. Methods Appl. Mech. Engrg.*, 193:5525–5550, 2004.

[74] R. Hu and C. Oskay. Nonlocal homogenization model for wave dispersion and attenuation in elastic and viscoelastic periodic layered media. *J. Appl. Mech.*, in press, 2017.

[75] S. Ghosh, K. Lee, and S. Moorthy. Two scale analysis of heterogeneous elastic-plastic materials with asymptotic homogenization and voronoi cell finite element model. *Comput. Methods Appl. Mech. Engrg.*, 132:63–116, 1996.

[76] S. Mall and T. Nichols. *Titanium matrix composites: mechanical behavior*. Taylor & Francis, 1997.

[77] G. R. Johnson and W. H. Cook. Fracture characteristics of three metal subjected to various strain, strain rates, temperatures and pressure. *Eng. Fract. Mech.*, 21:31–48, 1985.

[78] H. E. Pettermann, A. F. Plankensteiner, H. J. Bohm, and F. G. Rammerstorfer. A thermo-elasto-plastic constitutive law for inhomogeneous materials based on an incremental mori-tanaka approach. *Comput. Struct.*, 71:197–214, 1999.

[79] J. R. Rice. A metalgorithm for adaptive quadrature. *J. Assoc. Comp. Mach.*, 22:61–82, 1975.

[80] J. R. Rice. Adaptive approximation. *J. Approx. Theory*, 16:329–337, 1976.

[81] N. Carrere, D. Boivin, R. Valle, and A. Vassel. Local texture measurements in a SiC/Ti composite manufactured by the foil-fiber-foil. *Scripta Mater.*, 44:867–872, 2001.

[82] N. Carrere, J.-F. Maire, S. Kruch, and J.-L. Chaboche. Multiscale analysis of SiC/Ti composites. *Mater. Sci. Eng., A*, 365:275–281, 2004.

[83] D. Bettge, B. Gunther, W. Wedell, P.D. Portella, J. Hemptenmacher, P.W.M. Peters, and B. Skrotzki. Mechanical behavior and fatigue damage of a titanium matrix composite reinforced with continuous SiC fibers. *Mater. Sci. Eng., A*, 452-453:536–544, 2007.

[84] L. Figiel and B. Gunther. Modelling the high-temperature longitudinal fatigue behaviour of metal matrix composites (SiC/Ti-6242): Nonlinear time-dependent matrix behaviour. *Int. J. Fatigue*, 30:268–276, 2008.

[85] H. Yan and C. Oskay. A three-field (displacement-pressure-concentration) formulation for coupled transport-deformation problems. *Finite Elements Anal. Des.*, 90:20–30, 2014.

[86] S. Zhang and C. Oskay. Reduced order variational multiscale enrichment method for thermo-mechanical problems. *Comput. Mech.*, 59:887–907, 2017.

[87] F. Feyel and J. L. Chaboche. Fe^2 multiscale approach for modeling the elastoviscoplastic behaviour of long fibre sic/ti composite materials. *Comput. Methods Appl. Mech. Engrg.*, 183:309–330, 2000.

[88] A. S. Khan, A. Yu, and H. Liu. Deformation induced anisotropic responses of Ti-6Al-4V alloy Part II: A strain rate and temperature dependent anisotropic yield criterion. *Int. J. Plasticity*, 38:14–26, 2012.

[89] A. L. Pilchak, W. J. Porter, and R. John. Room temperature fracture processes of a near-α titanium alloy following elevated temperature exposure. *J. Mater. Sci.*, 47:7235–7253, 2012.

[90] G. N. Praveen and J. N. Reddy. Nonlinear transient thermoelastic analysis of functionally graded ceramic-metal plates. *Int. J. Solids Struct.*, 35:4457–4476, 1997.

[91] J. N. Reddy. Analysis of functionally graded plates. *Int. J. Numer. Meth. Engng*, 47:663–684, 2000.

[92] A. Bensoussan, J-L. Lions, and G. Papanicolau. *Asymptotic Analysis for Periodic Structures*. Elsevier, 1978.

[93] D. Cioranescu and P. Donato. *An Introduction to Homogenization*. Oxford University Press, 1999.

[94] T. Belytschko, J. S.-J. Ong, W. K. Liu, and J. M. Kennedy. Hourglass control in linear and nonlinear problems. *Comput. Methods Appl. Mech. Engrg.*, 43:251–276, 1984.

[95] O. P. Jacquotte and J. T. Oden. Analysis of hourglass instabilities and control in underintegrated finite element methods. *Comput. Methods Appl. Mech. Engrg.*, 44:339–363, 1984.

[96] T. J. R. Hughes. *The Finite Element Method: Linear Static and Dynamic Finite Element Analysis*. Prentice-Hall, Inc. Englewood Cliffs, N. J., 2000.

[97] R. D. Cook, D. S. Malkus, M. E. Plesha, and R. J. Witt. *Concepts and Applications of Finite Element Analysis, 4th Edition*. John Wiley & Sons. Inc., 2002.